NASA Contractor Report 178101

ICASE REPORT NO. 86-22

IN-747/

ICASE

UNIFORMLY HIGH ORDER ACCURATE ESSENTIALLY NON-OSCILLATORY SCHEMES III.

Ami Harten

Bjorn Engquist

Stanley Osher

Sukumar R. Chakravarthy

Contract Nos. NAS1-17070, NAS1-18107

April 1986

INSTITUTE FOR COMPUTER APPLICATIONS IN SCIENCE AND ENGINEERING
NASA Langley Research Center, Hampton, Virginia 23665

Operated by the Universities Space Research Association

National Aeronautics and
Space Administration

Langley Research Center
Hampton, Virginia 23665

UNIFORMLY HIGH ORDER ACCURATE ESSENTIALLY NON-OSCILLATORY SCHEMES III.

Ami Harten[1]
Department of Mathematics, UCLA and School of
Mathematical Sciences, Tel-Aviv University.

Bjorn Engquist[1], Stanley Osher[1]
Department of Mathematics, UCLA

Sukumar R. Chakravarthy
Rockwell Science Center, Thousand Oaks, Ca.

Dedicated to Peter Lax on his 60th birthday

ABSTRACT

In this paper, a third in a series we continue the construction and the analysis of essentially non-oscillatory shock capturing methods for the approximation of hyperbolic conservation laws. We present an hierarchy of uniformly high order accurate schemes which generalizes Godunov's scheme and its second order accurate MUSCL extension to arbitrary order of accuracy. The design involves an essentially non-oscillatory piecewise polynomial reconstruction of the solution from its cell averages, time evolution through an approximate solution of the resulting initial value problem, and averaging of this approximate solution over each cell. The reconstruction algorithm is derived from a new interpolation technique that when applied to piecewise smooth data gives high-order accuracy whenever the function is smooth but avoids a Gibbs phenomenon at discontinuities. Unlike standard finite difference methods this procedure uses an adaptive stencil of grid points and consequently the resulting schemes are highly nonlinear.

---

[1]Research was supported by NSF Grant No. DMS85-03294, ARO Grant No. DAAG29-85-K-0190, NASA Consortium Agreement No. NCA2-IR390-403, and NASA Langley Grant No. NAG1-270. Also, research for the first and third authors was partially supported under NASA Contracts NAS1-17070 and NAS1-18107 while in residence at the Institute for Computer Applications in Science and Engineering (ICASE), NASA Langley Research Center, Hampton, VA 23665-5225.

1. Introduction. In this paper, the third in a series we continue to study the use of essentially nonoscillatory, uniformly high-order accurate schemes for the numerical approximation of weak solutions of hyperbolic systems of conservation laws

$$u_t + f(u)_x = 0 \tag{1.1a}$$

$$u(x,0) = u_0(x). \tag{1.1b}$$

Here $u = (u_1, ..., u_m)^T$ is a state vector and $f(u)$, the flux, is a vector valued function of m components. The system is hyperbolic in the sense that the $m \times m$ Jacobian matrix

$$A(u) = \partial f / \partial u$$

has m real eigenvalues

$$a_1(u) \leq a_2(u) \leq \cdots \leq a_m(u)$$

and a complete set of m linearly independent right-eigenvectors $\{r_k(u)\}_{k=1}^m$. We denote by $\{l_k(u)\}_{k=1}^m$ the left-eigenvectors of $A(u)$ and assume that $l_i r_k = \delta_{ik}$.

We assume that the initial value problem (IVP) (1.1) (embedded in an appropriate setting which includes entropy considerations) is well-posed in the sense of Cauchy and that its weak solutions are generically piecewise smooth. We denote its evolution operator by $E(t)$, i.e.

$$u(\cdot, t) = E(t) \cdot u_0. \tag{1.2}$$

Let $\bar{w}(x)$ denote the sliding average of $w(x)$

$$\bar{w}(x) \equiv \frac{1}{h} \int_{-h/2}^{h/2} w(x+y)dy \equiv (A_h \cdot w)(x) \tag{1.3a}$$

We note that $\bar{w}$ is smoother than w by one derivative, and that at points of smoothness

$$\bar{w}(x) = w(x) + O(h^2). \tag{1.3b}$$

The sliding average in x of a weak solution of (1.1), $\bar{u}(x,t)$, satisfies

$$\frac{\partial}{\partial t}\bar{u}(x,t) + \frac{1}{h}[f(u(x+h/2,t)) - f(u(x-h/2,t))] = 0. \tag{1.4}$$

Integrating this relation from t to $t+\tau$, we get

$$\bar{u}(x,t+\tau) = \bar{u}(x,t) - \lambda[\hat{f}(x+h/2,t;u) - \hat{f}(x-h/2,t;u)] \tag{1.5a}$$

where $\lambda = \tau/h$ and

$$\hat{f}(x,t;w) = \frac{1}{\tau}\int_0^\tau f(w(x,t+\eta))d\eta. \tag{1.5b}$$

Let $\{I_j \times [t_n, t_{n+1}]\}_j$ where $I_j = [x_{j-\frac{1}{2}}, x_{j+\frac{1}{2}}]$, $x_\alpha = \alpha h$, $t_n = n\tau$, be a partition of $\mathbf{R}\times\mathbf{R}^+$. Writing relation (1.5) at $x = x_j, t = t_n$ we get

$$\bar{u}_j^{n+1} = \bar{u}_j^n - \lambda[\hat{f}(x_{j+\frac{1}{2}}, t_n; u) - \hat{f}(x_{j-\frac{1}{2}}, t_n; u)]. \tag{1.6a}$$

Here

$$\bar{u}_j^n = \bar{u}(x_j, t_n) = \frac{1}{h}\int_{I_j} u(x,t_n)dx \tag{1.6b}$$

is the "cell-average" of u at time t_n.

In this paper we describe a class of numerical schemes that generalizes Godunov's scheme [5] and its second order extensions ([22], [4], [15]) to any finite order of accuracy. These schemes can be written in standard conservation form

$$v_j^{n+1} = v_j^n - \lambda(\bar{f}_{j+\frac{1}{2}} - \bar{f}_{j-\frac{1}{2}}) \equiv (\bar{E}_h(\tau)\cdot v^n)_j. \tag{1.7a}$$

Here $\bar{E}_h(\tau)$ denotes the numerical solution operator and $\bar{f}_{j+\frac{1}{2}}$, the numerical flux, denotes a function of $2k$ variables

$$\bar{f}_{j+\frac{1}{2}} = \bar{f}(v^n_{j-k+1}, ..., v^n_{j+k}), \tag{1.7b}$$

which is consistent with the flux $f(u)$ in (1.1) in the sense that $\bar{f}(u, u, ..., u) = f(u)$. We design these schemes so that the conservation form (1.7a) will approximate (1.5) to high order of accuracy. Setting $v^n_j \equiv \bar{u}^n_j$ in (1.7) and comparing it to (1.6) we see that if the numerical flux (1.7b) can be expanded as

$$\bar{f}_{j+\frac{1}{2}} = \hat{f}(x_{j+\frac{1}{2}}, t_n; u) + d(x_{j+\frac{1}{2}})h^r + \mathcal{O}(h^{r+1}) \tag{1.8a}$$

then

$$v^{n+1}_j = \bar{u}^{n+1}_j - \lambda\left[d(x_{j+\frac{1}{2}}) - d(x_{j-\frac{1}{2}})\right]h^r + O(h^{r+1}).$$

This shows that if the numerical flux $\bar{f}_{j+\frac{1}{2}}$ satisfies (1.8a) then the truncation error in the sense of cell averages is

$$\bar{u}(x_j, t_n - \tau) - \left[\bar{E}_h(\tau)\bar{u}(\cdot, t_n)\right]_j = \lambda\left[d(x_{j+\frac{1}{2}}) - d(x_{j-\frac{1}{2}})\right]h^r + O(h^{r+1}), \tag{1.8b}$$

which is $O(h^{r+1})$ where $d(x)$ is Lipschitz continuous.

When $f(u)$ is a nonlinear function of u, the approximation of $\hat{f}(x_{j+\frac{1}{2}}, t_n; u)$ to $O(h^r)$ requires knowledge of pointwise values of the solution to the same order of accuracy. In order to design a numerical flux that satisfies (1.8a), we must extract high order accurate pointwise information from the given $\{v^n_j\}$, which are approximations to $\{\bar{u}^n_j\}$, the cell averages (1.6b) of the solution. Solving this reconstruction problem to arbitrarily high-order of accuracy r, without introducing $O(1)$ Gibbs-like spurious oscillations at points of discontinuity, is the most important step in the design of our new schemes.

Given $\bar{w}_j = \bar{w}(x_j)$, cell averages of a piecewise smooth function $w(x)$, we construct $R(x;\bar{w})$, a piecewise polynomial function of x of uniform polynomial degree $(r-1)$ that satisfies:

(i) At all points x for which there is a neighborhood where w is smooth

$$R(x;\bar{w}) = w(x) + e(x)h^r + O(h^{r+1}). \tag{1.9a}$$

(ii) conservation in the sense of

$$\bar{R}(x_j;\bar{w}) = \bar{w}_j \tag{1.9b}$$

here $\bar{R}$ denotes the sliding average (1.3) of R.

(iii) It is essentially non-oscillatory

$$TV(R(\cdot;\bar{w})) \le TV(w) + O(h^r), \tag{1.9c}$$

where TV denotes total-variation in x.

The inequality (1.9c) implies that the reconstruction R is essentially non-oscillatory in the sense that it does not have a Gibbs-like phenomenon of generating $O(1)$ spurious oscillations at points of discontinuity that are proportional to the size of the jump there. In [16], [11], [17] we describe $R(x;\bar{w})$ in the scalar case. We show there that R may occasionally produce $O(h^r)$ spurious oscillations which are on the level of the truncation error. These small spurious oscillations may occur only in the smooth part of w and they usually disappear once $w(x)$ is adequately resolved on the computational mesh. For sake of completeness we review this reconstruction algorithm in section 3; we shall extend it to vector functions $w(x)$ in Section 5 of this paper.

Using the reconstruction (1.9) we can express the abstract form of our new schemes by

$$\tilde{E}_h(\tau)\cdot\bar{w} \equiv A_h \cdot E(\tau)\cdot R(\cdot;\bar{w}). \tag{1.10}$$

Here A_h is the cell-averaging operator on the RHS of (1.3); $E(t)$ is the exact evolution operator (1.2) and w is any piecewise smooth function of x. These schemes are a generalization of Godunov's scheme and its second-order extensions in the sense that (1.10) with the first order accurate piecewise constant reconstruction

$$R(x;\bar{w}) = \bar{w}_j \qquad \text{for } x_{j-\frac{1}{2}} \le x < x_{j+\frac{1}{2}} \tag{1.11}$$

is exactly Godunov's schemes ([5]); (1.10) with the second order accurate piecewise linear reconstruction

$$R(x;\bar{w}) = \bar{w}_j + s_j(x - x_j) \qquad \text{for } x_{j-\frac{1}{2}} \le x < x_{j+\frac{1}{2}} \tag{1.12a}$$

such that

$$s_j = w_x(x_j) + O(h), \tag{1.12b}$$

is the abstract form of the second-order extensions to Godunov's scheme described in [22],[4] and [15].

We recall that the evolution operator $E(t)$ is monotone in the scalar case. Since A_h, the cell-averaging operator is also monotone we see that in the scalar case

$$TV(\bar{E}_h(\tau)\bar{w}) = TV(A_h \cdot E(\tau) \cdot R(\cdot;\bar{w})) \le TV(R(\cdot;\bar{w})). \tag{1.13a}$$

If $\bar{w}$ in (1.13a) is the sliding average of a piecewise smooth function $w(x)$, it follows then from (1.9c) that

$$TV(\bar{E}_h(\tau)\bar{w}) \le TV(w) + O(h^r). \tag{1.13b}$$

This shows that the schemes (1.10) in the scalar case are essentially non-oscillatory in exactly the same way as the reconstruction: They do not have a Gibbs-like phenomenon at discontinuities, yet they may occasionally produce small

spurious oscillations on the level $O(h^r)$ of the trunction error (see Remark 1.3 at the end of this section).

(1.10) is the abstract operator expression of a scheme in the conservation form (1.7). Although the scheme generates discrete values v_j^n, which are r-th order accurate approximations to the cell-averages $\bar{u}_j^n$, its operation involves a globally defined pointwise approximation to $u(x,t)$ of the same order of accuracy, which we denote by $v_h(x,t)$. The latter is defined for all x in the time-strips $t_n \le t < t_{n+1}$, with a possible discontinuity at $\{t_k\}$; we shall use the standard notation $v_h(x, t_n \pm 0)$ to distinguish between the two possibly different values.

We define $v_h(x,t)$ via the following algorithmic description of the scheme (1.10). We start by setting

$$v_j^\circ = \bar{u}_0(x_j)$$

where u_0 is the given initial datum (1.1b), and $\bar{u}_0$ is its sliding average (1.3a). Having defined $v^n = \{v_j^n\}$, approximation to $\{\bar{u}_j^n\}$ in (1.6b), we proceed to evaluate v^{n+1} by the following three steps:

(i) Reconstruction: Define

$$v_h(x, t_n + 0) = R(x; v^n), \tag{1.14a}$$

Note that $v_h(x, t_n + 0)$ is a pointwise approximation to $u(x, t_n)$.

(ii) Solution in the small: For $t_n \le t < t_n + \tau = t_{n+1}$, define

$$v_h(\,;t) = E(t - t_n) \cdot v_h(\cdot\,; t_n + 0). \tag{1.14b}$$

(iii) Cell-averaging: Close the time-loop of the algorithm by defining

$$v_j^{n+1} = \bar{v}_h(x_j; t_{n+1} - 0) = \frac{1}{h} \int_{x_{j-\frac{1}{2}}}^{x_{j+\frac{1}{2}}} v_h(x, t_{n+1} - 0)\,dx. \tag{1.14c}$$

We note that v_h, being an exact solution of (1.1) in $t_n \le t < t_{n+1}$, satisfies (1.5) in this strip. Using the conservation property (1.9b) of the reconstruction in (1.14a), i.e.

$$\bar{v}_h(x_j, t_n + 0) = v_j^n, \tag{1.15}$$

we get from (1.5) that the scheme (1.10), (1.14) satisfies the conservation form

$$v_j^{n+1} = v_j^n - \lambda(\bar{f}_{j+\frac{1}{2}} - \bar{f}_{j-\frac{1}{2}}) \tag{1.16a}$$

with the numerical flux

$$\bar{f}_{j+\frac{1}{2}} = \hat{f}(x_{j+\frac{1}{2}}, t_n; v_h) \equiv \frac{1}{\tau}\int_0^\tau f(v_h(x_{j+\frac{1}{2}}, t_n + \eta))d\eta. \tag{1.16b}$$

We turn now to examine the local truncation error of the scheme. For this purpose we consider a single application of (1.14) starting with $v_j^n \equiv \bar{u}_j^n$, the exact cell-averages of the solution. It follows from (1.9a) and (1.14a) that

$$v_h(x, t_n + 0) = u(x, t_n) + e(x)h^r + O(h^{r+1}). \tag{1.17a}$$

The definition (1.14b) and our assumption of the well-posedness of the IVP (1.1) imply that

$$v_h(x, t) = u(x, t) + O(h^r) \text{ for } t_n \le t < t_{n+1}. \tag{1.17b}$$

This in turn implies that the numerical flux (1.16b) of the scheme satisfies (1.8a), i.e.

$$\bar{f}_{j+\frac{1}{2}} = \hat{f}(x_{j+\frac{1}{2}}, t_n; u) + d(x_{j+\frac{1}{2}})h^r + O(h^{r+1}). \tag{1.17c}$$

Clearly non-smoothness of $d(x)$ in (1.17c) can result only from non-smoothness of the coefficient $e(x)$ in (1.17a). It follows then from (1.8b) that away from points

of discontinuity and points at which $e(x)$ fails to be Lipschitz continuous, the local truncation error in the sense of cell-averages is $O(h^{r+1})$.

Let $u(x,t)$ be a smooth solution of (1.1) and let us suppose that as $h \to 0$, $\tau = O(h)$, the numerical approximation converges pointwise to $u(x,t)$. If $e(x)$ is globally Lipschitz cntinuous then the local truncation error in the sense of cell averages is globally $\mathcal{O}(h^{r+1})$. At time t, after performing $N = t/\tau$ time-steps, we expect the cumulative error to be $O(h^r)$, i.e.

$$v_j^N = \bar{u}(x_j, t_N) + O(h^r) \tag{1.18a}$$

In this case we see from (1.9a) that

$$v_h(x, t_N + 0) = R(x; v^N) = u(x, t_N) + O(h^r). \tag{1.18b}$$

Thus at the end of the computation we have two sets of output data at our disposal: (i) Discrete values $\{v_j^N\}$ that approximate $\{\bar{u}(x_j, t_N)\}$ to $O(h^r)$. (ii) A piecewise polynomial function of x, $R(x; v^N)$, that approximates $u(x, t_N)$ to $O(h^r)$.

REMARK: (1.1). Note that (1.8) is quite different from the truncation error in a pointwise sense which is used in formulating Lax-Wendroff-type schemes [20], [21]. There we take $v_j^n = u(x_j, t_n)$ and require $v_j^{n+1} = u(x_j, t_{n+1}) + O(h^{r+1})$. To accomplish that we need a numerical flux that satisfies

$$-\lambda(\bar{f}_{j+\frac{1}{2}} - \bar{f}_{j-\frac{1}{2}}) = \sum_{k=1}^{r} \frac{\tau^k}{k!} \frac{\partial^k u}{\partial t^k}\Big|_{(x_j, t_n)} + O(h^{r+1}).$$

We shall see in the following that condition (1.8a) for the accuracy in a cell-average sense is more manageable in many respects

REMARK (1.2): When $e(x)$ fails to be Lipschitz continuous at a point, the local truncation error (1.8b) is only $\mathcal{O}(h^r)$. In the MUSCL-type schemes [22],[4] this

happens at local extremum points· in higher-order accurate schemes this may occur at roots of higher derivatives of u (see [15], [11]). Due to local accumulation we expect the pointwise error at time t, after $N = t/\tau$ time-steps, to be only $O(h^{r-1})$ at such points. Away from these points we expect the pointwise cumulative error to remain $O(h^r)$. Consequently the scheme is $(r-1)$-th order accurate in the maximum norm. Because of the non-oscillatory nature of the schemes, we expect the number of points where $e(x)$ fails to be Lipschitz-continuous to remain bounded as $h \to 0$. In this case the L_1-norm of the cumulative error is $O(h^r)$. To distinguish between schemes that are r-th order accurate in the usual pointwise sense, and those that are r-th order accurate in the L_1-norm but only $(r-1)$-th accurate in the maximum norm, we shall use "r-th order accurate" for the latter, thus qualifying the difference by the use of quotation marks.

REMARK (1.3): It is well known that if the total variation of the numerical approximation is uniformly bounded, i.e.

$$TV(v_h(\cdot,t)) \leq C \cdot TV(u_0) \tag{1.19}$$

where the constant C is independent of h for $0 \leq t \leq T$, then any refinement sequence $h \to 0$, $\tau = O(h)$ has a subsequence that converges in L_1^{loc} to a weak solution of (1.1). Therefore uniform boundedness of the total variation is an appropriate sense of stability for numerical approximations to discontinuous solutions of (1.1); see [9], [10] and the references cited there.

Inequality (1.13) shows that the total variation of our new schemes is dominated by that of reconstruction step

$$TV(v^{n+1}) \leq TV(R(\cdot;v^n)). \tag{1.20}$$

When R is the piecewise-constant function (1.11) or the piecewise-linear function (1.12) (where the slope s_j is that of the MUSCL scheme) then

$$TV(R(\cdot;v)) \le TV(v) \tag{1.21a}$$

for any function v of bounded total variation. Consequently Godunov's scheme and the MUSCL scheme are total variation diminishing (TVD) in the scalar case

$$TV(v^{n+1}) \le TV(v^n); \tag{1.21b}$$

this trivially implies (1.19) with $C = 1$.

In proving relation (1.9c) for higher order reconstructions we have used the assumption that for h sufficiently small there are at least $r+1$ points of smoothness between discontinuities. Consequently we cannot apply this result to the numerical solution v^n. Nevertheless, based on heuristic analysis and extensive numerical experimentation, we conjecture that in the scalar case

$$TV(v^{n+1}) \le TV(v^n) + O(h^{p+1}) \tag{1.22}$$

for some $p > 0$.

2. Review and overview. In [15], the first paper of this series, we present a second-order accurate scheme which is strictly non-oscillatory in the scalar case ($m = 1$) i.e.,

$$N_0(v^{n+1}) \leq N_0(v^n) \tag{2.1}$$

where $N_0(v)$ denotes the number of local extreme in v. This scheme is a modification of the "second-order accurate" MUSCL scheme [22], [4], which is total-variation-diminishing (TVD) in the scalar case, i.e.

$$TV(v^{n+1}) \leq TV(v^n). \tag{2.2}$$

In order to enforce (2.2), the slope s_j (1.12a) in the MUSCL scheme is subjected to a so called "limiter". Due to the operation of this limiter, the coefficient in the $O(h)$ term in the Taylor expansion (1.12b) becomes discontinuous at local extrema: Consequently $e(x)$ in (1.9a) fails to be Lipschitz continuous at such points, which leads to a loss of accuracy at local extrema. In [15] this difficulty is circumvented by using a modified slope s_j in (1.12a) which satisfies

$$s_j = w_x(x_j) + O(h^2), \tag{2.3}$$

thus leading to a globally smooth $e(x)$ in (1.9a).

Although the end result is a simple technical modification of the formula for the slope s_j, the design of the scheme in [15] invokes major conceptual changes. Realizing that TVD schemes, independent of their particular form, are necessarily only first-order accurate at local extrema, we seek a weaker notion of control over possible growth of total variation of the numerical solution. For this purpose we introduce the notion (2.1) of non-oscillatory schemes, which satisfy in the scalar case for piecewise smooth w

$$TV(\bar{E}_h(\tau) \cdot \bar{w}) \leq TV(w) + O(h^2) \tag{2.4}$$

rather than (2.2). In [16], the second paper in this series, we show that even the notion of (strictly) non-oscillatory schemes (2.1) is too restrictive in the sense that it limits the order of accuracy to 2. To enable the design of higher-order accurate schemes we then introduce the notion of *essentially* non-oscillatory schemes (1.13), which excludes a Gibbs-like phenomenon but allows for the production of spurious oscillations on the level of the truncation error.

Another conceptual change is the removal of the "monotonicity limiters" which are an essential part of TVD schemes ([30]) and may cause reduction of order of accuracy at some points. Our new schemes are of uniform order of accuracy r. The control over possible growth of the total variation of the numerical solution is obtained by an adaptive stencil that at each point attempts to use the smoothest information available. This adaptive selection of stencil is introduced to the algorithm through the reconstruction step (1.14a). The number of points in the stencil, independent of its orientation, is always $(r+1)$.

In [16], the second paper in the series, we investigate the stability of our new schemes in the scalar constant coefficient case

$$u_t + a u_x = 0, \qquad a = \text{constant}. \tag{2.5a}$$

The exact evolution operator (1.2) in this case is just a translation with the constant speed a. Therefore our schemes (1.14) take the particularly simple form

$$v_j^{n+1} = \bar{R}(x_j - a\tau; v^n). \tag{2.5b}$$

Due to the adaptive selection of stencil in the reconstruction step, the scheme (1.23b) is highly nonlinear; consequently the use of the standard linear stability analysis is inappropriate. We demonstrate this point in [16] by choosing initial data for which the reconstruction algorithm selects a stencil that is biased in the "down-wind" direction (i.e. in the direction opposite to that of the wind); a constant choice of

such a stencil is notoriously unstable. Such an instability usually exhibits itself by the production of increasing oscillations which starts at the highest derivative and propagates to the function itself. The numerical experiment in [16] shows that once these oscillations begin to appear on the level of the highest derivative, the adaptive selection of stencil in (2.5b) reacts by changing the orientation of the stencil and thus avoids the build up of instability.

In [16] we also investigate the initial-boundary value problem (IBVP) for (2.5a). Unlike the treatment of boundaries in standard finite-difference schemes we do not use "numerical boundary conditions". Instead we modify the scheme (2.5b) by restricting the selection of the stencil to available information. As a result the scheme is biased "against the wind" at one of the two boundaries. Nevertheless, numerical experiments show the scheme to be strongly stable.

In the present paper, the third in the series, we turn to consider the general nonlinear case. The abstract form of our schemes, (1.10) and (1.14), calls for the evaluation of the exact *solution in the small* (i.e. for $0 \le t < \tau$, τ small) of the IVP (1.1) with the initial data $R(x; v^n)$; the latter is a piecewise polynomial function of x with possible discontinuities at $\{x_{j+\frac{1}{2}}\}$.

When $R(x; v^n)$ is the piecewise-constant function (1.11) (i.e. Godunov's scheme), we can express this solution in terms of local solutions to the Riemann problem

$$u_t + f(u)_x = 0, \qquad u(x,0) = \begin{cases} v_j^n & x < 0 \\ v_{j+1}^n & x > 0 \end{cases}. \tag{2.7}$$

When $R(x; v^n)$ is a piecewise polynomial function of higher degree we cannot in general express the solution of the IVP(1.1) in a simple closed form. Nevertheless, (see [1], [6]) we can obtain a local Taylor expansion of the solution to any desired order of accuracy.

We note, however, that the step of "solution-in-the-small" (1.14b) is followed by the step of "cell-averaging" (1.14c). consequently many of the fine details of the

exact solution, which may be very costly to compute, are later ignored in evaluating v_j^{n+1} by averaging the exact solution over $(x_{j-\frac{1}{2}},\ x_{j+\frac{1}{2}})$. To economize on the cost of our schemes it makes sense to use simplified approximate "solvers" that carry only this information which determines the value of the cell-average, namely the one needed to compute a numerical flux satisfying (1.17c). The study of such approximate solvers is the main issue of the present paper. In Section 4 we consider the scalar case; in Section 5 we extend the scheme to hyperbolic systems of conservation laws.

When we consider the reconstruction (1.9) in the context of approximation of functions, the assumption that $w(x)$ is piecewise smooth with a finite number of discontinuities implies that for h sufficiently small these are at least $(r+1)$ points of smoothness separating discontinuities on the computational grid. Therefore at any point of smoothness it is possible to select a stencil from the smooth part of the function. Although the x-behaviour of weak solutions of (1.1) is generically of this type, their time dependence allows for collision of discontinuities, as well as their collision with a boundary, e.g. solid walls. For points in a region between two discontinuities that are about to collide, no matter how small is h, there must come a time when there are not enough points to select a stencil of $(r+1)$ points from the region of smoothness. Consequently a component-wise extension of the scalar reconstruction algorithm in [16] to vector functions may produce large spurious oscillations during this brief encounter.

The elimination of such spurious oscillations has been a major consideration in designing the extension of our scalar schemes to systems of conservation laws. In Section 5 we show that this can be accomplished to a great extent by extending the scalar reconstruction algorithms to systems via the use of locally defined characteristic variables.

In Section 6 we describe in detail the algorithm for the solution of the Euler equations of gas dynamics. In Section 7 we present some numerical experiments.

In future papers we shall present the extension of these schemes to two-dimensional problems and study the dependence of the computational efficiency on the order of accuracy of the scheme.

3. Reconstruction. In this section we present a brief description of the reconstruction $R(x;w)$ to be used in (1.14a); we refer the reader to [16], [11], [17] for more details and analysis. For this purpose we introduce $H_m(x;w)$, a piecewise polynomial function of x that interpolates w at the points $\{x_j\}$, i.e.

$$H_m(x_j;w) = w(x_j), \tag{3.1a}$$

$$H_m(x;w) \equiv q_{m,j+\frac{1}{2}}(x;w) \qquad \text{for } x_j \le x \le x_{j+1}, \tag{3.1b}$$

where $q_{m,j+\frac{1}{2}}$ is a polynomial in x of degree m.

We take $q_{m,j+\frac{1}{2}}$ to be the (unique) m-th degree polynomial that interpolates $w(x)$ at the $(m+1)$ successive points $\{x_i\}$, $i_m(j) \le i \le i_m(j)+m$, that include x_j and x_{j+1}, i.e.

$$q_{m,j+\frac{1}{2}}(x_i;w) = w(x_i) \qquad \text{for } i_m(j) \le i \le i_m(j)+m. \tag{3.2a}$$

$$1-m \le i_m(j) - j \le 0. \tag{3.2b}$$

Clearly there are exactly m such polynomials corresponding to the m different choices of $i_m(j)$ subject to (3.2b). This freedom is used to assign to (x_j, x_{j+1}) a stencil of $(m+1)$ points (3.2) so that $w(x)$ is "smoothest" in $(x_{i_m(j)},\ x_{i_m(j)+m})$ in some asymptotic sense.

The information about smoothness of $w(x)$ is extracted from a table of divided differences of w. The latter can be defined recursively by

$$w[x_i] = w(x_i) \tag{3.3a}$$

$$w[x_i, \ldots, x_{i+k}] = (w[x_{i+1}, \ldots, x_{i+k}] - w[x_i, \ldots, x_{i+k-1}])/(x_{i+k} - x_i). \tag{3.3b}$$

It is well known that if w is C_∞ in $[x_i, x_{i+k}]$ then

$$w[x_i, ..., x_{i+k}] = \frac{1}{k!}\frac{d^k}{dx^k}w(\xi_{i,k}),\ x_i \le \xi_{i,k} \le x_{i+k}. \tag{3.3c}$$

However if w has a jump discontinuity in the p-th derivative in this interval, $0 \le p \le k$, then

$$w[x_i, ..., x_{i+k}] = O(h^{-k+p}[w^{(p)}]); \tag{3.3d}$$

here $[w^{(p)}]$ denotes the jump in the p-th derivative. (3.3c)-(3.3d) show that $|w[x_i, ..., x_{i+k}]|$ provides an asymptotic measure of the smoothness of w in (x_i, x_{i+k}), in the sense that if w is smooth in (x_{i_1}, x_{i_1+k}) but is discontinuous in (x_{i_2}, x_{i_2+k}), then for h sufficiently small $|w[x_{i_1}, ..., x_{i_1+k}]| < |w[x_{i_2}, ..., x_{i_2+k}]|$. Hence the problem of choosing a stencil of points for which w is "smoothest" is basically the same as that of finding an interval in which w has the "smallest divided differences." (see [16], [11] for more details).

In [11] we propose the following recursive algorithm to evaluate $i_m(j)$. We start by setting

$$i_1(j) = j, \tag{3.4a}$$

i.e. $q_{1,j+\frac{1}{2}}$ is the first-degree polynomial interpolating w at x_j and x_{j+1}. Let us assume that we have already defined $i_k(j)$, i.e. $q_{k,j+\frac{1}{2}}$ is the k-th degree polynomial interpolating w at

$$x_{i_k(j)}, ..., x_{i_k(j)+k}.$$

We consider now as candidates for $q_{k+1,j+\frac{1}{2}}$ the two $(k+1)$-th degree polynomials obtained by adding to the above stencil the neighboring point to the left or the one to the right; this corresponds to setting $i_{k+1}(j) = i_k(j) - 1$ or $i_{k+1}(j) = i_k(j)$,

respectively. We choose the one that gives a $(k+1)$-th order divided difference that is smaller in absolute value, i.e.

(3.4b)

$$i_{k+1}(j) = \begin{cases} i_k(j) - 1 & \text{if } |w[x_{i_k(j)-1}, ..., x_{i_k(j)+k}]| < |w[x_{i_k(j)}, ..., x_{i_k(j)+k+1}]| \\ i_k(j) & \text{otherwise.} \end{cases}$$

In [16] we analyse this interpolation technique for a piecewise smooth function w and show that: (i) wherever $w(x)$ is smooth

$$\frac{d^k}{dx^k} H_m(x; w) = \frac{d^k}{dx^k} w(x) + O(h^{m+1-k}),\ 0 \le k \le m; \tag{3.5a}$$

(ii) $H_m(x; w)$ is an essentially non-oscillatory interpolation of w in the sense that

$$TV(H_m(\cdot; w)) \le TV(w) + O(h^{m+1}). \tag{3.5b}$$

We turn now to describe two different techniques to solve the reconstruction problem (1.9) in terms of interpolation. (See appendix for an algorithmic description).

(1) *Reconstruction via Primitive function:* Given cell averages $\bar{w}_j$ of a piecewise smooth function w

$$\bar{w}_j = \frac{1}{h_j} \int_{x_{j-\frac{1}{2}}}^{x_{j+\frac{1}{2}}} w(y)dy, \quad h_j = x_{j+\frac{1}{2}} - x_{j-\frac{1}{2}}, \tag{3.6}$$

we can immediately evaluate the point-values of the primitive function $W(x)$

$$W(x) = \int_{x_0}^{x} w(y)dy \tag{3.7a}$$

by

$$W(x_{j+\frac{1}{2}}) = \sum_{i=i_0}^{j} h_j \bar{w}_j. \tag{3.7b}$$

Since

$$w(x) \equiv \frac{d}{dx} W(x)$$

we apply interpolation to the point values (3.7b) of the primitive function $W(x)$ (3.7a) and then obtain an approximation to $u(x)$ by defining

$$R(x;\bar{w}) = \frac{d}{dx} H_r(x;W). \tag{3.8}$$

We note that this procedure does not require uniformity of the mesh.

The primitive function $W(x)$ is by one derivative smoother than $w(x)$, therefore it follows from (3.5a) that wherever $W(x)$ is smooth

$$\frac{d^k}{dx^k} H_r(x;W) = \frac{d^k}{dx^k} W(x) + O(h^{r+1-k}) :$$

thus we get from the definition (3.8) that

$$\frac{d^l}{dx^l} R(x;\bar{w}) = \frac{d^l}{dx^l} w(x) + O(h^{r-l}), \tag{3.9}$$

which implies (1.9a) for $l = 0$.

The conservation property of the reconstruction (1.9b) follows immediately from the definition (3.8):

$$\begin{aligned} \frac{1}{h_j} \int_{x_{j-\frac{1}{2}}}^{x_{j+\frac{1}{2}}} R(x;\bar{w})dx &= \frac{1}{h_j}[H_r(x_{j+\frac{1}{2}};W) - H_r(x_{j-\frac{1}{2}};W)] \\ &= \frac{1}{h_j}[W(x_{j+\frac{1}{2}}) - W(x_{j-\frac{1}{2}})] = \bar{w}_j. \end{aligned} \tag{3.10}$$

The non-oscillatory nature of the reconstruction (1.9c) follows primarily from the non-oscillatory nature of the interpolation (3.5b), see [16].

We denote the reconstruction via primitive function (3.8) by RP.

(2) *Reconstruction via deconvolution:* We assume that the mesh is uniform and consider the given cell-averages $\bar{w}_j$ to be point values of $\bar{w}(x)$, the globally defined sliding-average function (1.3) of w, i.e.

$$\bar{w}_j = \bar{w}(x_j), \tag{3.11a}$$

where

$$\bar{w}(x) = \frac{1}{h}\int_{-h/2}^{h/2} w(x+y)dy. \tag{3.11b}$$

Expanding $w(x+y)$ in (3.11b) around $y=0$, we get

$$\bar{w}(x) = \sum_{k=0}^{\infty} \frac{w^{(k)}(x)}{k!}\frac{1}{h}\int_{-h/2}^{h/2} y^k dy = \sum_{k=0}^{\infty} \alpha_k h^k w^{(k)}(x) \tag{3.12a}$$

where

$$\alpha_k = \begin{cases} 0 & k \text{ odd.} \\ 2^{-k}/(k+1)! & k \text{ even} \end{cases} \tag{3.12b}$$

Multiplying both sides of (3.12a) by $h^l d^l/dx^l$ and then truncating the expansion in the RHS at $O(h^r)$, we get

$$h^l \bar{w}^{(l)}(x) = \sum_{k=0}^{r-l-1} \alpha_k h^{k+l} w^{(k+l)}(x) + O(h^r) \tag{3.13a}$$

Writing the relations (3.13a) for $l = 0, ..., r-1$ in a matrix form, we obtain

$$\begin{bmatrix} \bar{w}(x) \\ h\bar{w}'(x) \\ h^2\bar{w}''(x) \\ \vdots \\ h^{r-1}\bar{w}^{(r-1)}(x) \end{bmatrix} = \begin{pmatrix} 1 & 0 & \alpha_2 & 0 & \alpha_4 & \cdots & \alpha_{r-1} \\ & \ddots & \ddots & \ddots & \ddots & & \\ & & \ddots & \ddots & \ddots & & \alpha_4 \\ & & & \ddots & \ddots & & 0 \\ 0 & & & & \ddots & & \alpha_2 \\ & & & & & & 0 \\ & & & & & & 1 \end{pmatrix} \begin{bmatrix} w(x) \\ hw'(x) \\ h^2 w''(x) \\ \vdots \\ h^{r-1} w^{(r-1)}(x) \end{bmatrix} + O(h^r) \tag{3.13b}$$

Let us denote the coefficient matrix in the RHS of (3.13b) by C. This matrix is upper triangular and diagonally dominant. Multiplying both sides of (3.13b) by C^{-1} from the left we get

$$(3.13c)\qquad \begin{pmatrix} w(x) \\ hw'(x) \\ \cdot \\ \cdot \\ \cdot \\ h^{r-1}w^{(r-1)}(x) \end{pmatrix} = C^{-1} \begin{pmatrix} \bar{w}(x) \\ h\bar{w}'(x) \\ \cdot \\ \cdot \\ \cdot \\ h^{r-1}\bar{w}^{(r-1)}(x) \end{pmatrix} + O(h^r) \quad .$$

Given $\bar{w}_j$ we interpolate $\bar{w}(x)$ by $H_m(x;\bar{w})$ with $m \geq r-1$. Since $\bar{w}(x)$ is smoother than $w(x)$ it follows from (3.5a) that

$$\frac{d^k}{dx^k} H_m(x;\bar{w}) = \frac{d^k}{dx^k}\bar{w}(x) + O(h^{m+1-k})$$

wherever $w(x)$ is smooth. We note that although H_m is only continuous at x_j, the one-sided derivatives at $x_j \pm 0$ do satisfy the above relations, i.e.

$$(3.14)\qquad \frac{d^k}{dx^k} H_m(x_j \pm 0;\bar{w}) = \frac{d^k}{dx^k}\bar{w}(x_j) + O(h^{m+1-k}).$$

Next we define

$$(3.15a)\qquad \bar{D}_{0,j} = \bar{w}_j$$

$$(3.15b)\qquad \bar{D}_{l,j} = h^l \; M\left(\frac{d^l}{dx^l} H_m(x_j - 0;\bar{w}), \frac{d^l}{dx^l} H_m(x_j + 0;\bar{w})\right)$$
$$\text{for } 1 \leq l \leq r-1,$$

where $M(x,y)$ is the min mod function

$$(3.16)\qquad M(x,y) = \begin{cases} s \cdot \min(|x|,|y|) & \text{if } \operatorname{sgn}(x) = \operatorname{sgn}(y) = s \\ 0 & \text{otherwise} \end{cases}$$

Clearly

$$(3.17a)\qquad \bar{D}_{l,j} = h^l w^{(l)}(x_j) + O(h^r);$$

using $\bar{D}_j = (\bar{D}_{0,j}, ..., \bar{D}_{r-1,j})^T$ to approximate the vector, on the RHS of (3.13c) we get that

$$D_j = C^{-1}\bar{D}_j \tag{3.17b}$$

satisfies

$$D_j = (w(x_j), hw'(x_j), ..., h^{r-1}w^{(r-1)}(x_j))^T + O(h^r). \tag{3.17c}$$

Finally we define

$$R(x, \bar{w}) = \sum_{k=0}^{r-1} \frac{1}{k!} D_{k,j}[(x - x_j)/h]^k \quad \text{for } |x - x_j| < h/2. \tag{3.18}$$

We note that since C is upper triangular $D_{l,j}$ in (3.17b) can be computed by back-substitution, i.e. we set

$$D_{r-1,j} = \bar{D}_{r-1,j} \tag{3.19a}$$

and then compute for $k = r-2, ..., 0$

$$D_{k,j} = \bar{D}_{k,j} - \sum_{l=k+1}^{r-1} \alpha_l \, D_{l,j}. \tag{3.19b}$$

It follows immediately from the definition (3.18) and the relations (3.17a) that wherever $w(x)$ is smooth

$$\frac{d^l}{dx^l} R(x; \bar{w}) = \frac{d^l}{dx^l} w(x) + O(h^{r-l}); \tag{3.20}$$

this for $l = 0$ implies (1.9a). The conservation property of the reconstruction (1.9b) follows from

$$\frac{1}{h}\int_{-h/2}^{h/2} R(x+y; \bar{w})dy = \sum_{k=0}^{r-1} \frac{Dk,j}{k!} \frac{1}{h^{k+1}} \int_{-h/2}^{h/2} y^k dy = D_{0,j} + \sum_{k=1}^{r-1} \alpha_k \, D_{k,j} \tag{3.21}$$
$$= \bar{D}_{0,j} = \bar{w}_j.$$

The last two equalities in (3.21) follow from (3.19b) with $k = 0$ and (3.15a).

The non-oscillatory nature of the reconstruction (1.9c) follows primarily from the non-oscillatory nature of the interpolation $H_m(x; \bar{w})$; see [16] for more details.

We note that $\bar{w}(x)$ is the convolution of $w(x)$ with $\psi_h(x)$, the characteristic function of a cell, i.e.

$$\bar{w}(x) = (w * \psi_h)(x) \tag{3.22a}$$

$$\psi_h(x) = \begin{cases} 1/h \text{ for } |x| < h/2. \\ 0 \text{ for } |x| > h/2 \end{cases} \tag{3.22b}$$

Hence (3.13c) is actually a deconvolution to $O(h^r)$. Therefore we refer to (3.18) as reconstruction via deconvolution and denote it by RD.

REMARK (3.1): We note that for RP with $m = r$ and RD with $m = r - 1$ the coefficient $e(x)$ of h^r in the reconstruction error (1.9a) is discontinuous at points where there is a change of orientation in the stencil of the associated interpolation; this may happen at critical points of the function and its derivatives. Hence the resulting schemes (1.14) are "r-th order accurate" (see Remark (1.4)). On the other hand RD with $m = r$ yield $e(x)$ which is globally Lipschitz continuous, thus resulting in schemes that are r-th order accurate in a pointwise sense. This follows from the fact that (3.17a) is upgraded to

$$\bar{D}_{l,j} = h^l \bar{w}^{(l)}(x) + O(h^{r+1}) \tag{3.23}$$

which has the effect of pushing the non-smoothness due to change of stencil orientation in the associated interpolation to the $O(h^{r+1})$ level.

REMARK (3.2): We note that both RD with $r = 2$, $m = 1$ and RP with $r = 2$ are piecewise linear reconstructions of the form (1.12). The slope s_j for RD is identical to that of the "2nd-order accurate" TVD scheme in [5]. The slope for RP is the same as that of RD except at local extrema; where $s_j = 0$ for RD while for RP

$$s_j = \begin{cases} w[x_j, x_{j+1}] & \text{if } |w[x_j, x_{j+1}]| < |w[x_{j-1}, x_j]| \\ w[x_{j-1}, x_j] & \text{otherwise.} \end{cases} \tag{3.24}$$

Although RP does not "chop" local extrema as RD, the lack of smoothness in (3.24) results in the same loss of accuracy at local extrema.

We note that RD with $m = r = 2$ is essentially the same reconstruction that gives the non-oscillatory second order accurate scheme of [15].

4. **Scalar conservation laws.** The abstract form of our scheme calls in (1.14b) for the evaluation of the exact solution in the small of the IVP (1.1) with the initial data $R(x; v^n)$. This step is followed by the cell-averaging operation in (1.14c) which results in the conservation form (1.16). Thus we are spared the task of having to compute a global solution. All we need to do is evaluate

$$\bar{f}_{j+\frac{1}{2}} = \frac{1}{\tau}\int_0^\tau f(v_h(x_{j+\frac{1}{2}}, t_n + \eta))d\eta. \tag{4.1}$$

To simplify our notation let us denote $v_h(x, t_n + t)$ by $v(x,t)$. Thus $v(x,t)$ is the solution of

$$v_t + f(v)_x = 0 \tag{4.2a}$$

with the piecewise-polynomial initial data

$$v(x,0) = R(x; v^n) = \sum_{l=0}^{r-1} b_{j,l}(x - x_j)^l/l! \quad \text{for } x_{j-\frac{1}{2}} \le x < x_{j+\frac{1}{2}} \tag{4.2b}$$

in the time strip $-\infty < x < \infty$, $0 \le t \le \tau$, τ small.

The solution $v(x,t)$, for sufficiently small τ, is composed of sections of smoothness seperated by "fans" that emerge from the discontinuities at $\{x_{i+\frac{1}{2}}\}$. We use here the term "fan" loosely, allowing a "fan" with zero spread which is just a curve. In the linear case discontinuities propagate along characteristic curves; in this case all the "fans" are just curves. In the nonlinear case the "fans" with zero spread are shock curves, while "fans" with positive spread are rarefaction fans - or possibly a succession of rarefaction fans seperated by contact shocks in the case of non-convex flux. We denote by $v_j(x,t)$ the section of smoothness of $v(x,t)$ that is connected to the polynomial data in $(x_{j-\frac{1}{2}},\ x_{j+\frac{1}{2}})$.

A global description of $v(x,t)$ can be quite complicated. Fortunately all we need is $v(x_{j+\frac{1}{2}}, t)$ for small t, which can be easily described in terms of $v_j(x,t)$, $v_{j+1}(x,t)$ and the "fan" eminating from $x = x_{j+\frac{1}{2}}$ at $t = 0$ as follows. If for $t > 0$ the "fan"

stays to the right of $x = x_{j+\frac{1}{2}}$ then $v(x_{j+\frac{1}{2}}, t) = v_j(x_{j+\frac{1}{2}}, t)$; if this "fan" stays to the left of $x = x_{j+\frac{1}{2}}$ then $v(x_{j+\frac{1}{2}}, t) = v_{j+1}(x_{j+\frac{1}{2}}, t)$; if the "fan" covers $x = x_{j+\frac{1}{2}}$, then $v(x_{j+\frac{1}{2}}, t) = \text{constant} = V(0; v_j(x_{j+\frac{1}{2}}, 0), v_{j+\frac{1}{2}}(x_{j+\frac{1}{2}}, 0))$. Here $V(x/t; u_L, u_R)$ denotes the self-similar solution of the Riemann problem

$$u_t + f(u)_x = 0,\ u(x,0) = \begin{cases} u_L & x < 0 \\ u_R & x > 0, \end{cases} \tag{4.3}$$

with constant u_L and u_R. We note that the "fan" covers $x = x_{j+\frac{1}{2}}$ only when it contains a sonic centered rarefaction wave (i.e. one that includes a point for which $f' = 0$); this wave retains its self-similar form as long as it does not interact with shocks. Therefore if we choose τ sufficiently small so that no shock crosses $x = x_{j+\frac{1}{2}}$ for $0 < t \leq \tau$, we can express $f(v(x_{j+\frac{1}{2}}, t))$ by

(4.4)

$$f(v(x_{j+\frac{1}{2}}, t)) = \begin{cases} f(v_j(x_{j+\frac{1}{2}}, t)) & \text{"fan" stays to the right of } x = x_{j+\frac{1}{2}} \\ f^R(v_j(x_{j+\frac{1}{2}}, 0), v_{j+1}(x_{j+\frac{1}{2}}, 0)) & \text{"fan" covers } x = x_{j+\frac{1}{2}}. \\ f(v_{j+1}(x_{j+\frac{1}{2}}, t)) & \text{"fan" stays to the left of } x = x_{j+\frac{1}{2}} \end{cases}$$

Here f^R denotes the flux at $x = 0$ of the solution to the Riemann problem (4.3), i.e.

$$f^R(u_1, u_2) = f(V(0; u_1, u_2)); \tag{4.5}$$

using the formula in [23] it can be expressed by

$$f^R(u_1, u_2) = \begin{cases} \min_{u_1 \leq u \leq u_2} f(u) & \text{if } u_1 \leq u_2 \\ \max_{u_1 \geq u \geq u_2} f(u) & \text{if } u_1 > u_2. \end{cases} \tag{4.6a}$$

When $f(u)$ is a convex function of u, i.e. $f''(u) > 0$, $f(u)$ may have only a single local extremum which is a minimum; let us denote its location by u_s. Using this fact in (4.6a) we can express $f^R(u_1, u_2)$ in the convex case by

$$f^R(u_1,u_2)=\begin{cases} f(u_1) & \text{if } u_s < u_1 \le u_2 \\ f(u_s) & \text{if } u_1 \le u_s \le u_2 \\ f(u_2) & \text{if } u_1 \le u_2 < u_s \\ f(u_1) & \text{if } u_1 > u_2 \text{ and } \tilde{a}(u_1,u_2) > 0 \\ f(u_2) & \text{if } u_1 > u_2 \text{ and } \tilde{a}(u_1,u_2) \le 0. \end{cases} \tag{4.6b}$$

Here

$$\tilde{a}(u_1,u_2) = [f(u_2)-f(u_1)]/(u_2-u_1) \tag{4.7}$$

is the speed of the shock with $u_L = u_1$ and $u_R = u_2$ in (4.3). We remark that (4.4) is deliberately formulated in terms of $f(v(x_{j+\frac{1}{2}},t))$ rather than $v(x_{j+\frac{1}{2}},t)$ in order to remove ambiguity in the definition when v is discontinuous at $x_{j+\frac{1}{2}}$. The continuity of $f(v)$ in this case follows from the Rankine-Hugoniot relation for a stationary shock.

We turn now to derive a simple but adequate approximation to the numerical flux (4.1), which is

$$\bar{f}_{j+\frac{1}{2}} = \frac{1}{\tau}\int_0^\tau f(v(x_{j+\frac{1}{2}},t))dt \tag{4.8}$$

with the integrand given by (4.4). Note that the integrand is a smooth function of t.

The first step is to discretize the integral in (4.8) by using a numerical quadrature

$$\frac{1}{\tau}\int_0^\tau g(t)dt = \sum_{k=0}^{K} \alpha_k\, g(\beta_k\tau) + O(\tau^r); \tag{4.9}$$

thus

$$\bar{f}_{j+\frac{1}{2}} \approx \sum_{k=0}^{K} \alpha_k f(v(x_{j+\frac{1}{2}},\beta_k\tau)). \tag{4.10}$$

The second step is to approximate $v_j(x,t)$ in (4.4) by its Taylor expansion which is obtained by the following local Cauchy-Kowalewski procedure. We start by expressing $\partial^l v(x,0)/\partial x^l$ at x_j by

$$\frac{\partial^l v(x_j,0)}{\partial x^l} = \begin{cases} b_{j,l} & for\ 0 \le l \le r-1 \\ 0 & for\ l \ge r. \end{cases} \tag{4.11a}$$

Next we use (4.11a) to evaluate

$$\frac{\partial^l v}{\partial x^k \partial t^{l-k}}(x_j,0) \quad \text{for all } l \text{ and } 0 \le k \le l \tag{4.11b}$$

by taking derivatives of the partial differential equation (1.1a) in the following ordered way

$$\begin{cases} v_t &= -f' v_x \\ v_{xt} &= -[f''(v_x)^2 + f' v_{xx}] \\ v_{tt} &-[f'' v_t v_x + f' v_{xt}] \\ v_{xxt} &= -[f'''(v_x)^3 + 3f'' v_x v_{xx} + f' v_{xxx}] \\ v_{xtt} &= -[f'''(v_x)^2 v_t + f''(2v_x v_{xt} + v_t v_{xx}) + f' v_{xxt}] \\ v_{ttt} &= -[f'''(v_t)^2 v_x + f''(2v_t v_{xt} + v_x v_{tt}) + f' v_{xtt}] \\ \text{etc.} \end{cases} \tag{4.11c}$$

and then compute (4.11b) by successively evaluating the RHS of (4.11c); note that this procedure always uses known values which are either initially given by (4.11a) or previously computed in the algorithm (4.11c). We observe that

$$\tilde{v}_j(x,t) = \sum_{l=0}^{r-1} \sum_{k=0}^{l} \frac{\partial^l v(x_j,0)}{\partial x^k \partial t^{l-k}} \cdot \frac{(x-x_j)^k}{k!} \frac{t^{l-k}}{(l-k)!} \tag{4.12a}$$

satisfies

$$\tilde{v}_j(x,0) = v_j(x,0) = v(x,0) \quad \text{for } x_{j-\frac{1}{2}} < x < x_{j+\frac{1}{2}}, \tag{4.12b}$$

and that

$$\tilde{v}_j(x,t) = v_j(x,t) + O(h^r), \tag{4.12c}$$

wherever $v_j(x,t)$ is well defined.

The last step in our derivation of the numerical flux is to approximate $f(v(x_{j+\frac{1}{2}},t))$ in (4.4) by

$$f(v(x_{j+\frac{1}{2}},t)) \approx f^R(\tilde{v}_j(x_{j+\frac{1}{2}},t),\ \tilde{v}_{j+1}(x_{j+\frac{1}{2}},t)), \tag{4.13}$$

where f^R is (4.5) - (4.6). The resulting numerical scheme is

$$v_j^{n+1} = v_j^n - \lambda(\bar{f}_{j+\frac{1}{2}} - \bar{f}_{j-\frac{1}{2}}) \tag{4.14a}$$

$$\bar{f}_{j+\frac{1}{2}} = \sum_{k=0}^{K} \alpha_k f^R(\tilde{v}_j(x_{j+\frac{1}{2}},\beta_k\tau), \tilde{v}_{j+1}(x_{j+\frac{1}{2}},\beta_k\tau)). \tag{4.14b}$$

In the following we show that the numerical flux $\bar{f}_{j+\frac{1}{2}}$ in (4.14b) is an adequate approximation to the "abstract numerical flux" (4.1).

We start by proving that the scheme (4.14) is r-th order accurate in the sense of (1.8). To do so we take in (4.14) $v_j^n = \bar{u}(x_j,t_n)$ where $u(x,t)$ is a smooth (either globally or locally) solution of (1.1) and show that

$$\bar{f}_{j+\frac{1}{2}} = \frac{1}{\tau}\int_0^\tau f(u(x_{j+\frac{1}{2}},t_n+\eta))d\eta + O(h^r). \tag{4.15}$$

When we apply the reconstruction R to $\bar{u}^n$ we get from (3.9) and (3.20) that

$$\frac{d^k}{dx^k}R(x;\bar{u}^n) = \frac{\partial^k}{\partial x^k}u(x,t_n) + O(h^{r-k}) \quad \text{for } 0 \le k \le r-1. \tag{4.16a}$$

Consequently it follows from the Cauchy-Kowalewski procedure (4.11) - (4.12) and $\tau = O(h)$ that

$$\tilde{v}_i(x_{j+\frac{1}{2}},t) = u(x_{j+\frac{1}{2}},t_n+t) + O(h^r) \quad \text{for } i = j, j+1 \tag{4.16b}$$

$f^R(u_1,u_2)$ is Lipschitz-continuous with respect to u_1 and u_2, and it is consistent with $f(u)$ in the sense that $f^R(u,u) = f(u)$; therefore

$$f^R(u_1,u_2) = f(u) + O(|u-u_1| + |u-u_2|). \tag{4.16c}$$

Applying (4.16c) to (4.16b) we get that

(4.16d) $$f^R(\tilde{v}_j(x_{j+\frac{1}{2}},t),\ \tilde{v}_{j+1}(x_{j+\frac{1}{2}},t)) = f(u(x_{j+\frac{1}{2}},t_n+t)) + O(h^r).$$

Finally using the assumed smoothness of $u(x,t)$ and the order of accuracy of the numerical quadrature (4.9) we obtain (4.15).

Next we consider the constant coefficient case

(4.17a) $$v_t + av_x = 0, \qquad a = \text{ constant}.$$

Here the "fan" in (4.4) is the characteristic line

(4.17b) $$x_{j+\frac{1}{2}}(t) = x_{j+\frac{1}{2}} + at$$

and

(4.17c) $$v_j(x,t) = v(x-at,0) = R(x-at;v^n) \text{ for } x_{j-\frac{1}{2}}(t) < x < x_{j+\frac{1}{2}}(t).$$

Since $v_j(x,t)$ in (4.17c) is a polynomial of degree $r-1$ in $(x-at)$ we get that

(4.17d) $$\frac{\partial^l v}{\partial x^k \partial t^{l-k}} \equiv 0 \text{ for } l \geq r;$$

this implies in (4.11) - (4.12) that

(4.18a) $$\tilde{v}_j(x,t) \equiv v_j(x,t).$$

Hence

(4.18b) $$f^R(\tilde{v}_j(x_{j+\frac{1}{2}},t),\ \tilde{v}_{j+1}(x_{j+\frac{1}{2}},t)) \equiv f(v(x_{j+\frac{1}{2}},t)).$$

Since the numerical quadrature (4.9) is exact for polynomials of degree $r-1$ we get that the numerical flux $\tilde{f}_{j+\frac{1}{2}}$ (4.14b) is identical to (4.8). It follows then that the

numerical scheme (4.14) in the constant coefficient case is the "abstract scheme" (1.14), (1.16), i.e.

$$v_j^{n+1} = \bar{R}(x_j - a\tau; v^n). \tag{4.18c}$$

We observe that since the "fans" in the solution $v(x,t)$ in the constant coefficient case have zero spread, the evaluation of $f(v(x_{j+\frac{1}{2}},t))$ in (4.4) involves only the smooth parts of the solution $v_i(x,t)$. The "fans" in the numerical approximation mark the domain of validity of the Taylor expansions $\tilde{v}_j(x,t)$. Therefore the only role of the Riemann solver in the formulation of the numerical flux (4.14b)

$$f^R(\tilde{v}_j(x_{j+\frac{1}{2}},t), \tilde{v}_{j+1}(x_{j+\frac{1}{2}},t)) = \begin{cases} f(\tilde{v}_j(x_{j+\frac{1}{2}},t)) & \text{if } a > 0 \\ f(\tilde{v}_{j+1}(x_{j+\frac{1}{2}},t)) & \text{if } a < 0 \end{cases} \tag{4.19}$$

is to serve as a pointer, i.e. to identify whether $x = x_{j+\frac{1}{2}}$ falls into the domain of validity of $\tilde{v}_j$ or into that of $\tilde{v}_{j+1}$. Since $\tilde{v}_i(x_{j+\frac{1}{2}},t) = v(x_{j+\frac{1}{2}} - at, 0)$, the use of the Cauchy-Kowalewski procedure is equivalent to that of a characteristic method that traces the characteristic curve through $(x_{j+\frac{1}{2}},t)$ to the initial data.

Next we consider the scalar IVP (1.1) with convex $f(u)$ and smooth initial data $u_0(x)$ and we show that the above interpretation of the numerical approximations applies to this nonlinear case as well. The numerical solution $v_j^n \approx \bar{u}(x_j,t_n)$ typically forms a monotone transition of 1 - 2 points across shocks and stays close to $\bar{u}(x_j,t_n)$ in the smooth parts of the solution. (see the numerical experiments with $u_t + uu_x = 0$ and $u(x,0) = \sin \pi x$ in section 7). Let us now examine the discontinuities of $R(x; v^n)$ at $\{x_{j+\frac{1}{2}}\}$ and the nature of the "fans" eminating from these points. Relation (4.16b) with $t = 0$ shows that the jump at $x_{j+\frac{1}{2}}$ in the smooth part of the solution is of the order of the local error, say $O(h^p)$ with $0 < p \leq r$. Hence the "fan" emerging from $x_{j+\frac{1}{2}}$ in a region of smoothness is either a shock curve or a rarefaction fan with $O(h^p)$ spread. On the other hand in the vicinity of shocks of $u(x,t_n)$ the size of this jump is 0(1); however the "fan" is necessarily a shock curve.

We see therefore that the global picture is very similar to that of the constant coefficient case, i.e. the "fans" separating $\{v_j(x,t)\}$ are either shock curves with zero spread or rarefaction fans with $O(h^p)$ spread (these can be thought of as "blurred" characteristic curves); these "fans" are the boundaries of the domains of validity of the Taylor expansions $\tilde{v}_i(x,t)$. We note that the value given by $\tilde{v}_i(x_{j+\frac{1}{2}},t)$ differs by $O(\tau^r)$ from that obtained by solving the nonlinear characteristc relation for v

$$v = R(x_{j+\frac{1}{2}} - a(v)t; v^n). \tag{4.20}$$

Hence the use of the local Cauchy-Kowalewski procedure is again computationally equivalent to tracing the characteristic curve through $(x_{j+\frac{1}{2}},t)$ to the initial data. Since the evaluation of $f(v(x_{j+\frac{1}{2}},t))$ in (4.4) essentially involves only $\tilde{v}_j(x_{j+\frac{1}{2}},t)$ and $\tilde{v}_{j+1}(x_{j+\frac{1}{2}},t)$, the role of the Riemann solver in the numerical flux (4.14b) is again that of a pointer, i.e. to identify to which domain of validity $x = x_{j+\frac{1}{2}}$ belongs to. This suggests that f^R in (4.14b) can be adequately replaced by the simpler expression f^{ROE} which corresponds to Roe's approximate solution of the Riemann problem (see [25], [14]):

$$f^{ROE}(u_1,u_2) = \frac{1}{2}[f(u_1) + f(u_2) - |\bar{a}(u_1,u_2)|(u_2 - u_1)]$$

$$= \begin{cases} f(u_1) & \text{if } \bar{a}(u_1,u_2) > 0 \\ f(u_2) & \text{if } \bar{a}(u_1,u_2) \le 0, \end{cases} \tag{4.21}$$

where $\bar{a}(u_1,u_2)$ is defined by (4.7). Observe that f^{ROE} in (4.21) satisfies (4.16c) and therefore the modified scheme remains r-th order accurate.

The heuristic analysis presented above is applicable only when all the discontinuities in the solution to the IVP (1.1) are shocks; discontinuities that are not shocks may be present in the solution either by being introduced through the initial data $u_0(x)$ or as a result of a shock-snock interaction in the non-convex case. Clearly f^{ROE} in its form (4.21a) should not be used when the solution contains

a sonic rarefaction wave since it admits any discontinuity with $\bar{a}(u_L, u_R) = 0$ as a stationary solution. This problem is well known and there are many ways to overcome it (see [13], [26], [9] and Section 7).

In Section 7 we present numerical experiments testing the performance of the scheme (4.14) in the solution of the Riemann IVP (4.3) where $f(u)$ is non-convex and $\bar{a}(u_L, u_R) = 0$. In all these experiments, as well as in others not reported here, we have found the scheme to develop the correct structure of the solution.

5. Systems of conservation laws. In this section we extend the reconstruction algorithm of Section 3 and the solution-in-the-small procedure of Section 4 to the case of hyperbolic systems of conservation laws.

As always we are interested only in "computable" solutions and therefore assume that the initial data $u_0(x)$ in (1.1b) are such that $u(x,t)$, which is a vector function of m components $u = (u_1, ..., u_m)^T$, is a piecewise smooth function of x with a finite number of discontinuities. Given cell-averages $\bar{u}_j^n = \bar{u}(x_j, t_n)$, it seems natural from the point of view of approximation theory to reconstruct $u(x, t_n)$ by applying the scalar reconstruction R to each of the scalar component $\bar{u}_k^n$, i.e.

$$\mathbf{R}(x; \bar{u}^n) = (R(x; \bar{u}_1^n), ..., R(x; \bar{u}_m^n))^T; \tag{5.1}$$

here $\mathbf{R}$ denotes vector-reconstruction. However, componentwise reconstruction seems natural only if we disregard the time-dependence of $u(x,t)$ which allows discontinuities in the solution to collide with each other.

We recall that the scalar reconstruction is non-oscillatory only if discontinuities are seperated by at least $r+1$ points of smoothness, where r is the order of accuracy. Consequently the component-by-component reconstruction (5.1) may cease to be non-oscillatory around the discrete set of points (x_c, t_c) where discontinuities of $u(x,t)$ interact. In the following we describe an algorithm to reconstruct $u(x, t_n)$ from $\bar{u}^n$ which avoids this difficulty by decomposing $\bar{u}^n$ into m locally defined scalar characteristic variables.

We start by examining the constant coefficient case $f(u) = Au$, where A is a constant $m \times m$ matrix

$$u_t + Au_x = 0 \tag{5.2a}$$

$$u(x,0) = u_0(x). \tag{5.2b}$$

We note that the eigenvalues $\{a_k\}$ as well as the eigenvectors $\{r_k\}$, $\{l_k\}$ are also constant. We assume that

(5.3a) $$a_1 < a_2 < \cdots < a_m$$

(5.3b) $$l_i r_j = \delta_{ij}.$$

We define the k-th characteristic variable w^k by

(5.4a) $$w^k = l_k u.$$

It follows then from (5.3b) that

(5.4b) $$u = \sum_{k=1}^{m} w^k r_k.$$

Multiplying (5.2) from the left by l_k we see that $w^k(x,t)$ satisfies the following scalar IVP

(5.5a) $$(w^k)_t + a_k (w^k)_x = 0$$

(5.5b) $$w^k(x,0) = l_k u_0(x) \equiv w_0^k(x),$$

the solution to which is

(5.5c) $$w^k(x,t) = w_0^k(x - a_k t).$$

Using (5.4b) and (5.5c) we can express the solution $u(x,t)$ of the constant coefficient IVP (5.2) by

$$u(x,t) = \sum w_0^k(x - a_k t) r_k.$$

Let us now consider the following initial data in (5.2b)

(5.6a) $$u_0(x) = \begin{cases} u_L & x < x_L \\ u_M & x_L \le x \le x_R \\ u_R & x_R < x \end{cases}.$$

First let us consider the case $x_L = x_R = 0$ which is the Riemann IVP (4.3). The solution $u(x,t)$ is a self-similar solution $V(x/t; u_L, u_R)$ of the following form

$$u(x,t) = V(x/t; u_L, u_R) = \begin{cases} u_L & x/t < a_1 \\ u^k & a_k < x/t < a_{k+1},\ 1 \le k \le m-1, \\ u_R & a_m < x/t \end{cases} \tag{5.6b}$$

where

$$u^k = u_L + \sum_{i=1}^{k} (w_R^i - w_L^i) r_i, \quad 1 \le k \le m-1. \tag{5.6c}$$

In the case $x_R > x_L$ in (5.6a) the solution $u(x,t)$, for t small, is

$$u(x,t) = \begin{cases} V(\frac{x-x_L}{t}; u_L, u_M) & \text{for } x < x_L + a_m t \\ u_M & \text{for } x_L + a_m t \le x \le x_R + a_1 t. \\ V(\frac{x-x_R}{t}; u_M, u_R) & \text{for } x_R + a_1 t < x \end{cases} \tag{5.6d}$$

As t increases, the discontinuity in the k-th characteristic field originating at $x = x_L$ will eventually collide with any discontinuity in the l-th field, $l = 1, ..., k-1$ originating at $x = x_R$.

The example (5.6) demonstrates the difficulty encountered in using the componentwise reconstruction (5.1). We may get oscillations for small t in both (5.6b) and (5.6d) since the discontinuities are too close due to the self-similar nature of the solution to the Riemann problem. Later on we may get more oscillations in (5.6d) as discontinuities collide.

We observe that there are no such problems with $w^k(x,t) = w_0^k(x - a_k t)$. Therefore it makes sense to use the scalar reconstruction $R(x; \bar{w}^k)$ to define

$$\mathbf{R}(x; \bar{u}) = \sum_{k=1}^{m} R(x; \bar{w}^k) r_k \tag{5.7a}$$

where

$$\bar{w}^k = l_k \bar{u}. \tag{5.7b}$$

We generalize (5.7) to the nonlinear system case by using locally defined characteristic variables. To reconstruct u from $\bar{u}$ in $(x_{j-\frac{1}{2}},\ x_{j+\frac{1}{2}})$ we define

$$\text{(5.8a)} \qquad \mathbf{R}(x;\bar{u}) = \sum_{k=1}^{m} R(x;\bar{w}^k(\bar{u}_j))r_k(\bar{u}_j) \quad \text{for } x_{j-\frac{1}{2}} \le x < x_{j+\frac{1}{2}},$$

where the mesh function $\bar{w}^k(\bar{u}_j) = \{\bar{w}_i^k(\bar{u}_j)\}$ is defined by

$$\text{(5.8b)} \qquad \bar{w}_i^k(\bar{u}_j) = l_k(\bar{u}_j)\bar{u}_i \quad \text{for } j-p \le i \le j+p;$$

here p is the desired order of reconstruction.

In Section 7 we present calculations for the Euler equations of gas dynamics with the initial data (5.6a). The results of these calculations (as well as those of shocks reflecting from a wall) demonstrate that the reconstruction (5.8) works well also in the nonlinear case.

We turn now to describe our scheme in the case of hyperbolic systems of conservation laws. This scheme is identical in form to (4.14):

$$\text{(5.9a)} \qquad v_j^{n+1} = v_j^n - \lambda(\bar{f}_{j+\frac{1}{2}} - \bar{f}_{j-\frac{1}{2}})$$

$$\text{(5.9b)} \qquad \bar{f}_{j+\frac{1}{2}} = \sum_{k=0}^{K} \alpha_k f^R(\tilde{v}_j(x_{j+\frac{1}{2}},\beta_k\tau), \tilde{v}_{j+1}(x_{j+\frac{1}{2}},\beta_k\tau)).$$

The derivation of (5.9), although different in some details, is basically the same as the one presented in Section 4 for the scalar case. Rather than repeating ourselves we shall use the formulae of Section 4 (which are to be interpreted here in a vector sense), and point out the differences whenever they do exist.

The problem to be solved in the "solution-in-the-small" step of the algorithm (1.14b) is as before (4.2). The general structure of the solution $v(x,t)$ is similar to that of the scalar case, i.e. it is composed of sections of smoothness seperated by "fans" eminating from the discontinuities at $\{x_{j+\frac{1}{2}}\}$. As in the scalar case we can use a local Cauchy-Kowalewski procedure to approximate $v_j(x,t)$, the section of smoothness of $v(x,t)$ that is connected to the polynomial initial data in

$(x_{j-\frac{1}{2}}, x_{j+\frac{1}{2}})$, by $\tilde{v}_j(x,t)$ in (4.12) to any desired order of accuracy. Since $f(u)$ is now a vector, $f'(u)$ is a matrix, $f''(u)$ is a tensor and so on; consequently (4.11c) has to be replaced by a much more complicated expression. Rather than doing this we shall present in Section 6 an algorithm to carry out the Cauchy-Kowalewski procedure in the specific case of the Euler equations for gas dynamics.

Next we consider the "fan" that eminates from the discontinuity at $x_{j+\frac{1}{2}}$. As in the scalar case this "fan" starts at $t = 0$ as a self-similar solution to the Riemann problem (4.3), which in the system case is a packet of m fans corresponding to the different characteristic fields. A major difference from the scalar case is that (except when the initial data in (4.2b) are piecewise constant) the "fan" emerging from $x_{j+\frac{1}{2}}$ at $t = 0$ immediately loses its self-similar nature. Therefore it is no longer possible to express $v(x_{j+\frac{1}{2}}, t)$ in a simple closed form as we did in (4.4). However $v(x_{j+\frac{1}{2}}, t)$ can be expressed to any desired order of accuracy via a local Taylor expansion of the various curves in the "fan" and the states in between (We refer the interested reader to [1] where Ben-Artzi and Falcowitz describe such an expansion for the Euler equations of gas dynamics). Thus as in the scalar case, although at a considerably more effort, it is possible to obtain an explicit expression that approximates the "abstract numerical flux" (4.8) to any desired order of accuracy.

We turn now to show that the numerical scheme (5.9) is an adequate approximation to the "abstract scheme" (1.16). First we observe that relations (4.16) hold also for the system case; therefore (4.15) follows in exactly the same way as in the scalar case and consequently the scheme (5.9) is likewise r-th order accurate.

Next we consider the scheme in the constant coefficient case (5.2). Since both the PDE (1.1a) and the scheme (5.9) decouple into m scalar relations for the characteristic variables w^k in (5.4a), we can apply the analysis of the scalar constant coefficient case to systems in a characteristic-wise fashion. It follows then from (4.17) - (4.18) that the numerical flux (5.9b) is exact and that the numerical scheme (5.9)

is identical to the "abstract scheme" (1.16). Let us examine now the structure of the solution $v(x,t)$: The "fan" eminating from $x_{j+\frac{1}{2}}$ has the same form as (5.6b) except that u_L, u^k and u_R are now functions of x and t. The section of smoothness $x_{j-\frac{1}{2}} + a_m t < x < x_{j+\frac{1}{2}} + a_1 t$ is also the domain of validity of the Taylor expansion $\tilde{v}_j(x,t)$. We note however that $l_k\ \tilde{v}_j(x,t)$, which is the Taylor expansion of $w_j^k(x,t)$, is valid in the larger domain $x_{j-\frac{1}{2}} + a_k t < x < x_{j+\frac{1}{2}} + a_k t$. Next let us examine the role of f^R in formulating the numerical flux (5.9b):

$$(5.10a) \qquad f^R(\tilde{v}_j(x_{j+\frac{1}{2}},t), \tilde{v}_{j+1}(x_{j+\frac{1}{2}},t)) = \sum_k (a_k)^+ [l_k\ \tilde{v}_j(x_{j+\frac{1}{2}},t)] r_k + \sum_k (a_k)^- [l_k\ \tilde{v}_{j+1}(x_{j+\frac{1}{2}},t)] r_k;$$

where

$$(5.10b) \qquad (a_k)^+ = \max(0, a_k), \quad (a_k)^- = \min(0, a_k).$$

We see from (5.10) that as in the scalar case the role of f^R is that of a pointer, i.e. to identify for each characteristic variable $w^k = l_k v$ to which domain of validity of $\{l_k\ \tilde{v}_i\}$ does $x = x_{j+\frac{1}{2}}$ belong to. Since $l_k\ \tilde{v}_i(x_{j+\frac{1}{2}},t) = l_k v(x_{j+\frac{1}{2}} - a_k t, 0)$, the use of the Cauchy-Kowalewski procedure in this fashion is again computationally equivalent to that of a characteristic method.

In the following we argue that except for the discrete set $\{(x_c,t_c)\}$ of interactions, the above interpretation can be applied to the nonlinear case as well. Unlike the scalar case we do not consider in this paper the "non-convex case" for systems and assume that each characteristic field is either genuinely nonlinear or linearly degenerate (see [19]). When we consider the IVP (4.2) in the context of the numerical scheme where $v(x,0) = R(x;v^n)$ we see that the "fans" in the solution $v(x,t)$ are related to the global structure of $u(x,t_n)$ in the following way (see figure 14 and figure 16): When $u(x.t_n)$ is smooth, the "fan" has the basic structure of the constant coefficient case linearized around $u(x_{j+\frac{1}{2}},t_n)$, except that the k-waves may have a

spread of $O(h^p)$. When $x_{j+\frac{1}{2}}$ is in the vicinity of a shock of $u(x,t_n)$, the "fan" is essentially a shock wave with small perturbations in the other fields. We see that typically (excluding interactions) the "fan" eminating from $x_{j+\frac{1}{2}}$ in the solution $v(x,t)$ is degenerate in the sense that except possibly for a single large shock (or a contact-discontinuity) all the waves in it are weak. This heuristic analysis suggests that $f(v(x_{j+\frac{1}{2}},t))$ can be adequately approximated by a local Roe's linearization; this linearization is exact for a single shock or a contact-discontinuity and amounts to a characteristic approximation for weak waves.

As in the scalar case, f^{ROE} is obtained by a local linearization with respect to a particular average $\hat{u} = \hat{u}(u_L, u_R)$ for which

$$f(u_R) - f(u_L) = A(\hat{u})(u_R - u_L). \tag{5.11a}$$

f^{ROE} is defined as the flux at $x = 0$ of the solution to the constant coefficient Riemann IVP:

$$u_t + A(\hat{u})u_x = 0$$

$$u(x,0) = \begin{cases} u_L & x < 0 \\ u_R & x > 0, \end{cases}$$

which can be expressed as

$$f^{ROE}(u_L, u_R) = \frac{1}{2}\left[f(u_L) + f(u_R) - \sum_{k=1}^{m} \delta_k(u_L, u_R)|a_k(\hat{u})|r_k(\hat{u},)\right] \tag{5.11b}$$

where

$$\delta_k(u_L, u_R) = l_k(\hat{u})(u_R - u_L); \tag{5.11c}$$

here $a_k(\hat{u})$, $l_k(\hat{u})$ and $r_k(\hat{u})$ are evaluated with respect to the Jacobian matrix $A(\hat{u})$. The derivation of Roe's Riemann solver is well documented in the literature (see [25], [8], [9], [14]). In Section 6 we describe f^{ROE} for the Euler equations of gas dynamics

Finally let us examine the performance of the scheme (5.9) during an interaction of discontinuities in the solution $u(x,t)$ of the IVP (1.1). We observe that it takes some time until the outcoming waves can be properly described on the computational grid. Till then $R(x;v^n)$, which is based on polynomial interpolation, can only be a crude approximation to $u(x,t_n)$. Under these circumstances we expect the "fans" in the solution $v(x,t)$ (4.12) that originate from discontinuities in the interaction zone of $u(x,t_n)$, to be adequately approximated by the self-similar solution to the local Riemann problem. We note that once the outcoming waves are properly resolved on the computational grid, the previous analysis applies.

In Section 7 we present numerical experiments where the scheme (5.9) with f^R replaced by f^{ROE} (5.11) is applied to an interaction problem for the Euler equations of polytropic gas. In all these experiments the scheme (5.9) has developed the correct structure of the solution.

We remark that the scheme (5.9) with f^{ROE} in its form (5.11b) admits a stationary "expansion shock" as its steady solution. This can be easily rectified by adding entropy viscosity terms for the genuinely nonlinear characteristic fields. (See [13], [14], [9]).

6. Euler equations of gas dynamics. In this section we describe how to apply the scheme (5.1) to the Euler equations of gas dynamics for a polytropic gas:

$$u_t + f(u)_x = 0 \tag{6.1a}$$

$$u = (\rho, m, E)^T \tag{6.1b}$$

$$f(u) = qu + (0, P, qP)^T \tag{6.1c}$$

$$P = (\gamma - 1)(E - \frac{1}{2}\rho q^2). \tag{6.1d}$$

Here ρ, q, P and E are the density, velocity, pressure and total energy, respectively; $m = \rho q$ is the momentum and γ is the ratio of specific heats.

The eigenvalues of the Jacobian matrix $A(u) = \partial f/\partial u$ are

$$a_1(u) = q - c, \quad a_2(u) = q \quad a_3(u) = q + c \tag{6.2a}$$

where $c = (\gamma P/\rho)^{\frac{1}{2}}$ is the sound speed.

The corresponding right-eigenvectors are

$$r_1(u) = \begin{pmatrix} 1 \\ q - c \\ H - qc \end{pmatrix}, r_2(u) = \begin{pmatrix} 1 \\ q \\ \frac{1}{2}q^2 \end{pmatrix}, r_3(u) = \begin{pmatrix} 1 \\ q + c \\ H + qc \end{pmatrix}; \tag{6.2b}$$

here

$$H = (E + P)/\rho = c^2/(\gamma - 1) + \frac{1}{2}q^2 \tag{6.2c}$$

is the enthalpy.

To compute $\{l_k(u)\}$ which is bi-orthonormal to $\{r_k(u)\}$ in (6.2b), we first form the matrix $\mathbf{T}(u)$, the columns of which are the right-eigenvectors in (6.2b)

$$\mathbf{T}(u) = (r_1(u), r_2(u), r_3(u))$$

and then define $l_k(u)$ to be the k-th row in $\mathbf{T}^{-1}(u)$, the inverse of $\mathbf{T}(u)$. We get

$$\text{(6.2d)} \qquad \begin{cases} l_1(u) = \frac{1}{2}(b_2 + q/c, -b_1 q - 1/c, b_1) \\ l_2(u) = (1 - b_2, b_1 q, -b_1) \\ l_3(u) = \frac{1}{2}(b_2 - q/c, -b_1 q + 1/c, b_1) \end{cases}$$

where

$$\text{(6.2e)} \qquad b_1 = (\gamma - 1)/c^2$$

$$\text{(6.2f)} \qquad b_2 = \frac{1}{2} q^2 b_1 .$$

Given $\{v_j^n\}$, approximation to $\{\bar{u}(x_j, t_n)\}$, we use (6.2d) - (6.2f) to evaluate the locally defined characteristic variables (5.8b)

$$\text{(6.3a)} \qquad \bar{w}_i^k(v_j^n) = l_k(v_j^n) v_i^n \quad \text{for } i = j - r, ..., j + r \text{ and } k = 1, 2, 3.$$

Next we apply our scalar reconstruction algorithm to each of the locally defined characteristic variables in (6.3a). The scalar reconstruction $R(x; \bar{w})$ is described in an algorithmic form in an appendix; the output of this algorithm is in the form of the finite Taylor series in (4.2b). Thus we get for each characteristic variable in $(x_{j-\frac{1}{2}}, x_{j+\frac{1}{2}})$

$$\text{(6.3b)} \qquad R(x; \bar{w}^k(v^n)) = \sum_{l=0}^{r-1} b_{j,l}^k (x - x_j)^l / l!$$

Rearranging terms we can express the vector reconstruction (5.8a) by

$$\text{(6.3c)} \qquad \mathbf{R}(x; v^n) = \sum_{l=0}^{r-1} \vec{b}_{j,l} (x - x_j)^l / l!$$

where

$$\text{(6.3d)} \qquad \vec{b}_{j,l} = \sum_{k=1}^{3} b_{j,l}^k r_k .$$

Note that wherever the solution is smooth

$$\text{(6.3e)} \qquad \vec{b}_{j,l} = \frac{\partial^l}{\partial x^l} (\rho, m, E)^T \Big|_{x = x_j} + O(h^{r-l}) \qquad \text{for } 0 \le l \le r - 1.$$

We turn now to describe the Cauchy-Kowalewski procedure (4.4) - (4.5) for the Euler equations of gas dynamics. We start by using the reconstruction output (6.3c) to define (4.4a), i.e.

$$\frac{\partial^l v(x_j,0)}{\partial x^l} = \begin{cases} \vec{b}_{j,l} & \text{for } 0 \le l \le r-1 \\ 0 & \text{for } l \ge r. \end{cases} \tag{6.4a}$$

We find it convenient to express $\partial^l v(x_j,0)/\partial x^k \partial t^{l-k}$ in terms of derivatives of the 4-vector $Z = (\rho, m, P, q)^T$. For this purpose we use (6.4a) and the relations

$$m = \rho q$$

$$P = (\gamma - 1)(E - \frac{1}{2} qm)$$

to find the x-derivatives of q and P, by

$$\begin{cases} m_x = q\rho_x + \rho q_x \Rightarrow q_x = (m_x - q\rho_x)/\rho \\ P_x = (\gamma-1)[E_x - \frac{1}{2}(q_x m + q m_x)] \end{cases} \tag{6.4b}$$

$$\begin{cases} m_{xx} = \rho q_{xx} + 2\rho_x q_x + q\rho_{xx} \Rightarrow q_{xx} = (m_{xx} - q\rho_{xx} - 2q_x\rho_x)/\rho \\ P_{xx} = (\gamma-1)[E_{xx} - \frac{1}{2}(mq_{xx} + 2q_x m_x + q m_{xx})] \end{cases} \tag{6.4c}$$

and so on. Having evaluated $\partial^l Z(x_j,0)/\partial x^l$ for $0 \le l \le r-1$, we proceed to obtain the rest of the derivatives $\partial^l Z(x_j,0)/\partial x^k \partial t^{l-k}$, $0 \le l \le r-1$, $0 \le k \le l$ by differentiating the PDE's

$$\rho_t + m_x = 0 \tag{6.5a}$$

$$m_t + (qm)_x + P_x = 0 \tag{6.5b}$$

$$P_t + qP_x + \gamma P u_x = 0 \tag{6.5c}$$

and the algebraic relation

$$m = q\rho \tag{6.5d}$$

in the following ordered way:

Compute $Z_t(x_j, 0)$ from

$$\text{(6.6a)} \qquad \begin{cases} \rho_t + m_x = 0 \\ m_t + q_x m + q m_x + P_x = 0 \\ P_t + q P_x + \gamma P q_x = 0 \\ \rho q_t + \rho_t q = m_t \end{cases};$$

compute $Z_{xt}(x_j, 0)$ from

$$\text{(6.6b)} \qquad \begin{cases} \rho_{xt} + m_{xx} = 0 \\ m_{xt} + 2q_x m_x + q m_{xx} + m q_{xx} + P_{xx} = 0 \\ P_{xt} + q P_{xx} + \gamma P q_{xx} + (1+\gamma) q_x P_x = 0 \\ \rho q_{xt} + \rho_x q_t + \rho_t q_x + q \rho_{xt} = m_{xt} \end{cases};$$

compute $Z_{tt}(x_j, 0)$ from

$$\text{(6.6c)} \qquad \begin{cases} \rho_{tt} + m_{xt} = 0 \\ m_{tt} + q m_{xt} + m q_{xt} + P_{xt} + (q_x m_t + q_t m_x) = 0 \\ P_{tt} + q P_{xt} + \gamma P q_{xt} + (q_t P_x + \gamma P_t q_x) = 0 \\ \rho q_{tt} + 2\rho_t q_t + q \rho_{tt} = m_{tt} \end{cases};$$

compute $Z_{xxt}(x_j, 0)$ from

$$\text{(6.6d)} \qquad \begin{cases} \rho_{xxt} + m_{xxx} = 0 \\ m_{xxt} + q m_{xxx} + m q_{xxx} + P_{xxx} + 3q_x m_{xx} + 3q_{xx} m_x = 0 \\ P_{xxt} + q P_{xxx} + \gamma P q_{xxx} + (2+\gamma) q_x P_{xx} + (1+2\gamma) q_{xx} P_x = 0 \\ \rho q_{xxt} + 2(\rho_x q_{xt} + \rho_{xt} q_x) + q \rho_{xxt} + \rho_{xx} q_t + \rho_t q_{xx} = m_{xxt} \end{cases};$$

compute $Z_{xtt}(x_j, 0)$ from

$$\text{(6.6e)} \qquad \begin{cases} \rho_{xtt} + m_{xxt} = 0 \\ m_{xtt} + q m_{xxt} + m q_{xxt} + P_{xxt} + 2(q_x m_{xt} + m_x q_{xt}) \\ \quad + (m_t q_{xx} + q_t m_{xx}) = 0 \\ P_{xtt} + q P_{xxt} + \gamma P q_{xxt} + (\gamma+1)[q_{xt} P_x + q_x P_{xt}] + q_t P_{xx} + \gamma P_t q_{xx} = 0 \\ \rho q_{xtt} + q \rho_{xtt} + \rho_x q_{tt} + q_x \rho_{tt} + 2(\rho_{xt} q_t + \rho_t q_{xt} = m_{xtt} \end{cases};$$

compute $Z_{ttt}(x_j,0)$ from

$$\text{(6.6f)}\qquad \begin{cases} \rho_{ttt}+m_{xtt}=0 \\ m_{ttt}+qm_{xtt}+mq_{xtt}+P_{xtt}+2(q_tm_{xt}+m_tq_{xt}) \\ \quad +(q_xm_{tt}+m_xq_{tt})=0 \\ P_{ttt}+qP_{xtt}+\gamma Pq_{xtt}+\gamma q_xP_{tt}+2(q_tP_{xt}+\gamma P_tq_{xt})+q_{tt}P_x=0 \\ \rho q_{ttt}+q\rho_{ttt}+3(\rho_tq_{tt}+q_t\rho_{tt})=m_{ttt} \end{cases},$$

and so on.

We note that one can differentiate the algebraic relation (6.1d) in order to obtain $\partial^l E(x_j,0)/\partial x^k\partial t^{l-k}$ in terms of the already evaluated derivatives of P,q and m, and use the derivatives of the conserved quantities ρ,m,E to compute $\tilde{v}_j(x,t)$ in (4.5). However, it is more convenient to evaluate the flux $f(u)$ and $f^R(u_1,u_2)$ in terms of ρ,q and P; since $\tilde{v}_j(x,t)$ is smooth and the scheme (5.1) is in conservation form we do not really have to worry about relation (4.12b). For this reason we use the first, third and fourth components of $\tilde{Z}_j(x,t)$

$$\text{(6.7)}\qquad \tilde{Z}_j(x,t)=\sum_{l=0}^{r-1}\sum_{k=0}^{l}\frac{\partial^l Z(x_j,0)}{\partial x^k\partial t^{l-k}}\cdot\frac{(x-x_j)^k}{k!}\,\frac{t^{l-k}}{(l-k)!}$$

to define $\tilde{\rho}_j(x,t)$, $\tilde{P}_j(x,t)$ and $\tilde{q}_j(x,t)$, respectively.

Once we have computed (6.7) we can compute the numerical flux $\bar{f}_{j+\frac{1}{2}}$ in (5.1b).

An exact $f^R(u_1,u_2)$, i.e.

$$\text{(6.8)}\qquad f^R(u_1,u_2)=f(V(0;u_1,u_2))$$

where $V(x/t;u_1,u_2)$ is the exact solution of the Riemann problem for the Euler equations of gas dynamics can be computed through an iterative algorithm. This algorithm is rather complicated, and we refer the reader to [5], [3] and [28] for its details.

To compute $f^R \equiv f^{ROE}$ in (5.11b) and (5.9b) all we need is to describe the particular average $\hat{u}(u_1, u_2)$ for the Euler equations of gas dynamics (see [25], [9]). To do so we denote the arithmetic mean of $b(u)$ with respect to u_1 and u_2 by

$$\langle b \rangle = \frac{1}{2}[b(u_1) + b(u_2)] \tag{6.9a}$$

and define

$$\hat{q} = \langle \sqrt{\rho} q \rangle / \langle \sqrt{\rho} \rangle, \ \hat{H} = \langle \sqrt{\rho} H \rangle / \langle \sqrt{\rho} \rangle, \ \hat{c} = (\gamma - 1)^{\frac{1}{2}} \cdot \sqrt{\hat{H} - \frac{1}{2}\hat{q}^2}; \tag{6.9b}$$

here H is the enthalpy (6.2c). Having prescribed $\hat{q}$, $\hat{H}$ and $\hat{c}$, we have all the quantities needed to define the eigenvalues and eigenvectors in (6.2).

REMARK (6.1): The importance of using the particular average (6.9) rather than a simpler one is that when (u_1, u_2) corresponds to a single shock or a single contact discontinuity in the solution of the Riemann problem $V(x/t; u_1, u_2)$, then f^{ROE} is exact, i.e.

$$f^{ROE}(u_1, u_2) = f^R(V(0; u_1, u_2)). \tag{6.10}$$

7. Numerical experiments. In this section we present results of several computer experiments with the schemes (4.14), (5.9). These schemes will be referred to as r-th order ENO schemes (or "r-th order" when applicable – see Remark (1.2)); ENO stands for Essentially Non-Oscillatory.

The ENO schemes are highly nonlinear and consequently do not easily lend themselves to rigorous analysis. At present we have completed the analysis of the non-oscillatory interpolation H_m (3.1) - (3.5) and have acquired a fairly good understanding of the reconstruction $R(x;\bar{w})$; these reconstruction results can be extended to a single application of the "abstract scheme" (1.10) to piecewise smooth data. Unfortunately we have not been able as yet to analyse rigorously the crucial question of accumulation of error. Under these circumstances, computer experiments have become our main tool of analysis. We have performed a large number of numerical experiments with initial data ranging from random noise to smooth functions. We have studied two notions of "stability": (i) Boundedness of a refinement sequence $h \to 0$, $\tau = O(h)$ for $0 \le t \le T$. (ii) Boundedness of the numerical solution as $n \to \infty$ with fixed h and τ. In all our experiments[4] we have found the ENO schemes to be stable under a CFL restriction of 1 and strongly so, in the sense that they strongly damp high frequency noise – this is probably due to the cell-averaging step (1.14c).

In [15], the first paper in this series, we have presented numerical results which compare the second order ENO scheme based on RD with $r = 2$ to a "second order accurate" MUSCL-type scheme, which is computationally equivalent to the "second order" ENO scheme based on RP with $r = 2$.

[4]The only exception where we had to reduce the CFL number is for the initial data of the mesh oscillation function $v_j^0 = (-1)^j$. This choice of initial data forces the ENO scheme to become linear; for $v_j^0 = \theta_j(-1)^j$, where θ_j is a positive random number, the scheme is again stable under a CFL restriction of 1: (see [16] for more details).

In [16], the second paper in this series, we have presented numerical experiments that verify our statements about the accuracy and non-oscillatory nature of the reconstruction $R(x;\bar{w})$, and demonstrate the stability of the ENO schemes in the scalar constant coefficient case for both the pure IVP and the mixed initial-boundary value problem (IBVP).

In this paper we present a sample of our numerical experiments for the non-linear scalar case and the Euler equations of gas dynamics in 1D. The purpose of this presentation is to address the open questions that we could not fully answer by analysis: The accumulation of error, the adequacy of the "solution in the small" procedure, consistency with entropy inequalities and the effectiveness of the characteristic-wise reconstruction for systems. We have performed most of the numerical experiments for $r = 1,2,3,4,5,6$. Since it is not practical to present six sets of data for each problem we usually compare $r = 2$, which is the current state of the art scheme, to $r = 4$ which seems to be optimal for smooth solutions. However presentation of a comprehensive efficiency study is deferred to a future paper.

A. Scalar conservation laws.

A1. Convex $f(u)$ with smooth initial data: In this sub-section we show results of applying the ENO schemes to

$$u_t + (u^2/2)x = 0 \tag{7.1a}$$

$$u(x,0) = \alpha + \beta \sin(\pi x + \gamma), \tag{7.1b}$$

for $-1 \le x \le 1, \quad t \ge 0$. In these calculations we have used the ENO schemes with f^R replaced by f^{ROE} (4.21) (without any entropy correction).

Let $Z(x,t)$ denote the solution of (7.1a) with $Z(x,0) = \sin \pi x$, i.e. $\beta = 1$, $\alpha = \gamma = 0$ in (7.1b). The solution $Z(x,t)$ is smooth for $0 \le t < 1/\pi$; when $t = 1/\pi$ a shock develops at $x = \pm 1$, and stays there as a stationary shock for $t > 1/\pi$. Some

time after its development, this shock starts interacting with the expansion wave in $-1 < x < 1$; this brings about a fast decay of the solution. The "exact" solution presented in the following is computed in $0 \leq x < 1$ by using Newton-Raphson iterations to solve the characteristic relation

$$Z = \sin \pi(x - Zt); \tag{7.2}$$

Z in (-1,0) is obtained from Z in (0,1) by $Z(-x,t) = -Z(x,t)$. The general solution of (7.1) is computed from $Z(x,t)$ in (-1,1) by

$$u(x,t) = \alpha + \beta Z(x - \alpha t + \gamma,\ \beta t). \tag{7.3}$$

In Tables 1 and 2 and figure 1 we present computation of (7.1) with $\alpha = 1$, $\beta = 1/2$, $\gamma = 0$, i.e. $u(x,t) = 1 + \frac{1}{2}Z(x - t, \frac{1}{2}t)$; thus the shock develops at $t = 2/\pi$. The results are presented at $t = 0.3$ when the solution is still smooth. We divide (-1,1) into J equal intervals and define

$$x_j = -1 + (j - 1/2)h, \quad h = 2/J, \quad 1 \leq j \leq J \tag{7.4}$$

First we consider the pure IVP for (7.1), i.e. periodic boundary conditions at $x = \pm 1$. In Figures 1a and 1b we show the results of the ENO schemes with RD at $t = 0.3$; figure 1a shows the second order ENO scheme, while figure 1b shows the fourth order one. Both calculations were performed with $J = 10$ and CFL = 0.6. The continuous line in these figures is the exact solution; the circles represent the values of $R(x_j; v^N)$. In Tables 1a and 1b we list the L_∞-error and the L_1-error at $t = 0.3$ of a refinement sequence $J = 8$, 16, 32, 64, 128 for $r = 1$, 2, 3, 4, 5 with CFL = 0.6. Table 1a shows the results of the ENO schemes with RP while Table 1b shows the ones with RD. The value of r_c in Tables 1 and 2 is the "computational order of accuracy" which is calculated by assuming the error to be a constant times h^{r_c}; this definition is meaningful only for h sufficiently small.

In figures 2a and 2b we use the same schemes as in figure 1, but with $J = 16$, and show the results at $t \approx 2/\pi$ (after 17 time-steps) which is the time of the formation of the shock. In figures 3a and 3b we show the reconstruction $R(x; v^n)$ corresponding to the numerical solutions of figure 2. The squares in figures 3a and 3b mark the values of $R(x_{j+\frac{1}{2}} \pm 0; v^n)$. $R(x; v^n)$ is piecewise-linear in figure 3a and piecewise - cubic in figure 3b.

Next we consider the IBVP for (7.1); since the characteristic speed for (7.3) with $\alpha = 1$, $\beta = \frac{1}{2}$, $\gamma = 0$ is positive, we prescribe

$$u(-1, t) = g(t); \tag{7.5a}$$

$x = +1$ is an outflow boundary and no condition is prescribed there. To be able to compare with the periodic problem we take $g(t)$ in (7.5a) to be the value of the periodic solution at $x = -1$, i.e.

$$g(t) = 1 + \frac{1}{2} Z(-1 - t, \frac{1}{2} t). \tag{7.5b}$$

The point of view that we have taken in treating boundary conditions is consistent with the presentation of the "abstract scheme" (1.10), (1.14) as a sequence of global operations. Thus in the reconstruction step, as in the pure IVP case, we use the given cell-averages $\{v_j^n\}$, $1 \le j \le J$, to get $R(x; v^n)$ for $-1 < x < 1$; in presence of boundaries we restrict the choice of stencil to available information by imposing the condition

$$1 \le i_k(j) \le J - r \quad \text{for } 1 \le k \le r \tag{7.6}$$

in the algorithm (3.4). Note that we do not use the given boundary data $g(t)$ (7.5a) in the reconstruction step. The boundary data is incorporated into the scheme on the PDE level by considering the solution-in-the-small step to be an IBVP. Obviously the resulting scheme is biased "against the wind" near $x = -1$;

nevertheless, numerical experiments in the nonlinear case as well as in the constant coefficient case (see [16]), indicate that the ENO schemes are stable. We observe that a similar choice of stencil occurs near discontinuities in the interior of the computational grid.

In Tables 2a and 2b we repeat the calculations in Table 1 for the IBVP (7.1) with (7.5). In figures 4a and 4b we show the calculations of the ENO schemes based on RP with $r = 2$ and $r = 4$, respectively, for the IBVP (7.1) with $\alpha = 0$, $\beta = 1$, $\gamma = \pi$. Here the boundaries $x = \pm 1$ are characteristic, and a stationary shock develops at $x = 0$ at $t = 1/\pi$. In these calculations we have treated $x = -1$ as an inflow boundary and specified

$$u(-1, t) = 0;$$

$x = +1$ was treated as an outflow boundary. The results show the numerical solution with $J = 16$ and CFL $= 0.6$ at $t = 0.6$, at which time the solution has already started to decay considerably due to the interaction of the shock with the expansion waves.

(A2). *Riemann IVP for non-convex $f(u)$*: In this subsection we show results of applying the ENO schemes to the Riemann IVP

(7.7a) $$u_t = f(u)_x = 0,\ u(x,0) = \begin{cases} u_L & x < 0 \\ u_R & x > 0 \end{cases}$$

where $f(u)$ is the non-convex function

(7.7b) $$f(u) = \frac{1}{4}(u^2 - 1)(u^2 - 4).$$

We recall that the main difficulty in justifying the approximation (4.13) is when the "fan" in (4.4) covers $x = x_{j+\frac{1}{2}}$; the same difficulty is encountered in justifying the use of f^{ROE} (4.21) instead of the exact flux of the Riemann problem (4.6). Therefore we present two cases in which $\bar{a}(u_L, u_R) = 0$; in the first case $x = 0$

is covered by a centered sonic rarefaction fan, while in the second one there is a stationary (sonic) shock at $x = 0$.

In each case we present two sets of experiments. In the first set we use the ENO schemes with the exact f^R which is defined by (4.6a); these results, which we consider to be rather pleasing, are presented in Figures 5 and 7. In the second set of experiments we use the ENO schemes with f^R replaced by the following modification of f^{ROE} in (4.21)

$$f^{ROE}(u_1, u_2) = \frac{1}{2}[f(u_1) + f(u_2) - \max(|\bar{a}(u_1, u_2)|, \varepsilon)(u_2 - u_1)]. \tag{7.8a}$$

The addition of the linear viscosity term $-\varepsilon(u_2 - u_1)/2$ for $|\bar{a}| < \varepsilon$, is the simplest but crudest entropy correction of (4.21). We note that $\varepsilon = 0$ in (7.8a) corresponds to (4.21), while $\varepsilon = 1/\lambda$ ($\lambda = \tau/h$) corresponds to Lax's first order scheme [18]; since (7.8a) satisfies relation (4.16c) the modified scheme remains r-th order accurate. In our calculations we take

$$\varepsilon = 0.1/\lambda. \tag{7.8b}$$

Analysis presented in [24] shows that using (7.8a) - (7.8b) in the "second-order" TVD scheme of [9] results in a scheme which converges to entropy correct solutions for convex $f(u)$, provided that λ is sufficiently small; numerical experiments in the convex case [9] and the non-convex case [32] seem to verify this statement even for CFL number close to 1.

The numerical results of the ENO schemes using (7.8a) - (7.8b) are shown in Figures 6 and 8. These results show that the ENO schemes converge to entropy correct solutions; however, the quality of the numerical approximation depends strongly on the formal order of accuracy of the scheme.

We remark that an entropy correction to f^{ROE} which is more appropriate for the non-convex case is obtained by using in (7.8a) $\varepsilon = \varepsilon(u_1, u_2)$ which is defined by

$$\varepsilon = \max[0,\ \bar{a}(u_1, u_2) - a_L,\ a_R - \bar{a}(u_1, u_2)] \tag{7.8c}$$

where

$$a_L = \min_{v \in [u_1, u_2]} \bar{a}(u_1, v), \quad a_R = \max_{v \in [u_1, u_2]} \bar{a}(v, u_2); \tag{7.8d}$$

see [13]. In this case the modified f^{ROE} becomes computationally equivalent to the exact f^R.

Our purpose in presenting numerical experiments with the crude entropy correction (7.8b) rather than the more appropriate one (7.8c) - (7.8d) is to demonstrate that the importance of the Riemann solver in the formulation of the ENO schemes is decreasing with increasing order of accuracy. When $r = 1$ $R(x; v^n)$ is piecewise-constant and all the variation of the solution is contained in the discontinuities of the reconstruction. Consequently the Riemann solver is the only mechanism to describe time evolution. For $r > 1$, the smooth polynomial variation in the cell (which is $O(h)$ in regions of smoothness) is generally larger than the variation in the discontinuities of the reconstruction (which is $O(h^r)$ in regions of smoothness) – see Figures 3, 14 and 16. Therefore the time evolution of the smooth polynomial part, namely the Cauchy-Kowalewski procedure, is in general more important than the Riemann solver. The only exception is in the first few time-steps needed to introduce intermediate states in the solution to the Riemann IVP (7.7) where (u_L, u_R) is not a shock.

In all the calculations presented in this subsection we have used the ENO schemes with RD and CFL = 0.8.

Case: (i): $u_L = 2,\ u_R = -2.$

The exact solution in this case is (see figure 5a)

$$u(x,t) = \begin{cases} 2 & x/t < -0.5281529 \\ g(x/t) & |x|/t < 0.5281529; \\ -2 & x/t > 0.5281529 \end{cases} \tag{7.9a}$$

here $g(x/t)$ is a centered rarefaction wave: $g(y)$ is the solution of

$$y = f'(g)$$

in the concave part of f which is $|u| < \sqrt{5/6}$;

$$g(\pm 0.5281529) = \mp 0.2152504.$$

In figures 5b, c, d we show the results of the ENO schemes using the exact f^R as defined by (4.6a) for $r = 1, 2, 4$, respectively; in these calculations we used J = 40 in (7.4) and N = 80 time-steps. The exact solution is shown by the continuous line; the circles mark the values of $R(x_j; v^N)$. We observe that the structure of the solution in these calculations has developed at the correct rate; this is evident from the fact that the location of the computed shocks is accurate. In figure 5b we notice the "dog-leg" which is typical of Godunov's scheme.

In Figures 6a, b, c we repeat the calculations in Figures 5b, c, d but with f^R replaced by f^{ROE} (7.8a) - (7.8b). From these figures we see that the scheme develops the correct structure of the solution, but not at the correct rate. This is due to the fact that $\epsilon = 0.1/\lambda$ represents a fan which is much narrower than the initial fan in the exact solution. The location of the computed shocks lags behind the correct location by 8 cells for $r = 1$, 3 cells for $r = 2$ and only one cell for $r = 4$. To verify that the numerical approximations converge to the entropy correct solution we refine the mesh by a factor of 2 and repeat the calculations of Figures 6a, b, c with J = 80, N = 160; the results of these calculations are shown in Figures

6d, e, f. Since the number of cells by which the computed shocks lags behind the correct location remains the same, we conclude that the numerical approximations indeed do converge to the entropy correct solution.

Taking into account the crudeness of the entropy correction (7.8b) we consider the performance of the 4-th order scheme in figures 6c and 6f to be surprisingly good.

Case (ii): $u_L = -3,\ u_R = 3.$

The exact solution in this case is (see figure 7a)

$$u(x,t) = \begin{cases} -3 & x/t \le -19.5 \\ \tilde{g}(x/t) & -19.5 \le x/t < 0; \\ -\tilde{g}(-x/t) & 0 < x/t \le 19.5 \\ 3 & 19.5 \le x/t \end{cases} \tag{7.9b}$$

here $\tilde{g}(y)$ is the solution of

$$y = f'(\tilde{g})$$

in the convex part of f which is $|u| > \sqrt{5/6}$. Note that the solution (7.9b) is discontinuous at $x = 0; \tilde{g}(0) = \sqrt{2.5}$.

In Figures 7b, c, d we show the results of the ENO schemes using the exact f^R as defined by (4.6a) for $r = 1, 2, 4$, respectively; in these calculations we used J = 40 in (4.4) and N = 20 time-steps. We observe that the stationary shock at $x = 0$ in these figures is perfectly resolved.

In figures 8a, b, c we repeat the calculations in Figures 7b, c, d but with f^R replaced by f^{ROE} (7.8a) - (7.8b). Since the rarefaction fans in this case are not sonic, the quality of the numerical approximation of the rarefaction wave in figures 8a, b, c is similar to that of the corresponding one in figures 7b, c, d. We observe that the stationary shock at $x = 0$ in figures 8a, b, c is somewhat smeared - this is due to the fact that the Riemann solver corresponding to (7.8b) places a fan of the size $|x/t| < \epsilon$ around $x = 0$. Nevertheless, if we compare the results of the 4-th

order ENO schemes in the two experiments, we find that the results in figure 8c are only slightly inferior to those of figure 7d.

B. Euler equations of gas dynamics. In this subsection we present numerical experiments with the ENO schemes for the Euler equations of gas dynamics for a polytropic gas with $\gamma = 1.4$ (see section 6). In all these calculations we have used reconstruction via primitive function (RP) and f^{ROE} (5.11), (6.9) without any entropy corrections.

(B1). *Riemann problems.* In figures 9 and 10 we show the results of applying the ENO schemes with $r = 2$ and $r = 4$, respectively, to the Riemann problem (7.7a) with the initial data

$$(\rho_L, q_L, P_L) = (1, 0, 1); \quad (\rho_R, q_R, P_R) = (0.125, 0, 0.10). \tag{7.10a}$$

In these calculations we have used the characteristic reconstruction (5.8), (6.3) with 100 cells, $h = 0.1$, CFL $= 0.8$ and 50 time steps.

In figure 11 we repeat the calculation of the "4-th order" ENO scheme in figure 10 but with component-wise reconstruction (5.1). Comparing figure 10 with figure 11 we see that there is some "noise" in the component-wise reconstruction which is eliminated by using characteristic reconstruction. We note however that the level of "noise" in figure 11 may be considered acceptable for practical calculations.

The initial data (7.10a) are those of the Riemann problem proposed by Sod in [23], which has become a standard test problem. The solution to this problem has a monotone decreasing density profile and therefore it does not display certain difficulties that may arise when the intermediate state has to be "built-up." In figures 12-16 we present calculations for the Riemann problem

$$(\rho_L, q_L, P_L) = (0.445,\ 0.698,\ 3.528); (\rho_R, q_R, P_R) = (0.5,\ 0,\ 0.571) \tag{7.10b}$$

used by Lax in [18]; see also [7], [9]. All these calculations were performed with 100 cells, $h = 0.1$, CFL $= 0.8$ and 85 time-steps using a component-wise reconstruction (5.11). In figure 12 we show the results of the "4-th order" ENO scheme using a component-wise reconstruction (5.11). Comparing these results to figure 11 we see that the component-wise reconstruction here is much "noisier" than in Sod's problem. In figures 13 and 15 we show the results of the ENO schemes using characteristic reconstruction (6.3) for $r = 2$ and $r = 4$, respectively; comparing figure 15 to figure 12 we see that most of the "noise" in figure 12 is eliminated.

In figures 14 and 16 we show the characteristic reconstruction $R(x; v^n)$ of the numerical solution in figures 13 and 15, respectively; $R(x; v^n)$ is piecewise-linear in figure 14 ($r = 2$) and piecewise-cubic in figure 16 ($r = 4$). The squares in these figures mark the values of $R(x_{j+\frac{1}{2}} \pm 0; v^n)$; thus the difference between the two squares at the same location shows the size of the discontinuity in the reconstruction there (we recall that the circles in figures 13 and 15 are the values of $R(x_j; v^n)$). We see that the discontinuities in the reconstruction of the rarefaction wave are small enough to be graphically imperceptible. Surprisingly the discontinuities in the reconstruction of the contact-discontinuity are also rather small. Comparing figure 16 to figure 14 we notice that the size of the discontinuities in the reconstruction for $r = 4$ is always considerably smaller than that for $r = 2$. It is interesting to note that even in the shock region in figure 16 ($r = 4$), the sum of the jumps in the reconstruction is only about 35% of the size of the shock, while about 65% of the shock jump is described by the smooth polynomial part of the reconstruction.

We remark that because of the self-similar nature of the solution to the Riemann problem, the rate of convergence of any scheme is inherently limited to first order (see [27]). Comparing $r = 4$ with $r = 2$ in the solution of the above Riemann problems we notice a slight improvement in the smearing of the contact discontinuity (we have not used artificial compression in these calculations) and the description

of the rarefaction wave. Because of the self-similar nature of the solution it is better to compare the performances of two schemes by using x/t as the spacial variable and to find how many time-steps it takes to get well resolved intermediate states. Doing so for the problem (7.10b) we find that $r = 4$ with $N = 35$ gives about the same result as $r = 2$ with $N = 70$.

(B2). *Interaction of blast waves:* In this subsection we present numerical experiments with the ENO schemes for the problem of two interacting blast waves:

$$u(x,0) = \begin{cases} u_L & 0 \le x < 0.1 \\ u_M & 0.1 \le x < 0.9 \\ u_R & 0.9 \le x < 1 \end{cases} \tag{7.11a}$$

where

(7.11b)

$$\rho_L = \rho_M = \rho_R = 1, \quad q_L = q_M = q_R = 0, \quad P_L = 10^3,\ P_M = 10^{-2},\ P_R = 10^2;$$

the boundaries at $x = 0$ and $x = 1$ are solid walls. This problem was suggested by Woodward and Colella as a test problem; we refer the reader to [31] where a comprehensive comparison of the performance of various schemes for this problem is presented.

In our calculations we divided the interval (0,1) into J cells by

$$x_j = (j - \frac{1}{2})/J \qquad j = 1, ..., J, \tag{7.12a}$$

where x_j marks the center of the j-th cell. The boundary conditions of a solid wall in $x = 0$ and $x = 1$ were treated by reflection, i.e. we defined auxiliary states $v^n_0, ..., v^n_{-r+1}$ for the left wall and $v^n_{J+1}, ..., v^n_{J+r}$ for the right wall by

$$\rho^n_{-j+1} = \rho^n_j, \qquad q^n_{-j+1} = -q^n_j, \qquad P^n_{-j+1} = P^n_j, \qquad j = 1, ..., r \tag{7.12b}$$

$$\rho^n_{J+j} = \rho^n_{J-j+1}, \quad q^n_{J+j} = -q^n_{J-j+1}, \quad P^n_{J+j} = P^n_{J-j+1}, \quad j = 1, ..., r. \tag{7.12c}$$

We observe that representing the solid wall condition by the above reflection is very suitable for the characteristic reconstruction: \ 3-wave approaching the right boundary is reflected as a 1-wave; consequently there is hardly any interaction between the waves in the characteristic variables (6.3a) and a situation of not having enough points of smoothness to choose from is thus avoided.

In figures 17a-17h we show the solution of the "4-th order" ENO scheme at $t = 0.010$, 0.016, 0.026, 0.028, 0.030, 0.032, 0.034, 0.038, respectively. We refer the reader to figure 2 in [31] where a highly accurate solution is displayed and a detailed description of the various interactions that occur at these instances is presented. The continuous line in figures 17a-17h, 18 and 19 is the solution of the "4-th order" ENO scheme with $J = 800$ in (7.12a). Comparing this solution to the "exact" solution of Woodward and Colella in [31], we find that it shows all the important features of the various interactions and thus can be considered a "converged" solution. (The continuous line representing the solution with $J = 800$ is the piecewise-linear interpolation of $\{R(x_j; v^n)\}$; consequently cusps in the solution, which do appear in $R(x; v^n)$, are chopped in the graphic representation). The circles in figures 17a-17h show the values of $R(x_j; v^n)$ of the "4-th order" ENO scheme with $J = 400$. Comparing the numerical solution for $J = 400$ to that of $J = 800$ we see that the velocity and pressure have already converged, while the density in figures 17g and 17h still deviates from the "converged" solution. This is due to the smearing of 3 contact discontinuities which are present in the solution at this time; the numerical results of Woodward and Colella demonstrate that the addition of "contact-discontinuity steepeners" improve the density profile considerably.

In figure 18 we show the solution of the "4-th order" ENO scheme with $J = 200$ at the final time $t = 0.038$; In figure 19 we repeat the calculation in figure 18 for the "second-order" ENO scheme. Comparing figure 18 and figure 19 we see that the "4-th order" scheme gives a much better resolution. We remark that the results

of the "4-th order" scheme with $J = 100$ (not shown here) are of the same quality as those of the "second-order" scheme with $J = 200$.

We note that a parabola interpolating

$$P(x_{-1}) = 240, \quad P(x_0) = 0.01, \quad P(x_1) = 40$$

has an interval in which it is negative; the same is true for higher order interpolating polynomials that pass through these points. A situation of this type occurs in the calculation of the two interacting blast waves just before the interaction in figure 17d, when the low pressure region in figure 17c is shrinking to 1-2 computational cells. Since high order interpolating polynomials may produce negative values of pressure and density in such drastic situations, we have imposed a "positivity condition" on the reconstruction step of our programs for the Euler equations. To ensure that $\mathbf{R}(x; v^n)$ in the j-th cell yields density and pressure that are positive, i.e.

(7.13a)

$$P_j + \sum_{k=1}^{r-1} \left.\frac{\partial^k P}{\partial x^k}\right|_{x=x_j} \frac{(x-x_j)^k}{k!} > 0, \quad \rho_j + \sum_{k=1}^{r-1} \left.\frac{\partial^k \rho}{\partial x^k}\right|_{x=x_j} \frac{(x-x_j)^k}{k!} > 0 \text{ for } |x-x_j| < h/2$$

we check whether

$$\text{(7.13b)} \qquad \sum_{k=1}^{r-1} \left|\frac{\partial^k P_j}{\partial x^k}\right| \frac{(h/2)^k}{k!} < 0.8 P_j; \sum_{k=1}^{r-1} \left|\frac{\partial^k \rho_j}{\partial x^k}\right| \frac{(h/2)^k}{k!} < 0.8 \rho_j.$$

If condition (7.13b) is not satisfied we reduce the order of the reconstruction *locally* at $x = x_j$ until positivity is ensured. We observe that the LHS of the inequalities in (7.13b) is $O(h)$ in smooth regions, hence this positivity condition does not reduce the asymptotic order of accuracy. Our computer program monitors occurances of order reduction due to the positivity condition; we have found that the order in the calculations of the "4-th order" ENO scheme has been reduced during two time steps before the interaction in figure 16d, and only at the interaction zone itself; we have not encountered any order reduction in the solution to the Riemann problems (7.10).

C. Variants and extensions.

C1. *Characteristic method for the scalar case:* In [15] we described an approximation to $v(x,t)$, the solution-in-the-small of (4.2), which is obtained by tracing approximate characteristics to the initial data. This approximation $\tilde{v}(x,t)$ can be extended to arbitrary order of accuracy as follows: Let $\tilde{a}^n_{j+\frac{1}{2}}$ denote

$$\tilde{a}^n_{j+\frac{1}{2}} = \bar{a}(R(x_{j+\frac{1}{2}} - 0; v^n),\ R(x_{j+\frac{1}{2}} + 0; v^n)) \tag{7.14a}$$

where $\bar{a}(u_1, u_2)$ is defined in (4.7), and let $\tilde{a}(x)$ denote the interpolation of $\tilde{a}^n_{j+\frac{1}{2}}$ by H_m (3.1) with $m = r-1$, i.e.

$$\tilde{a}(x_{j+\frac{1}{2}}) = \tilde{a}^n_{j+\frac{1}{2}} \tag{7.14b}$$

$$\tilde{a}(x) = H_m(x; \tilde{a}^n), \quad m = r-1. \tag{7.14c}$$

The approximation $\tilde{v}(x,t)$ is obtained by prescribing constancy of the solution along the approximate characteristic lines

$$x = x_0 + \tilde{a}(x_0)t \tag{7.15a}$$

i.e.

$$\tilde{v}(x_0 + \tilde{a}(x_0)t, t) = \tilde{v}(x_0, 0) = R(x_0; v^n); \tag{7.15b}$$

thus

$$\tilde{v}(x,t) = R(x_0(x,t); v^n) \tag{7.15c}$$

where $x_0(x,t)$ is the solution of the algebraic equation (7.15a). Let $x_0^1(x,t)$ denote the solution to (7.15a) for $m = 1$ in (7.14c); if x and t are such that

$$\tilde{x}_{j-\frac{1}{2}}(t) < x \leq \tilde{x}_{j+\frac{1}{2}}(t) \tag{7.16a}$$

where

(7.16b) $$\tilde{x}_{i+\frac{1}{2}}(t) = x_{i+\frac{1}{2}} + t\ \tilde{a}^n_{i+\frac{1}{2}}$$

then

(7.16c) $$x^1_0(x,t) = x_{j-\frac{1}{2}} + \frac{x_{j+\frac{1}{2}} - x_{j-\frac{1}{2}}}{\tilde{x}_{j+\frac{1}{2}}(t) - \tilde{x}_{j-\frac{1}{2}}(t)}\ (x - \tilde{x}_{j-\frac{1}{2}}(t)).$$

For $m > 1$ we obtain $x_0(x,t)$ by solving (7.15a) with Newton-Raphson iterations starting with the initial guess (7.16c).

Using $\tilde{v}(x,t)$ (7.15c) we define the following variant of (4.14):

(7.17a) $$v^{n+1}_j = v^n_j - \lambda(\bar{f}_{j+\frac{1}{2}} - \bar{f}_{j-\frac{1}{2}})$$

(7.17b) $$\bar{f}_{j+\frac{1}{2}} = \sum_{k=0}^{k} \alpha_k\ f(\tilde{v}(x_{j+\frac{1}{2}}, \beta_k \tau)).$$

We have started the development of the ENO schemes with the version (7.17); later on we have replaced the characteristic method by the Cauchy-Kowalewski procedure which offers a unified approach in extending the scheme to include forcing terms and to systems of conservation laws. Our numerical experiments show that the two versions are computationally equivalent, although the version with the characteristic method (7.17) seems to be slightly more accurate than (4.14).

We remark that the scheme (7.17), as the scheme (4.14) with f^{ROE} in (4.21a), also admits any discontinuity with $\bar{a}(u_L, u_R) = 0$ as a stationary solution. This can be easily rectified by replacing the "shock curve" $\tilde{x}_{i+\frac{1}{2}}(t)$ in (7.16b) by an appropriate fan.

C2. *Semi-discrete formulation and Runge-Kutta methods:* The semi-discrete version of the ENO schemes can be derived either directly from (1.4) or by letting $\tau \to 0$ in (4.14), (5.9). It takes the form

(7.18a) $$\frac{d}{dt}\ v_j(t) = -\frac{1}{h}[\bar{f}_{j+\frac{1}{2}}(t) - \bar{f}_{j-\frac{1}{2}}(t)] \equiv Q\ v_j(t)$$

where

(7.18b) $$\bar{f}_{j+\frac{1}{2}}(t) = f^R(R(x_{j+\frac{1}{2}} - 0; v(t)),\ R(x_{j+\frac{1}{2}} + 0; v(t)));$$

here $v_j(t)$ is an approximation to $\bar{u}(x_j, t); v(t) = \{v_j(t)\}$; $f^R(u_1, u_2)$ is either the exact flux (4.5) or f^{ROE} (4.21), (5.11).

Considering (7.18) to be a system of ordinary differential equations in t for the vector $v(t) = \{v_j(t)\}$, we can solve the problem by using a numerical ODE solver. In [2] we present two sets of numerical experiments in which we use Runge-Kutta methods of appropriate order to approximate the solution of (7.18). In the first set of experiments we apply the scheme to the Riemann problem (7.10a) for $r = 1$, 2, 3, 4, 5, 6. In the second set of experiments we apply the scheme with $r = 2, 4$ to a Laval nozzle problem which involves the addition of a forcing term to the Euler equations (6.1). In these calculations we have used RP, f^{ROE} and CFL = 0.5. Comparing the results of the Riemann problem to those in the present paper we find them to be of similar quality. The numerical experiments of [2] indicate that the semi-discrete formulation (7.18) with Runge-Kutta temporal discretization does not generate spurious oscillations for CFL $\leq$ 0.5; however when we increase the CFL number beyond 0.5 we start getting some oscillations and eventually the scheme becomes unstable.

The main advantage of using the Runge-Kutta temporal discretization is the ease of its programming; however it seems to be less efficient than the fully discrete formulation and also requires more storage.

C3. *Variable grid and front tracking:* In section 3 we have pointed out that the non-oscillatory interpolation H_m (3.1) - (3.5) and the reconstruction via primitive function (RP) (3.6) - (3.10) are well defined for non-uniform grids, see appendix. Since the solution-in-the-small step also does not require uniformity of the grid, we

may compute new cell-averages v_j^{n+1} in (1.14c) on any choice of intervals $\{I_j^{n+1}\}$ by

$$v_j^{n+1} = \frac{1}{|I_j^{n+1}|}\int_{I_j^{n+1}} v_h(x, t_{n+1} - 0)dx; \tag{7.19}$$

here $I_k^\ell = (\xi_{k-\frac{1}{2}}^\ell, \xi_{k+\frac{1}{2}}^\ell)$ and $|I_k^\ell| = \xi_{k+\frac{1}{2}}^\ell - \xi_{k-\frac{1}{2}}^\ell$. Using the same rationale as before, our approximation to (7.19) becomes

$$|I_j^{n+1}|\, v_j^{n+1} = |I_j^n|\, v_j^n - \tau(\bar{f}^\sigma_{j+\frac{1}{2}} - \bar{f}^\sigma_{j-\frac{1}{2}}). \tag{7.20a}$$

The numerical flux $\bar{f}^\sigma_{j+\frac{1}{2}}$ is consistent with $f(u) - \sigma_{j+\frac{1}{2}}u$

$$\sigma_{j+\frac{1}{2}} = (\xi_{j+\frac{1}{2}}^{n+1} - \xi_{j+\frac{1}{2}}^n)/\tau, \tag{7.20b}$$

and can be expressed as

$$\bar{f}^\sigma_{j+\frac{1}{2}} = \sum_{k=0}^{k} \alpha_k \bar{f}^R(\tilde{v}_j(x_{j+\frac{1}{2}} + \beta_k\tau\sigma_{j+\frac{1}{2}}, \beta_k\tau), \tilde{v}_{j+1}(x_{j+\frac{1}{2}} + \beta_k\tau\sigma_{j+\frac{1}{2}}, \beta_k\tau); \sigma_{j+\frac{1}{2}}) \tag{7.20c}$$

where

$$\bar{f}^R(u_1, u_2; \sigma) = f(V(\sigma; u_1, u_2)) - \sigma V(\sigma; u_1, u_2); \tag{7.20d}$$

we recall that $V(\sigma; u_L, u_R)$ denotes the value of the solution to the Riemann problem (4.3) at $x/t = \sigma$. Roe's linearization (5.11) yields the following approximation

$$\begin{aligned}\bar{f}^{ROE}(u_1, u_2; \sigma) = \frac{1}{2}[f(u_1) + f(u_2) - \sigma(u_1 + u_2) \\ - \sum_{k=1}^{m} \delta_k(u_1, u_2)|a_k(\hat{u}) - \sigma|r_k(\hat{u})].\end{aligned} \tag{7.21}$$

In figure 20 we show the results of the scheme (7.20) with $\bar{f}^R$ approximated by $\bar{f}^{ROE}$ (7.21) for the Riemann problem (7.10b); the values of $\{\xi_j^{n+1}\}$ in this calculation were chosen by the self-adjusting grid algorithm of [13]. This algorithm provides an automatic way to place interval end-points ξ_j^{n+1} at the location of

significant discontinuities and thus avoid their smearing by the cell-averaging step (7.19). The calculation in figure 20 was initialized by taking the exact solution of the Riemann problem at $t = 0.5$ (at which time there are 4 grid points between the contact-discontinuity and the shock). The results displayed in figure 20 show the numerical solution of the scheme with $r = 4$ after 100 time steps with CFL $= 0.5$. These results clearly demonstrate the adaptability of the ENO schemes to front tracking techniques.

We note that the use of irregular grids disallows the extra order of accuracy which was gained in (1.18) for a uniform grid. Numerical experiments with irregular grids (where ξ_j^{n+1} is randomly selected within a specified interval) show that the error in solving the scalar smooth problem (7.1) by the scheme (7.20) is $O(h^{r-1})$ in the L_1, L_2 and L_∞ norms. However comparing figure 20 with figure 15 we observe a considerable gain in resolution in spite of the reduction in formal order of accuracy.

C4. *Extension to* 2D: In this subsection we outline the extension of the ENO schemes to the solution of the two-dimensional IVP

$$u_t + f(u)_x + g(u)_y = 0, \qquad u(x,y,0) = u_0(x,y). \tag{7.22}$$

We note that Strang-type dimensional splitting [29] is only second-order accurate in time, and therefore is unsuitable for extending the higher order accurate members of the ENO schemes to 2D.

Let $\bar{\bar{w}}$ denote the two-dimensional "sliding average" of w

$$\bar{\bar{w}}(x,y) = \frac{1}{\Delta x \Delta y} \int_{-\Delta x/2}^{\Delta x/2} \int_{-\Delta y/2}^{\Delta y/2} w(x+\xi, y+\eta) d\eta d\xi. \tag{7.23}$$

Integrating (7.22) over the computational cell $I_{ij} \times [t_n, t_{n+1}]$, $I_{ij} = [x_{i-\frac{1}{2}}, x_{i+\frac{1}{2}}] \times [y_{j-\frac{1}{2}}, y_{j+\frac{1}{2}}]$, we find that $\bar{\bar{u}}_{ij}^n = \bar{\bar{u}}(x_i, y_j, t_n)$ satisfies the equation

$$\bar{\bar{u}}_{ij}^{n+1} = \bar{\bar{u}}_{ij}^n - \lambda_x(\hat{f}_{i+\frac{1}{2},j} - \hat{f}_{i-\frac{1}{2},j}) - \lambda_y(\hat{g}_{i,j+\frac{1}{2}} - \hat{g}_{i,j-\frac{1}{2}}) \tag{7.24a}$$

where $\lambda_x = \tau/\Delta x,\ \lambda_y = \tau/\Delta y$ and

$$\hat{f}_{i+\frac{1}{2},j} = \frac{1}{\tau\Delta y}\int_0^\tau \int_{-\Delta y/2}^{\Delta y/2} f(u(x_{i+\frac{1}{2}}, y_j+\eta, t_n+t))d\eta dt, \tag{7.24b}$$

$$\hat{g}_{i,j+\frac{1}{2}} = \frac{1}{\tau\Delta x}\int_0^\tau \int_{-\Delta x/2}^{\Delta x/2} g(u(x_i+\xi, y_{j+\frac{1}{2}}, t_n+t))d\xi dt. \tag{7.24c}$$

The abstract form of the ENO schemes for the solution of (7.22) remains (1.10), i.e.

$$v^{n+1} = A_h \cdot E(\tau) \cdot R(\cdot,\cdot; v^n), \quad v^0 = \bar{\bar{u}}_0. \tag{7.25}$$

As before $E(t)$ is the exact evolution operator of (7.22); however, A_h is now the 2-dimensional cell-averaging (7.23) and $R(x,y;\bar{\bar{w}})$ is an appropriate 2-dimensional reconstruction of $w(x,y)$. In the scalar constant coefficient case

$$u_t + au_x + bu_y = 0, \qquad u(x,y,0) = u_0(x,y), \tag{7.26a}$$

the ENO scheme (7.25) becomes

$$v_{ij}^{n+1} = \bar{\bar{R}}(x_i - a\tau, y_j - b\tau; v^n), \quad v_{ij}^0 = \bar{\bar{u}}_0(x_i, y_j). \tag{7.26b}$$

In [12] we present numerical experiments with the ENO scheme (7.26) for the scalar constant coefficient case, where the reconstruction $R(x,y;\bar{\bar{w}})$ is obtained via a two-dimensional deconvolution. Expanding $w(x+\xi, y+\eta)$ in (7.23) around $\xi = \eta = 0$ we get as in (3.12)

$$\begin{aligned}\bar{\bar{w}}(x,y) = w(x,y) + \alpha_2[(\Delta x)^2 w_{xx} + (\Delta y)^2 w_{yy}] + \alpha_4[(\Delta x)^4 w_{xxxx} + \\ + 2(\Delta x)^2(\Delta y)^2 w_{xxyy} + (\Delta y)^4 w_{yyyy}] + O(\Delta^6)\end{aligned} \tag{7.27}$$

Multiplying both sides of (7.27) by $(\Delta x)^k(\Delta y)^{l-k}\frac{\partial^l}{\partial x^k \partial y^{l-k}}$ and truncating the expansion in the RHS at $O(\Delta^r)$, we get as in (3.13) an invertable system of linear

equations which expresses $\bar{w}$ and its derviatives in terms of w and its derivatives. We set

(7.28a) $$(\bar{D}^{0,0})ij = \bar{w}(x_i, y_j)$$

and obtain approximations

(7.28b) $$(\bar{D}^{k,l})_{ij} = (\Delta x)^k(\Delta y)^l \frac{\partial^{k+l}}{\partial x^k \partial y^l}\bar{w}(x_i, y_j) + O(\Delta^r), \quad 1 \le k + l \le r - 1;$$

then, as in (3.17), we invert the system of linear equations to get the following approximations to w and its derivatives

(7.29a) $$(D^{k,l})_{ij} = (\Delta x)^k(\Delta y)^l \frac{\partial^{k+l}}{\partial x^k \partial y^l}\ w(x_i, y_j) + O(\Delta^r), \quad 0 \le k + l \le r - 1.$$

Using (7.29a) we define R in the cell I_{ij} by

(7.29b) $$R(x, y; \bar{w}) = \sum_{l=0}^{r-1} \frac{1}{l!} \sum_{k=0}^{l} (D^{k,l-k})_{ij} \binom{l}{k} \left(\frac{x - x_i}{\Delta x}\right)^k \left(\frac{y - y_j}{\Delta y}\right)^{l-k}, \ (x, y) \in I_{ij}.$$

The approximations $\bar{D}^{k,l}$ in (7.28b) are obtained by a sequence of applications of the one-dimensional operation (3.15b), which we rewrite now in the following operator form:

(7.30) $$(G_m^i \bullet u)_j = M\left(\frac{d^l}{dz^l} H_m(z_j - 0; u_j), \frac{d^l}{dz^l} H_m(z_j + 0; u)\right);$$

here u denotes the one-dimensional vector $\{u(z_j)\}_{j=1}^{J}$. Using (7.30) and the notation convention $\bar{w}_{\bullet,j} = \{\bar{w}(x_i, y_j)\}_{i=1}^{I}$, we define

(7.31a) $$(\bar{D}^{k,0})_{ij} = (\Delta x)^k (G_m^k \bullet \bar{w}_{\bullet,j})_i, \qquad 1 \le k \le r - 1,$$

(7.31b) $$(\bar{D}^{0,l})_{ij} = (\Delta y)^l (G_m^l \bullet \bar{w}_{i,\bullet})_j, \qquad 1 \le l \le r - 1.$$

To obtain approximations to the mixed derivatives of $\bar{w}$ we first evaluate

$$(\tilde{D}_1^{k,l})_{ij} = (\Delta y)^l [G_{m-k}^l \bullet (\bar{\bar{D}}^{k,0})_{i,\bullet}]_j, \qquad 1 \le l \le r-1-k,$$

$$(\tilde{D}_2^{k,l})_{ij} = (\Delta x)^k [G_{m-l}^k \bullet (\bar{\bar{D}}^{0,l})_{\bullet,j}]_i, \qquad 1 \le k \le r-1-l,$$

and then define

$$(\bar{\bar{D}}^{k,l})_{ij} = M((\tilde{D}_1^{kl})_{ij}, (\tilde{D}_2^{kl})_{ij}), \tag{7.31c}$$

where M is the min mod function (3.16).

We observe that the restriction of the two-dimensional reconstruction (7.29) to $y = y_j$, i.e. $R(x, y_j; \bar{w})$ is identical to the one-dimensional reconstruction (3.18) applied to the restriction of $\bar{w}$ to $y = y_j$, i.e. $R(x; \bar{w}(\bullet, y_j))$; the same observation applies to the restrictions to $x = x_i$.

We recall that the one-dimensional reconstruction is essentially non-oscillatory only if discontinuities are seperated by at least $r+1$ points of smoothness. In the one-dimensional system case we had to overcome the problem of collision (in time) of discontinuities; in the two-dimensional case we also have to worry about intersections (in space) of curves of discontinuity. In order to study the severity of the problem we have experimented with the constant coefficient problem (7.26a) with the initial data

$$u_0(x,y) = \begin{cases} 1 & (x,y) \in S; \\ 0 & (x,y) \in U - S \end{cases} \tag{7.32}$$

here $U = [-1,1] \times [-1,1]$ and S is a rotated square contained in U. In [12] we present numerical results which are obtained by applying the scheme (7.26) with $r = 1,2,3,4$ to the initial data (7.32) with periodic boundary conditions on ∂U. These results show that indeed small spurious oscillations are generated for $r \ge 2$ at the corners of S, however it seems to us that they are small enough to be computationally acceptable.

Appendix: An algorithm for reconstruction.

In this appendix we describe our algorithm for computing the coefficients $b_{j,k}$ in

$$R(x;\bar{w}) = \sum_{k=0}^{r-1} b_{j,k}(x - x_j)^k, \tag{A.1}$$

where x_j is the center of the j-th cell. To obtain these coefficients we start with Newton's form of interpolation

$$H_r(x;u) = \sum_{k=0}^{r} u[y_i, ..., y_{i+k}] \prod_{l=0}^{k-1} (x - y_{i+l}). \tag{A.2}$$

Here $i = i(j)$ is selected by the algorithm (3.4) with respect to the divided differences

$$d_{i,k} = u[y_i, ..., y_{i+k}] \tag{A.3}$$

In the following we describe an algorithm to rewrite the polynomial on the RHS of (A.2) as a finite Taylor series around $x = x_c$:

$$q(x) = \sum_{k=0}^{r} d_{i,k} P_{i,k}(x) = \sum_{k=0}^{r} q^{(k)}(x_c)(x - x_c)^k/k! \tag{A.4}$$

where

$$P_{i,k}(x) = \prod_{l=0}^{k-1} (x - y_{i+l}) \equiv \sum_{l=0}^{k} S_{l,k}(x - x_c)^{k-l}. \tag{A.5}$$

Using the fact that the coefficients $\{S_{l,k}\}$ satisfy a recursion relation we compute them as follows:

We set

$$Z_l = x_c - y_{i+l}, \quad 0 \le l \le r-1; \tag{A.6}$$

$$S_{0,k} = 1, \quad 0 \le k \le r;$$

then we evaluate

$$\text{(A.7)} \qquad \begin{cases} \text{do } l = 1, r \\ S_{l,l} = S_{l-1,l-1} Z_{l-1} \\ \text{do } k = l+1, r \\ S_{l,k} = S_{l,k-1} + S_{l-1,k-1} Z_{k-1} \end{cases}$$

It is easy to see that

$$\text{(A.8)} \qquad q^{(k)}(x_c) = k! \sum_{l=k}^{r} S_{l-k,l} d_{i,l}$$

We note that the algorithm (A.6) - (A.8) is defined for a non-uniform grid. When the grid is uniform we can obtain (A.8) in two steps: First we take $x_c = y_i$ and observe that $Z_l = -lh$ in (A.6); consequently $\{S_{l,k}\}$ are independent of i. Denoting

$$\text{(A.9)} \qquad \bar{d}_k = h^k d_{i,k}, \qquad c_k = h^k q^{(k)}(y_i)$$

and using the convention $\bar{d}_k = 0$ for $k > r$, we get for $1 \le r \le 6$

$$\text{(A.10)} \qquad \begin{cases} c_0 = & u(y_i) \\ c_1 = & \bar{d}_1 - \bar{d}_2/2 + \bar{d}_3/3 - \bar{d}_4/4 + \bar{d}_5/5 - \bar{d}_6/6 \\ c_2 = & \bar{d}_2 - \bar{d}_3 + 11\bar{d}_4/12 - 5\bar{d}_5/6 + 137\bar{d}_6/180 \\ c_3 = & \bar{d}_3 - 1.5\bar{d}_4 + 1.75\bar{d}_5 - 1.875\bar{d}_6 \\ c_4 = & \bar{d}_4 - 2\bar{d}_5 + 17\bar{d}_6/6 \\ c_5 = & \bar{d}_5 - 2.5\bar{d}_6 \\ c_6 = & \bar{d}_6 \end{cases}$$

$$q(x) = \sum_{k=0}^{r} \frac{c_k}{k!} \left(\frac{x - y_i}{h} \right)^k$$

Thus

$$\text{(A.11)} \qquad h^k q^{(k)}(x_c) = \sum_{l=k}^{r} \frac{c_l}{(l-k)!} \left(\frac{x_c - y_i}{h} \right)^{l-k}$$

Reconstruction via primitive function (RP_j): In this case $I_j = (y_j, y_{j+1})$ is the j-th cell and $x_c = x_j = \frac{1}{2}(y_j + y_{j+1})$ is its center. The given data is

$$\text{(A.12)} \qquad \bar{w}_l = \frac{1}{y_{l+1} - y_l} \int_{y_l}^{y_{l+1}} w(y) dy,$$

from which we evaluate the point values of the primitive function

$$W(y_k) = \sum_{l=0}^{k-1} (y_{l+1} - y_l)\bar{w}_l. \tag{A.13}$$

Applying the algorithm (A.6) - (A.8) to

$$d_{i,k} = W[y_i, ..., y_{i+k}] \tag{A.14}$$

with $i = i(j)$ selected by (3.4), we obtain the values of $q^{(l)}(x_j)$. Using the definition (3.8) in (A.4) we get the coefficients of the Taylor expansion in (A.1) by

$$b_{j,k} = q^{(k+1)}(x_j)/k!. \tag{A.15}$$

We note that when the grid is uniform $y_k = x_{k-1/2}$ and we can also use the algorithm (A.9) - (A.11).

Reconstruction via deconvolution (RD): We recall that RD is used with a uniform grid so that the given data $\bar{w}_l$ can be thought of as point values $\bar{w}(x_l)$ of the sliding average function (1.3). Applying the algorithm (A.9) - (A.11) to

$$d_{i,k} = \bar{w}[x_i, ..., x_{i+k}] \tag{A.16}$$

with $x_c = x_j$ we get in (A.11) for $i = i(j-1)$ the values of

$$h^k \frac{d^k}{dx^k} H_r(x_j - 0; \bar{w}); \tag{A.17a}$$

when we apply this algorithm with $i = i(j)$ and $x_c = x_j$ we get in (A.11) the values of

$$h^k \frac{d^k}{dx^k} H_r(x_j + 0; \bar{w}). \tag{A.17b}$$

Next we evaluate $\bar{D}_{k,j}$ in (3.15) by taking the min mod of the appropriate values in (A.17a) and (A.17b). Finally we use the back-substitution (3.19) to obtain the coefficients of the Taylor expansion (A.1)

$$b_{j,k} = \frac{1}{k!} D_{k,j}/h^k. \tag{A.18}$$

We remark that the use of the algorithms (A.9) - (A.11) is preferable to that of (A.6) - (A.8) since it enables us to save computing time by rearranging the operations (A.16) - (A.17) as follows: First we set $i = i(j)$ in (A.16) and evaluate (A.9) - (A.10). Using the same coefficients c_k in (A.10) we now apply (A.11) to $x_c = x_j$ and $x_c = x_{j+1}$ to obtain $\frac{d^k}{dx^k} H_r(x_j + 0; \bar{w})$ and $\frac{d^k}{dx^k} H_r(x_{j+1} - 0; \bar{w})$, respectively; the min mod operation (3.15) is then performed in a following sweep.

REFERENCES

[1]. M. Ben-Artzi and J. Falcowitz, "An upwind second-order scheme for compressible duct flows," *Siam J. Sci. Comp.,* (1986) to appear.

[2]. S.R. Chakravarthy, A. Harten, and S. Osher, "Essentailly non-oscillatory shock-capturing schemes of arbitrarily high accuracy," *AIAA* 86-0339, (1986), Reno, NA.

[3]. A.J. Chorin, "Random choice solutions of hyperbolic systems, " *J. Comp. Phys.* V. 22 (1976) pp. 517-533.

[4]. P. Colella and P.R. Woodward, "The piecewise-parabolic method (PPM) for gas-dynamical simulations," *J. Comp. Phys.,* V. 54 (1984), 174-201.

[5]. S.K. Godunov, "A finite difference method for the numerical computation of dicontinuous solutions of the equations to fluid dynamics," *Mat. Sb., 47* (1959), pp. 271-290.

[6]. E. Harabetian, "A convergent series expansion for hyperbolic systems of conservation laws," *NASA Contractor Report 172557,* ICASE Report #85-13, 1985.

[7]. A. Harten, "The artificial compression method for computation of shocks and contact-discontinuities: III. Self-adjusting hybrid schemes," *Math. Comp.,* V. 32 (1978) pp. 363-389.

[8]. A. Harten, "On the symmetric form of systems of conservation laws with entropy," *J. Comp. Phys.,* V. 49 (1983), pp. 151-169.

[9]. A. Harten, "High resolution schemes for hyperbolic conservation laws," *J. Comp. Phys.,* V. 49 (1983), pp. 357-393.

[10]. A. Harten, "On a class of High Resolution Total- Variation-Stable Finite-Difference Schemes," *SINUM,* V. 21 (1984), pp. 1-23.

[11]. A. Harten, "On high-order accurate interpolation for non-oscillatory shock capturing schemes," *MRC Technical Summary Report #2829,* University of Wisconsin, (1985).

[12]. A. Harten, "Preliminary results on the extension of ENO schemes to two-dimensional problems," *Proceedings of the International Conference on Hyperbolic Problems,* Saint-Etienne, January 1986 (in preparation).

[13]. A. Harten and J.M. Hyman, "A self adjusting grid for the computation of weak solutions of hyperbolic conservation laws," *J. Comp. Phys.*, V. 50 (1983), pp. 235-269.

[14]. A. Harten, P.D. Lax and B. van Leer, "On upstream differencing and Godunov-type schemes for hyperbolic conservation laws," *SIAM* Rev., 25 (1983), pp. 35-61.

[15]. A. Harten and S. Osher, "Uniformly high-order accurate non-oscillatory schemes, I.," *MRC Technical Sumamry Report #2823,* May 1985, to appear in SINUM.

[16]. A. Harten, B. Engquist, S. Osher and S.R. Chakravarthy, "Uniformly high-order accurate non-oscillatory schemes, II." (in preparation).

[17]. A. Harten, S. Osher, B. Engquist and S.R. Chakravarthy, "Some results on uniformly high-order accurate essentially non-oscillatory schemes," to appear in J. App. Num. Math.

[18]. P.D. Lax, "Weak solutions of nonlinear hyperbolic equations and their numerical computation," *Comm. Pure Appl. Math.* V. 7 (1954) pp. 159-193.

[19]. P.D. Lax, "Hyperbolic systems of conservation laws and the mathematical theory of shock waves," *Society for Industrial and Applied Mathematics,* Philadelphia, 1972.

[20]. P.D. Lax and B. Wendroff, "Systems of conservation laws," *Comm. Pure Appl. Math.*, V. 13 (1960), pp. 217-237.

[21]. P.D. Lax and B. Wendroff, "Difference schemes for hyperbolic equations with high-order of accuracy," *Comm. Pure Appl. Math.* V. 17 (1964) pp. 381-398.

[22]. B. van Leer, "Towards the ultimate conservative difference schemes V. A second order sequel to Godunov's method," *J. Comp. Phys.*, V. 32, (1979) pp. 101-136.

[23]. S. Osher, "Riemann solvers, the entropy condition, and difference approximations," *SINUM,* V. 21, (1984), pp. 217-235.

[24]. S. Osher and E. Tadmor, "On the convergence of difference approximations to conservation laws," submitted to *Math-Comp.*

[25]. P.L. Roe, "Approximate Riemann solvers, parameter vectors, and difference schemes," *J. Comp. Phys.*, V. 43 (1981), pp. 357-372.

[26]. P.L. Roe, "Some contributions to the modeling of discontinuous flows." in *Lectures in Applied Mathematics,* V. 22 (1985) pp. 163-193.

[27]. M. Sever (Mock), "Order of dissipation near rarefaction centers," in Progress and Supercomputing in Computational Fluid Dynamics, *Proceedings of U.S.-Israel Workshop,* 1984, E.M. Murman and S.S. Abarbanel, Editors.

[28]. G.A. Sod, "A survey of several finite difference methods for systems of nonlinear hyperbolic conservation laws." *J. Comp. Phys.*, V. 27 (1978) pp. 1-31.

[29]. G. Strang, "On the construction and comparison of difference schemes," *SINUM,* V. 5 (1968) pp. 506-517.

[30]. P.K. Sweby, "High resolution schemes using flux limiters for hyperbolic conservation laws," *SINUM,* V. 21 (1984), pp. 995-1011.

[31]. P. Woodward and P. Colella, "The numerical simulation of two-dimensional fluid flow with strong shock," *J. Comp. Phys.*, V. 54 (1984) pp. 115-173.

[32]. Xiong-hau Wu and You-lan Zhu, "A scheme of the singularity- separating method for the non-convex problem," Computer Center, Academia Sinica, Preprint.

Table 1a. Solution of the periodic IVP (7.1) at $t = 0.3$ by ENO schemes based on RP.

	J	r = 1	r_c	r = 2	r_c	r = 3	r_c	r = 4	r_c	r = 5	r_c
L_∞-ERROR	8	1.582×10^{-1}		9.047×10^{-2}		3.804×10^{-2}		2.715×10^{-2}		2.117×10^{-2}	
			0.80		1.07		2.24		2.76		2.86
	16	9.082×10^{-2}		4.300×10^{-2}		8.038×10^{-3}		3.998×10^{-3}		2.906×10^{-3}	
			0.87		1.24		2.10		3.18		3.76
	32	4.964×10^{-2}		1.819×10^{-2}		1.876×10^{-3}		4.423×10^{-4}		2.151×10^{-4}	
			0.91		1.32		2.35		3.39		3.65
	64	2.648×10^{-2}		7.296×10^{-3}		3.684×10^{-4}		4.211×10^{-5}		1.713×10^{-5}	
			0.92		1.33		2.14		3.02		4.50
	128	1.404×10^{-2}		2.900×10^{-3}		8.356×10^{-5}		5.188×10^{-6}		7.562×10^{-7}	
L_1-ERROR	8	8.440×10^{-2}		4.507×10^{-2}		1.669×10^{-2}		1.003×10^{-2}		7.000×10^{-3}	
			0.98		1.79		2.70		3.21		3.57
	16	4.279×10^{-2}		1.304×10^{-2}		2.574×10^{-3}		1.086×10^{-3}		5.875×10^{-4}	
			0.97		1.81		2.69		3.53		4.08
	32	2.186×10^{-2}		3.707×10^{-3}		3.992×10^{-4}		9.400×10^{-5}		3.462×10^{-5}	
			0.96		1.89		2.69		3.57		4.48
	64	1.124×10^{-2}		9.980×10^{-4}		6.165×10^{-5}		7.905×10^{-6}		1.546×10^{-6}	
			0.99		1.83		2.56		3.53		4.62
	128	5.675×10^{-3}		2.813×10^{-4}		1.042×10^{-5}		6.835×10^{-7}		6.270×10^{-8}	

Table 1b. Solution of the periodic IVP (7.1) at $t = 0.3$ by ENO schemes based on RD.

	J	r = 1	r_c	r = 2	r_c	r = 3	r_c	r = 4	r_c	r = 5	r_c
L_∞-ERROR	8	1.582×10^{-1}		5.204×10^{-2}		4.484×10^{-2}		2.787×10^{-2}		2.115×10^{-2}	
			0.80		1.94		3.01		2.97		3.17
	16	9.082×10^{-2}		1.352×10^{-2}		5.577×10^{-3}		3.565×10^{-3}		2.343×10^{-3}	
			0.87		1.92		2.67		3.24		3.61
	32	4.964×10^{-2}		3.562×10^{-3}		8.791×10^{-4}		3.777×10^{-4}		1.191×10^{-4}	
			0.91		2.05		3.96		3.69		5.20
	64	2.648×10^{-2}		8.610×10^{-4}		5.658×10^{-5}		2.927×10^{-5}		5.242×10^{-6}	
			0.92		2.30		3.22		4.76		5.36
	128	1.404×10^{-2}		1.748×10^{-4}		6.081×10^{-6}		1.077×10^{-6}		1.276×10^{-7}	
L_1-ERROR	8	8.440×10^{-2}		2.231×10^{-2}		1.333×10^{-2}		8.600×10^{-3}		6.045×10^{-3}	
			0.98		2.40		3.26		3.71		3.90
	16	4.279×10^{-2}		4.228×10^{-3}		1.388×10^{-3}		6.575×10^{-4}		4.063×10^{-4}	
			0.97		2.30		3.31		4.02		4.40
	32	2.186×10^{-2}		8.565×10^{-4}		1.399×10^{-4}		4.056×10^{-5}		1.919×10^{-5}	
			0.96		2.23		3.67		4.39		5.40
	64	1.124×10^{-2}		1.826×10^{-4}		1.096×10^{-5}		1.936×10^{-6}		4.547×10^{-7}	
			0.99		2.18		3.35		4.53		5.53
	128	5.675×10^{-3}		4.039×10^{-5}		1.071×10^{-6}		8.385×10^{-8}		9.810×10^{-9}	

Table 2a. Solution of the IBVP (7.1), (7.5) at $t = 0.3$ by ENO schemes based on RP.

	J	r = 1	r_c	r = 2	r_c	r = 3	r_c	r = 4	r_c	r = 5	r_c
L_∞-ERROR	8	1.471×10^{-1}		9.047×10^{-2}		2.849×10^{-2}		2.936×10^{-2}		1.766×10^{-2}	
			0.68		1.07		0.77		1.56		0.69
	16	9.184×10^{-2}		4.300×10^{-2}		1.672×10^{-2}		9.943×10^{-3}		1.096×10^{-2}	
			0.77		1.24		2.75		2.98		3.58
	32	5.382×10^{-2}		1.819×10^{-2}		2.477×10^{-3}		1.275×10^{-3}		9.149×10^{-4}	
			0.75		1.32		2.75		5.14		5.56
	64	3.198×10^{-2}		7.296×10^{-3}		3.684×10^{-4}		3.614×10^{-5}		1.944×10^{-5}	
			0.88		1.33		2.14		2.83		4.69
	128	1.742×10^{-2}		2.900×10^{-3}		8.356×10^{-5}		5.089×10^{-6}		7.540×10^{-7}	
L_1-ERROR	8	7.745×10^{-2}		3.355×10^{-2}		1.221×10^{-2}		8.065×10^{-3}		5.265×10^{-3}	
			0.95		1.33		1.60		2.40		1.92
	16	4.015×10^{-2}		1.339×10^{-2}		4.032×10^{-3}		1.528×10^{-3}		1.389×10^{-3}	
			0.91		1.88		3.14		3.40		4.15
	32	2.143×10^{-2}		3.643×10^{-3}		4.563×10^{-4}		1.445×10^{-4}		7.810×10^{-5}	
			0.96		1.86		2.89		4.27		5.04
	64	1.102×10^{-2}		1.003×10^{-3}		6.175×10^{-5}		7.505×10^{-6}		2.371×10^{-6}	
			0.97		1.81		2.70		3.58		5.07
	128	5.630×10^{-3}		2.855×10^{-4}		9.485×10^{-6}		6.285×10^{-7}		7.060×10^{-8}	

Table 2b. Solution of the IBVP (7.1), (7.5) at t = 0.3 by ENO schemes based on RD.

	J	r = 1	r_c	r = 2	r_c	r = 3	r_c	r = 4	r_c	r = 5	r_c
L_∞-ERROR	8	1.471×10^{-2}		3.264×10^{-2}		3.122×10^{-2}		1.799×10^{-2}		9.192×10^{-3}	
			0.68		0.78		1.86		0.69		-.65
	16	9.184×10^{-2}		1.907×10^{-2}		8.571×10^{-3}		1.114×10^{-2}		1.441×10^{-2}	
			0.77		2.46		2.65		3.58		3.54
	32	5.382×10^{-2}		3.454×10^{-3}		1.366×10^{-3}		9.312×10^{-4}		1.240×10^{-3}	
			0.75		2.06		4.71		5.01		6.96
	64	3.198×10^{-2}		8.302×10^{-4}		5.220×10^{-5}		2.897×10^{-5}		9.727×10^{-6}	
			0.88		2.24		3.12		4.75		6.07
	128	1.742×10^{-2}		1.754×10^{-4}		5.996×10^{-6}		1.075×10^{-6}		1.473×10^{-7}	
L_1-ERROR	8	7.745×10^{-2}		1.488×10^{-2}		8.425×10^{-3}		5.480×10^{-3}		2.240×10^{-3}	
			0.95		1.52		2.45		2.00		0.88
	16	4.015×10^{-2}		5.190×10^{-3}		1.540×10^{-3}		1.372×10^{-3}		1.217×10^{-3}	
			0.91		2.57		3.18		4.07		3.83
	32	2.143×10^{-2}		8.740×10^{-4}		1.694×10^{-4}		8.105×10^{-5}		8.570×10^{-5}	
			0.96		2.22		4.00		4.90		6.26
	64	1.102×10^{-2}		1.879×10^{-4}		1.059×10^{-5}		2.747×10^{-6}		1.119×10^{-6}	
			0.97		2.15		3.39		4.90		6.68
	128	5.630×10^{-3}		4.219×10^{-5}		1.012×10^{-6}		9.200×10^{-8}		1.092×10^{-8}	

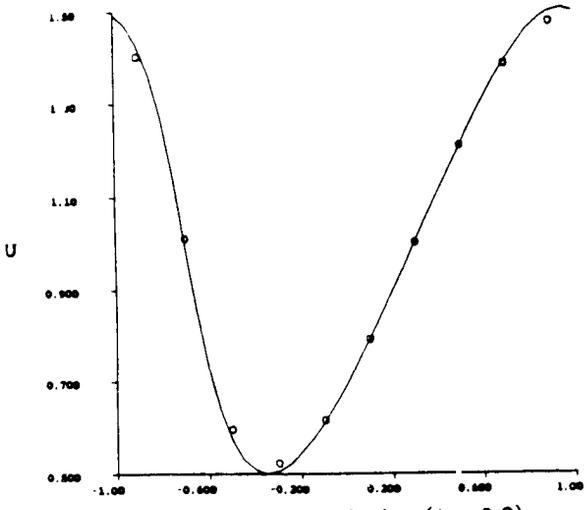

Figure 1a: Second-order solution ($t = 0.3$)

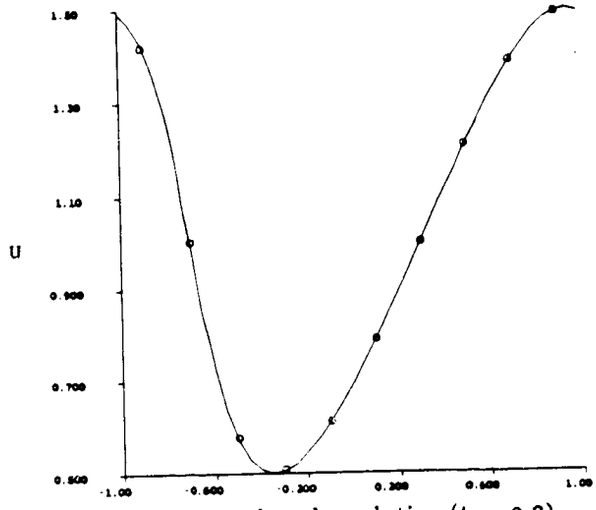

Figure 1b: Fourth-order solution ($t = 0.3$)

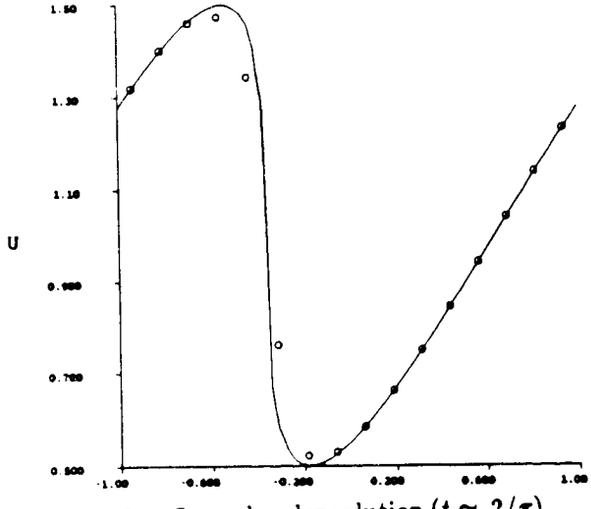

Figure 2a: Second-order solution ($t \approx 2/\pi$)

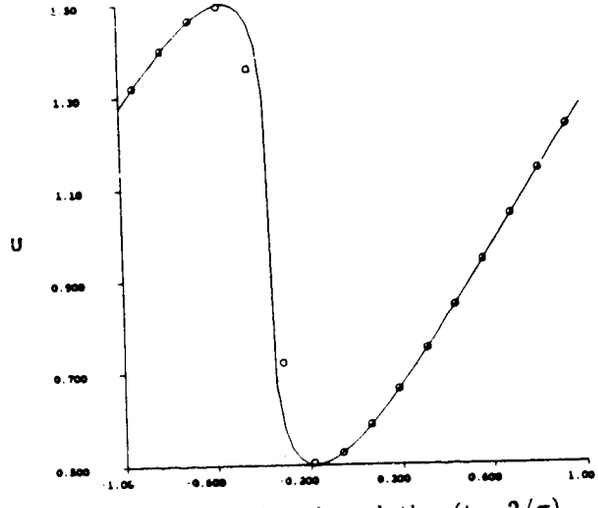

Figure 2b: Fourth-order solution ($t \approx 2/\pi$)

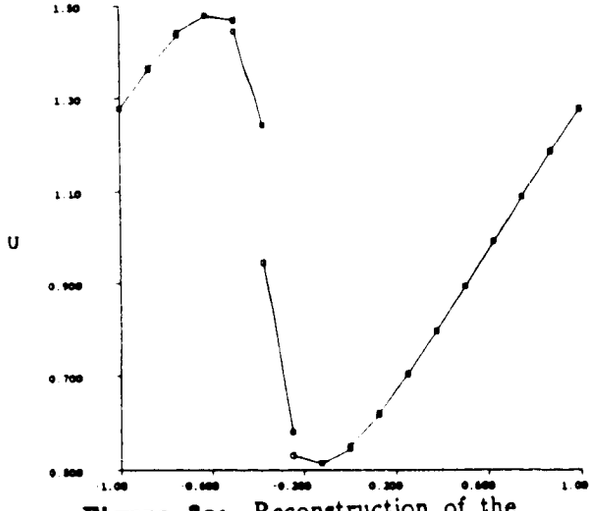

Figure 3a: Reconstruction of the solution in figure 2a ($r = 2$)

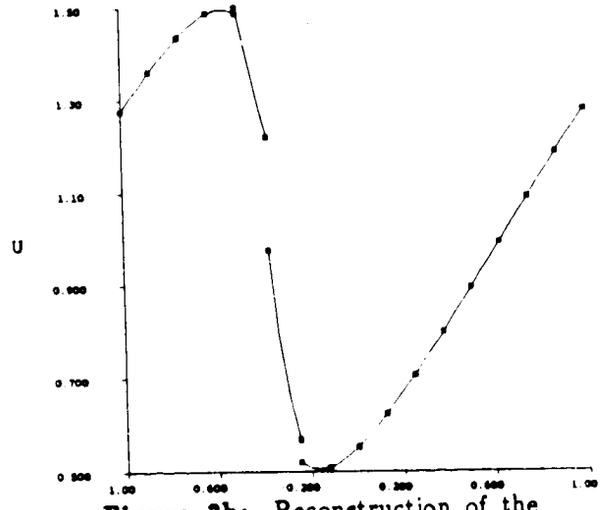

Figure 3b: Reconstruction of the solution in figure 2b ($r = 4$)

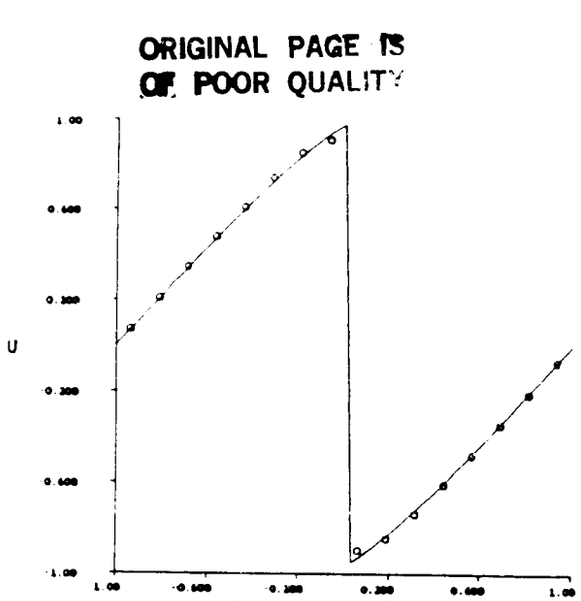

Figure 4a: "Second-order" solution of the IBVP (7.5)

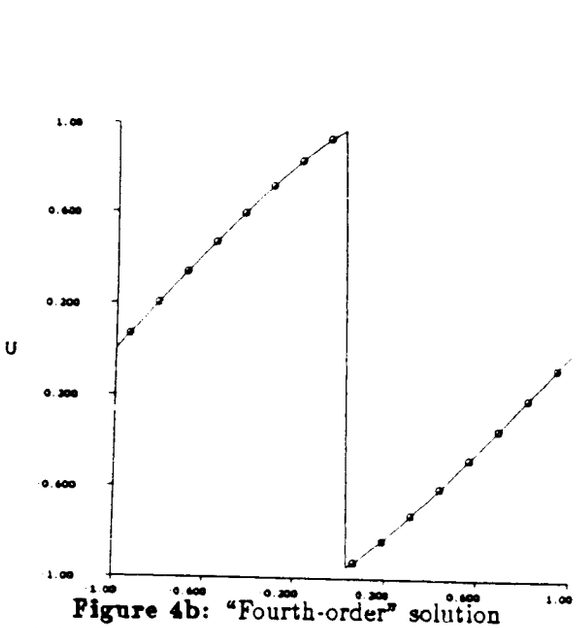

Figure 4b: "Fourth-order" solution of the IBVP (7.5)

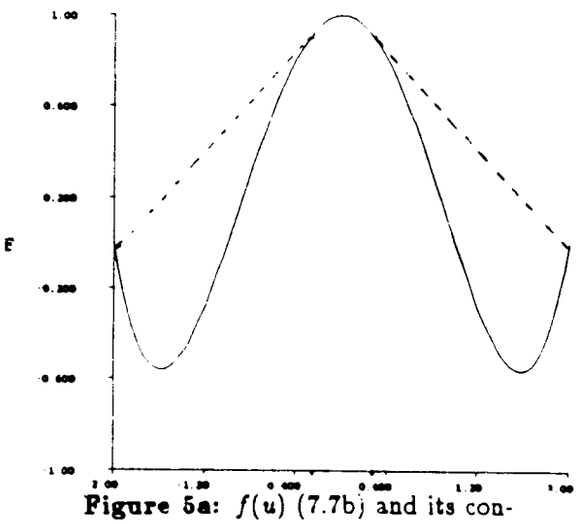

Figure 5a: $f(u)$ (7.7b) and its concave hull for $u_L = 2$, $u_R = -2$

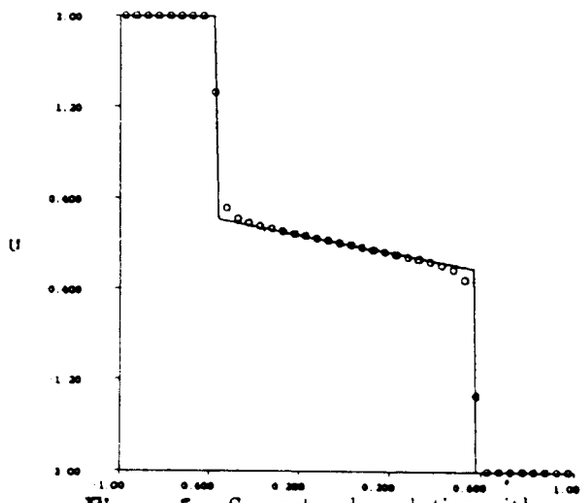

Figure 5c: Second-order solution with exact f^R ($J = 40$, $N = 80$)

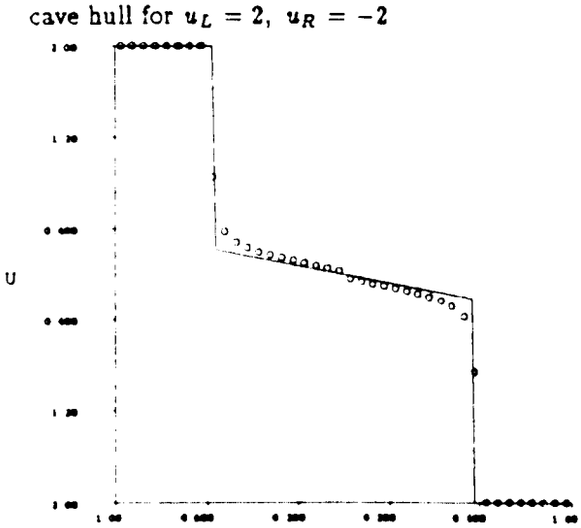

Figure 5b: First-order solution with exact f^R ($J = 40$, $N = 80$)

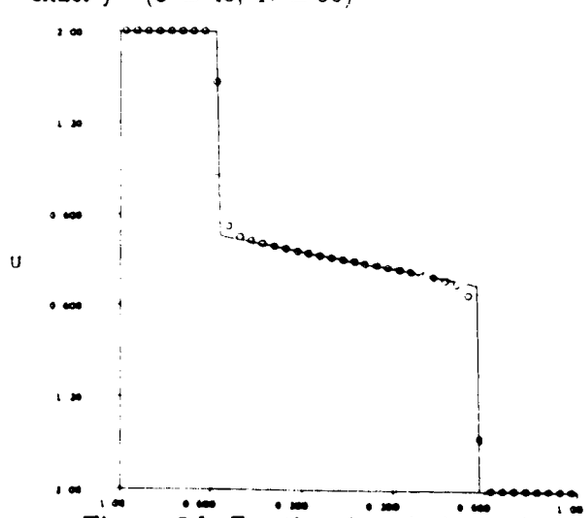

Figure 5d: Fourth-order solution with exact f^R ($J = 40$, $N = 80$)

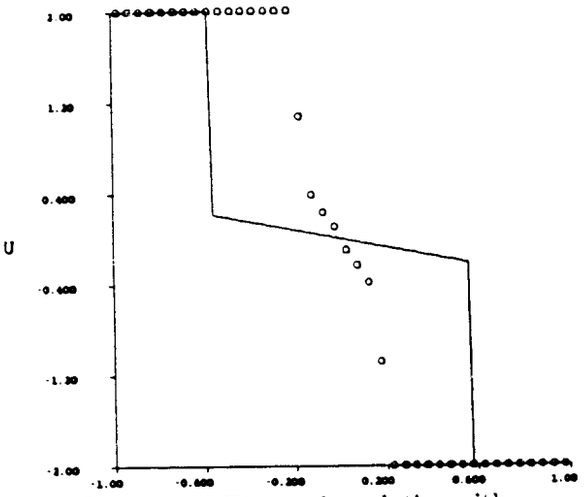

Figure 6a: First-order solution with f^{ROE} $(J = 40,\ N = 80)$

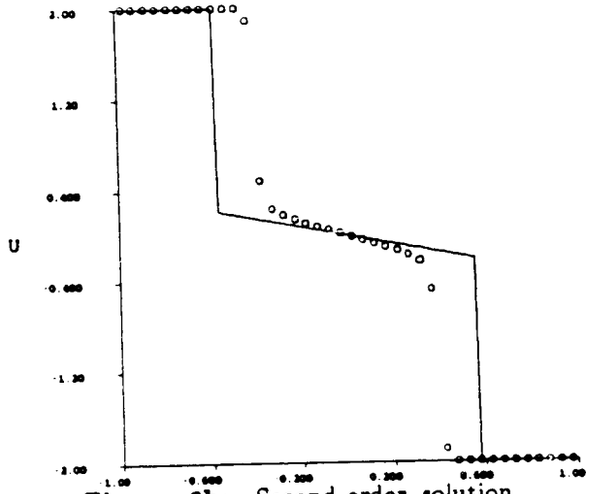

Figure 6b: Second-order solution with f^{ROE} $(J = 40,\ N = 80)$

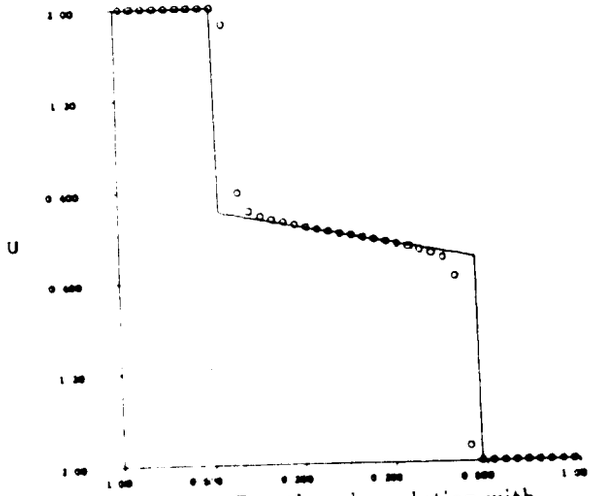

Figure 6c: Fourth-order solution with f^{ROE} $(J = 40,\ N = 80)$

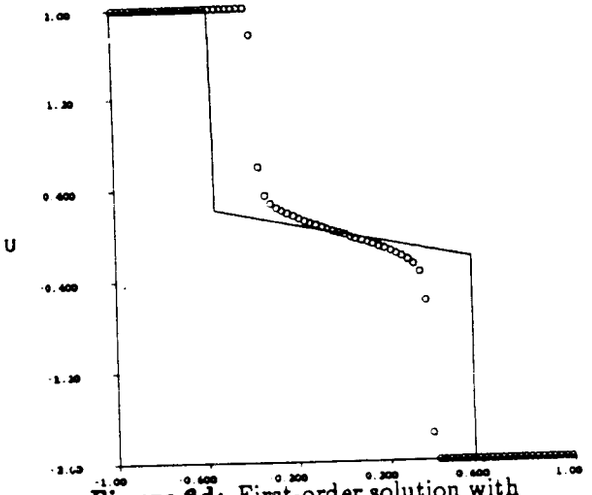

Figure 6d: First-order solution with f^{ROE} $(J = 80,\ N = 160)$

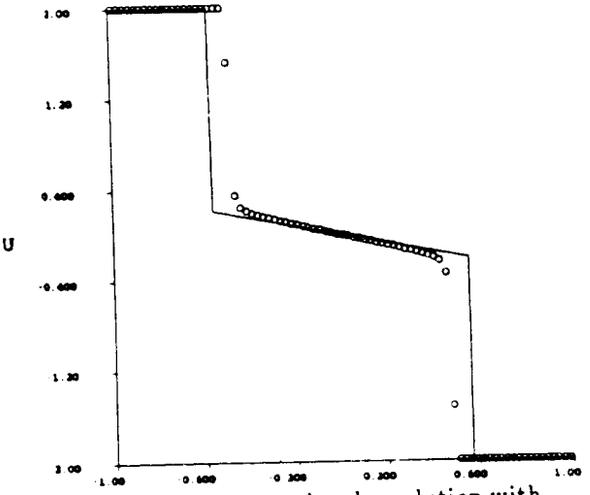

Figure 6e: Second-order solution with f^{ROE} $(J = 80,\ N = 160)$

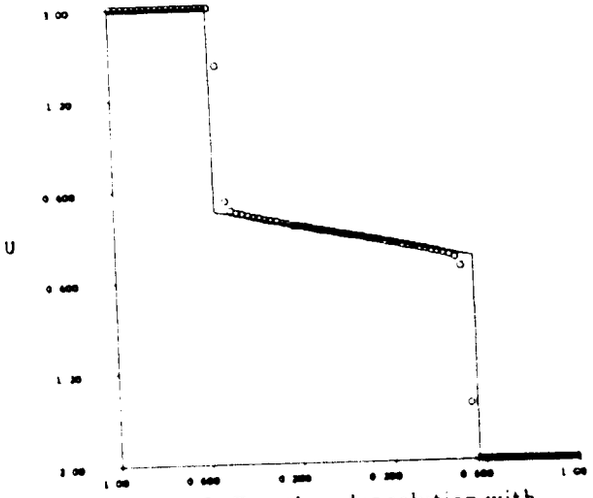

Figure 6f: Fourth-order solution with f^{ROE} $(J = 80,\ N = 160)$

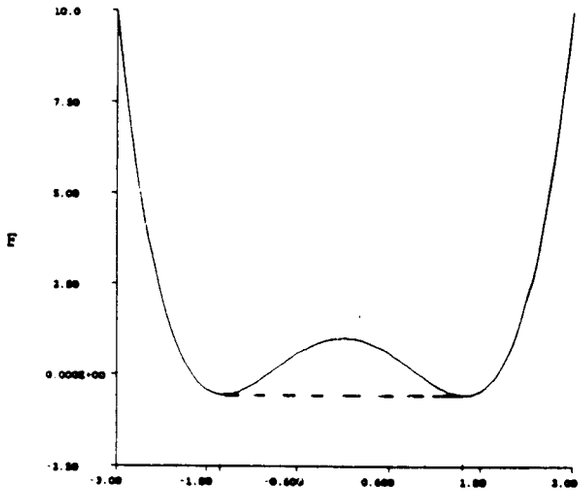

Figure 7a: $f(u)$ (7.7b) and its convex hull for $u_L = -3,\ u_R = 3$

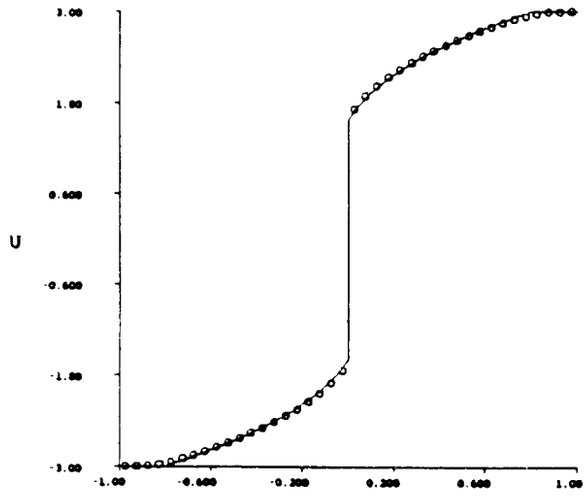

Figure 7c: Second-order solution with exact f^R ($J = 40,\ N = 20$)

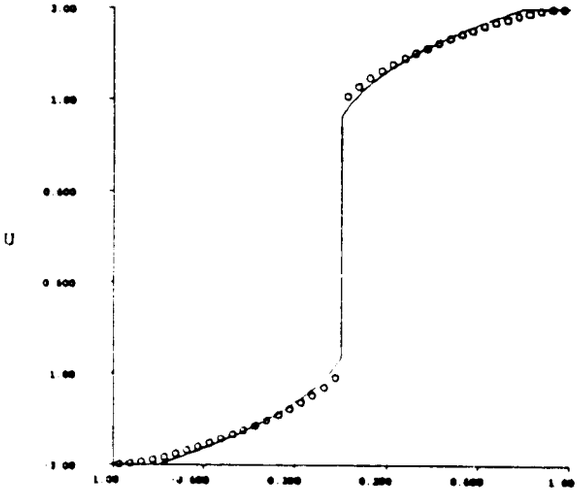

Figure 7b: First-order solution with exact f^R ($J = 40,\ N = 20$)

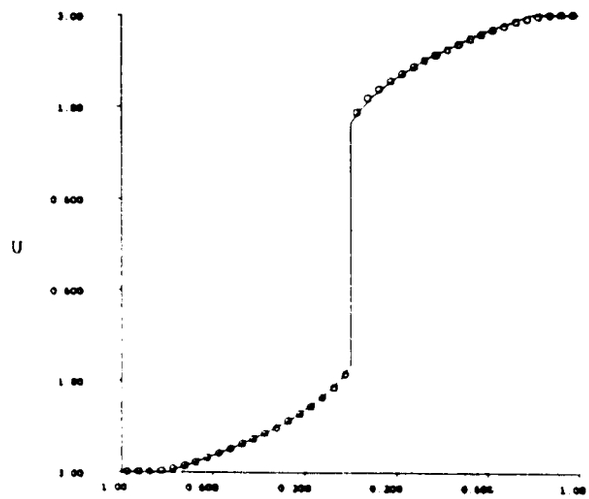

Figure 7d: Fourth-order solution with exact f^R ($J = 40,\ N = 20$)

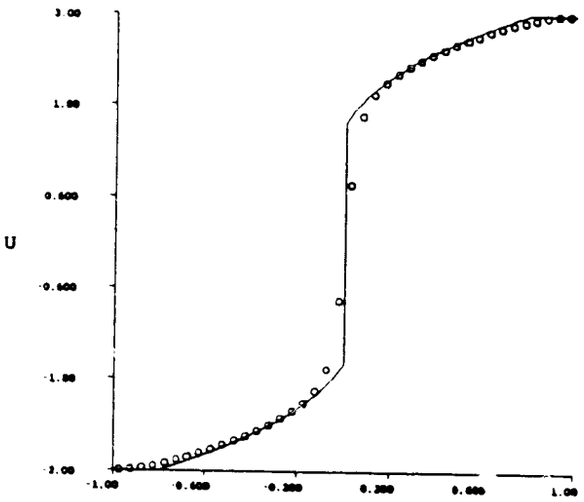

Figure 8a: First-order solution with f^{ROE} ($J = 40,\ N = 20$)

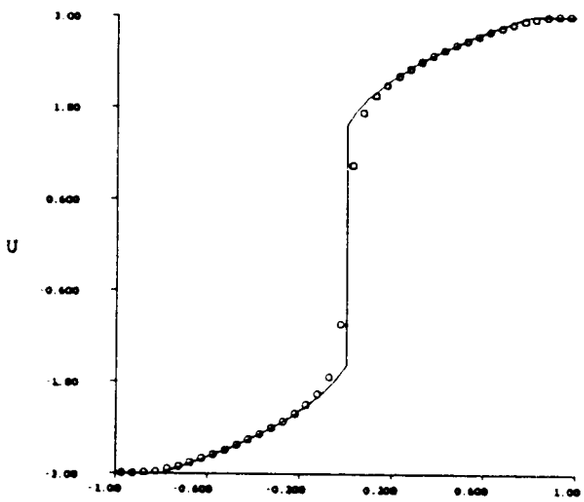

Figure 8b: Second-order solution with f^{ROE} ($J = 40,\ N = 20$)

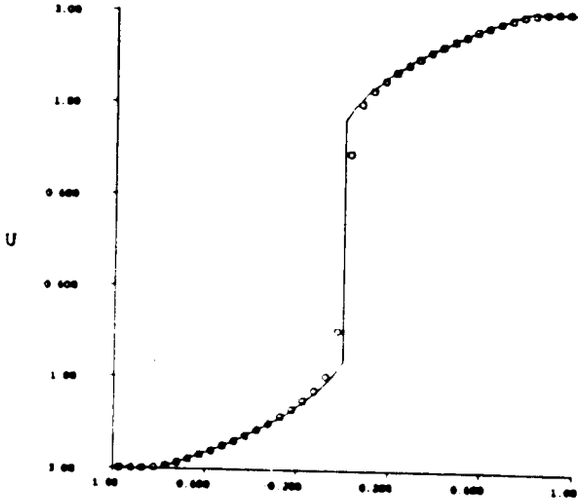

Figure 8c: Fourth-order solution with f^{ROE} ($J = 40,\ N = 20$)

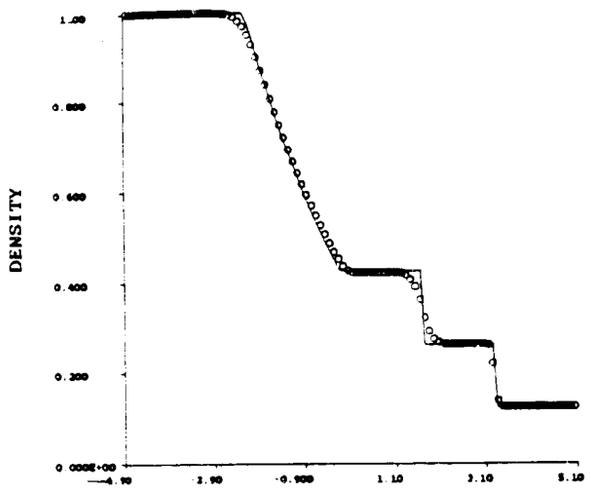

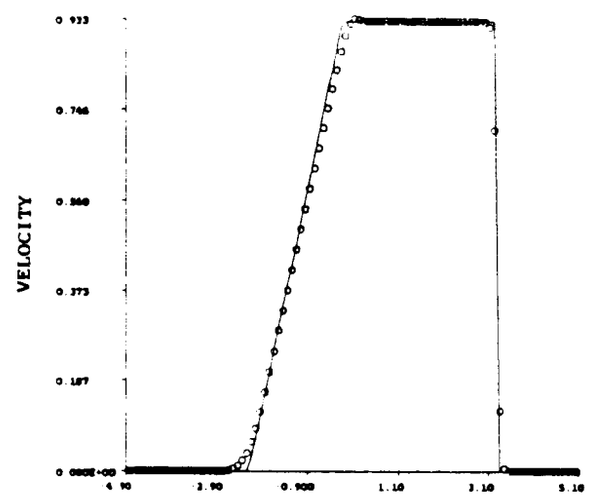

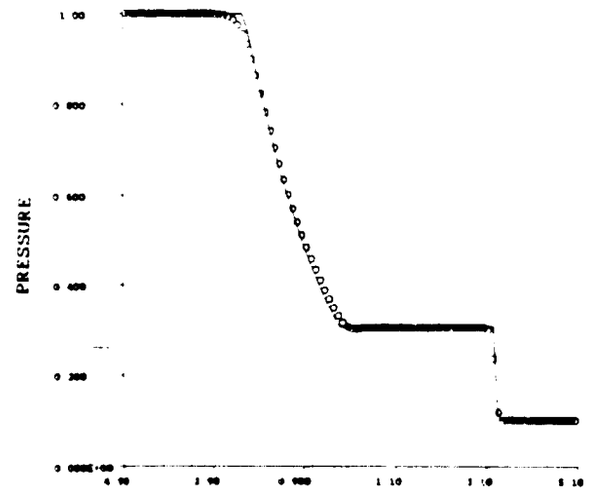

Figure 9: "Second-order" solution of Sod's problem (characteristic reconstruction).

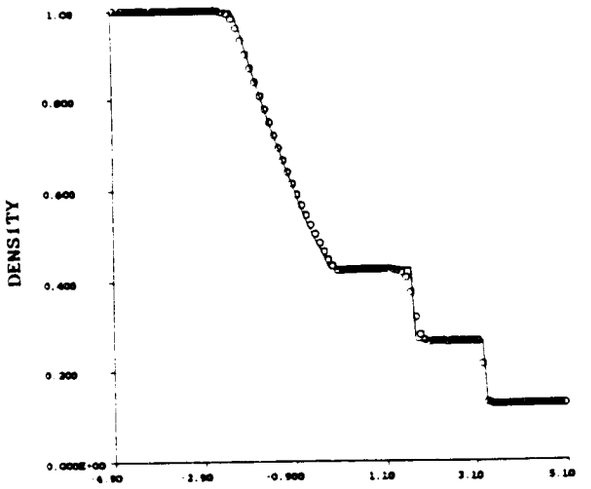

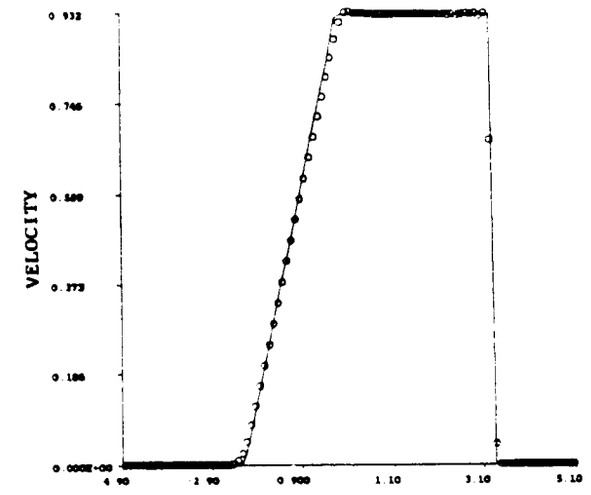

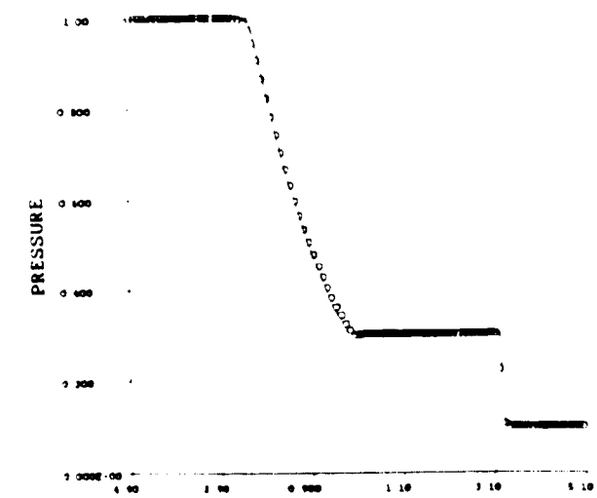

Figure 10: "Fourth-order" solution of Sod's problem (characteristic reconstruction).

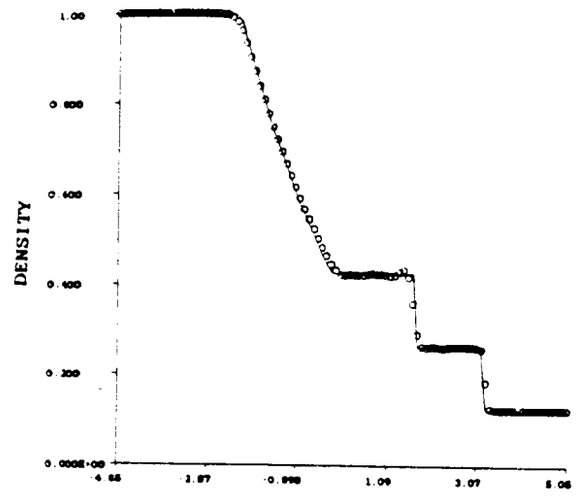

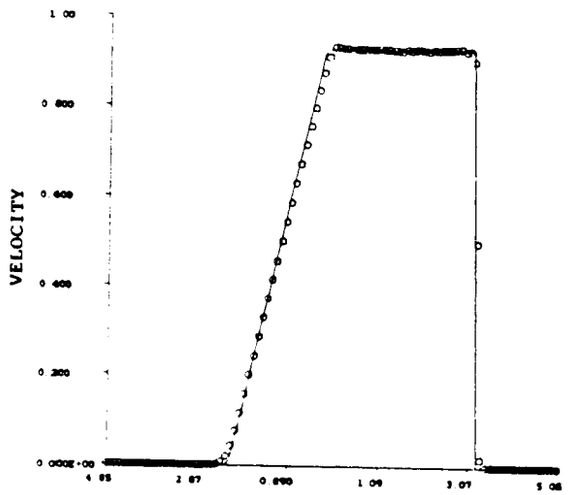

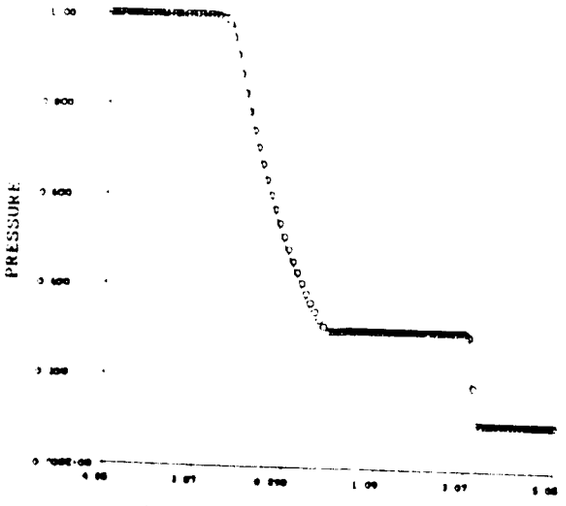

Figure 11: "Fourth-order" solution with component-wise reconstruction of Sod's problem.

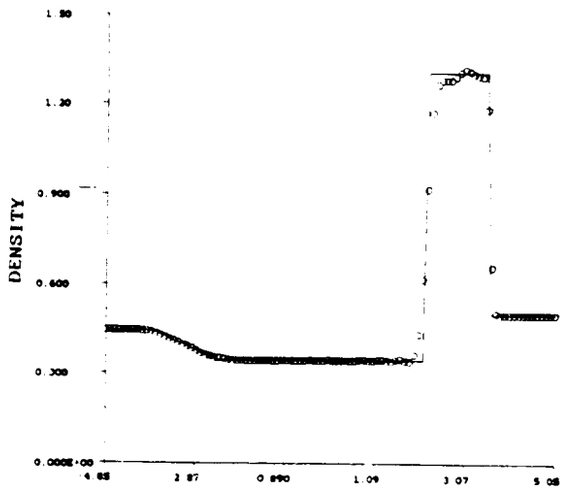

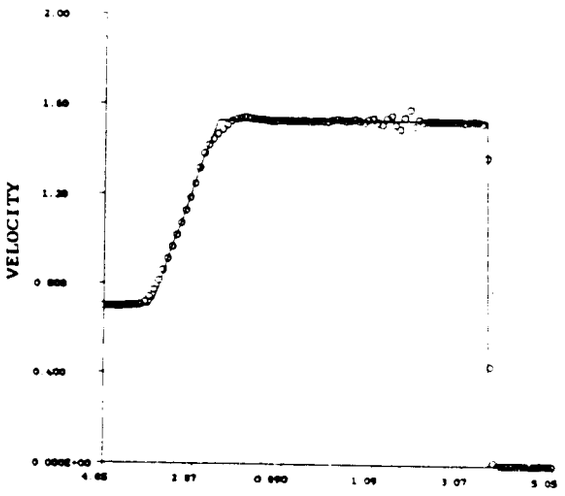

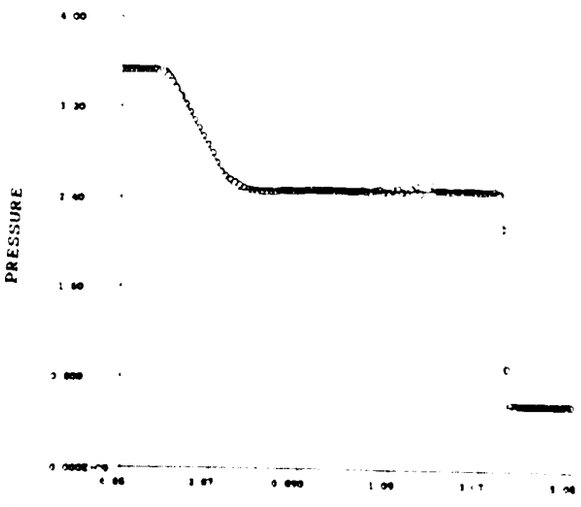

Figure 12: "Fourth-order" solution with component-wise reconstruction of Lax's problem.

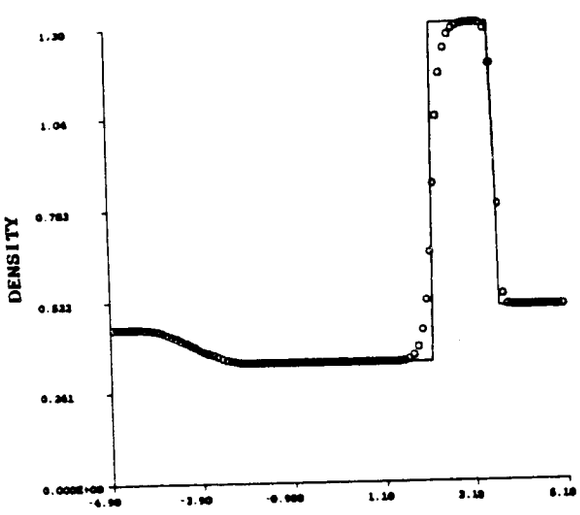

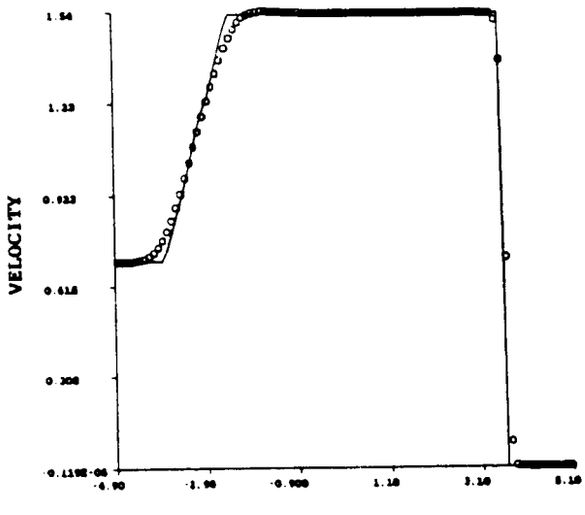

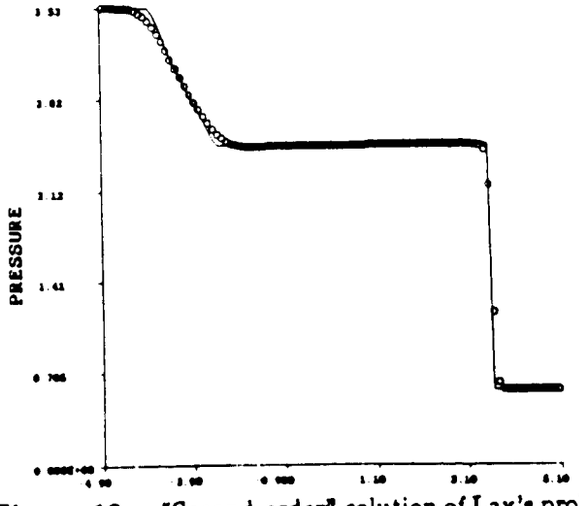

Figure 13: "Second-order" solution of Lax's problem (characteristic reconstruction).

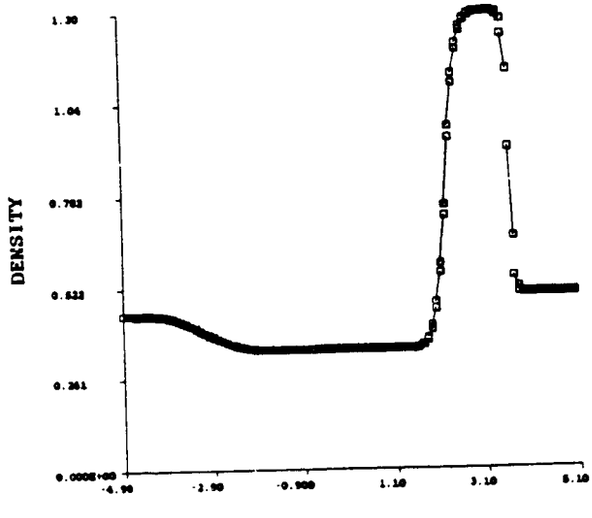

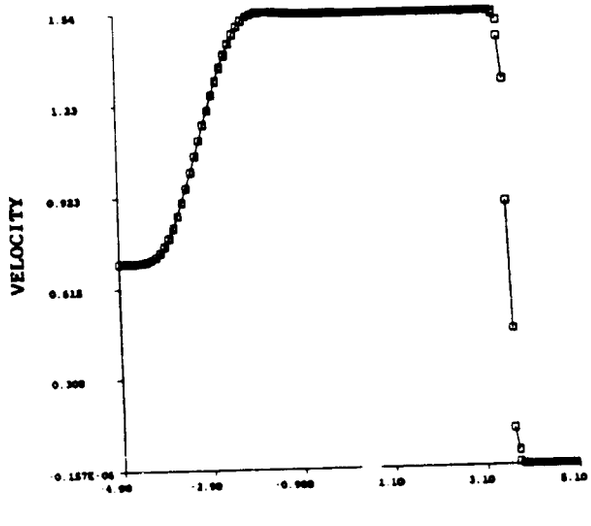

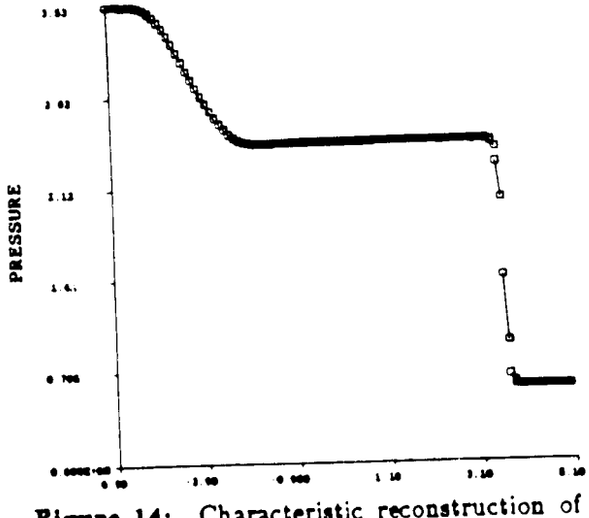

Figure 14: Characteristic reconstruction of the "second-order" solution in Figure 13.

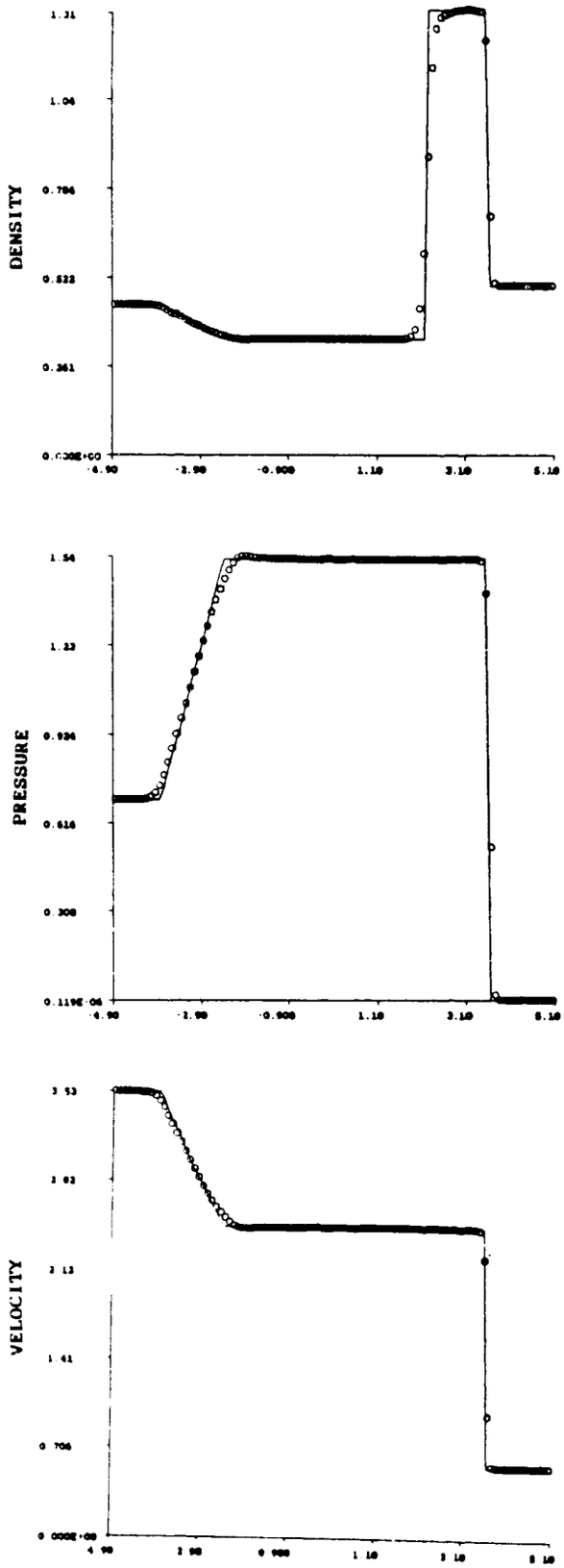

Figure 15: "Fourth-order" solution of Lax's problem (characteristic reconstruction).

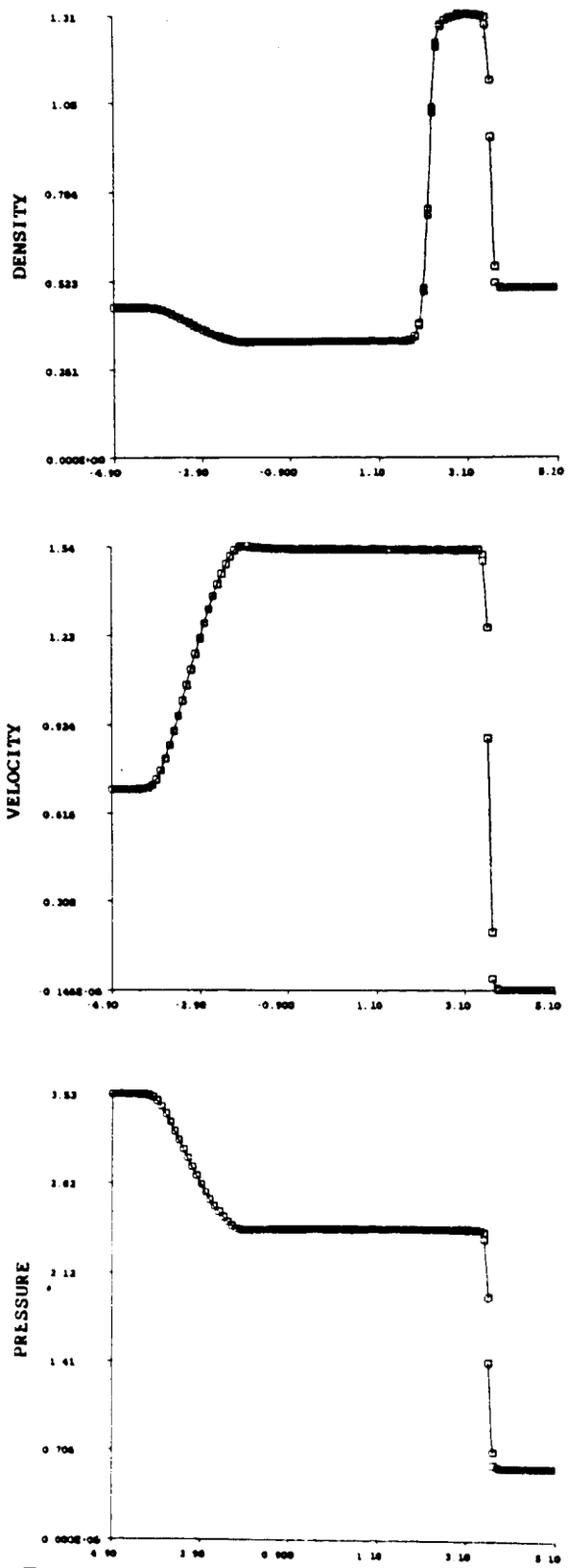

Figure 16: Characteristic reconstruction of the "fourth-order" solution in Figure 15.

Figure 17a: $t = 0.010$

Figure 17b: $t = 0.016$

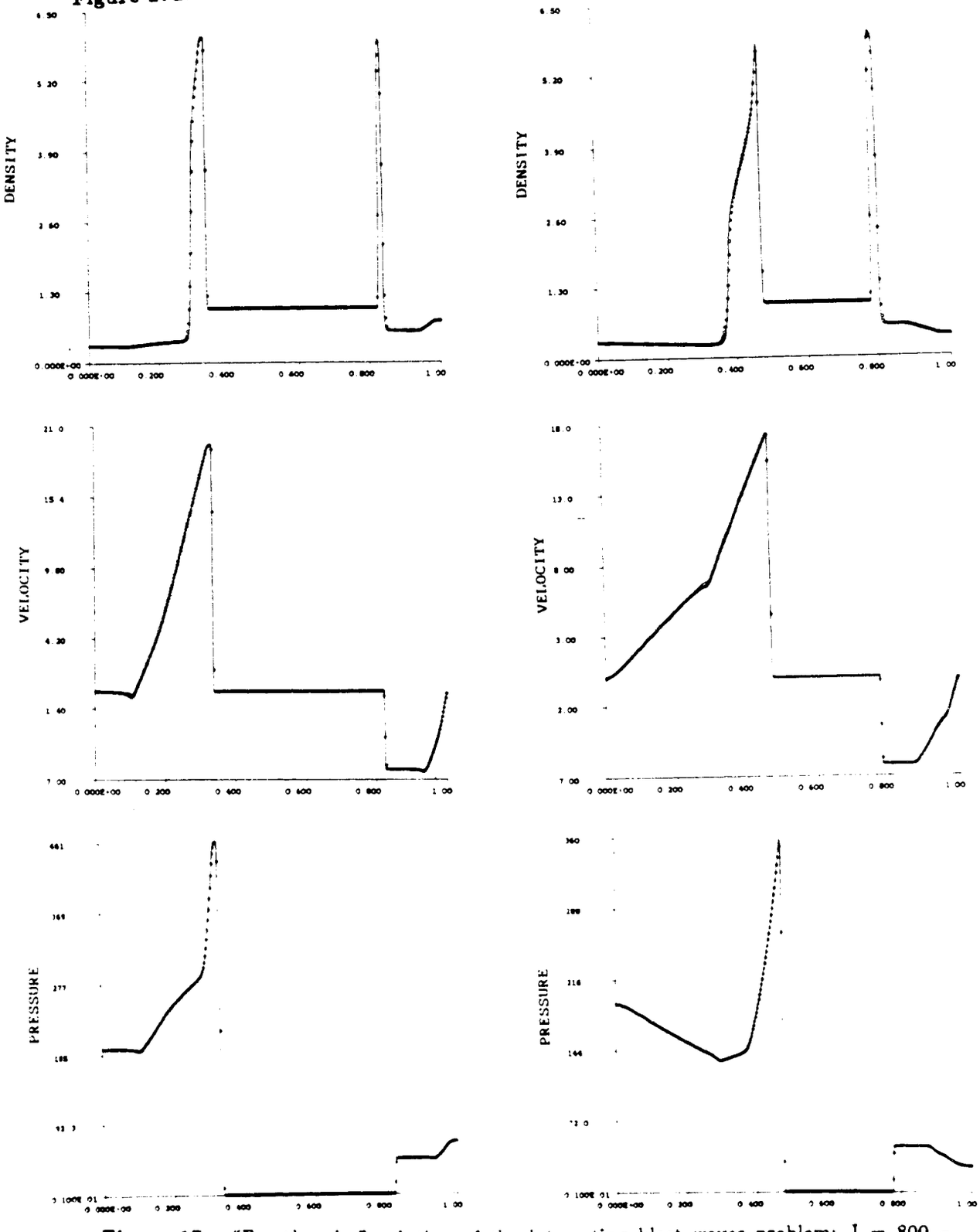

Figure 17: "Fourth-order" solution of the interacting blast waves problem; J = 800 – continuous line; J = 400 – circles.

Figure 17c: $t = 0.026$

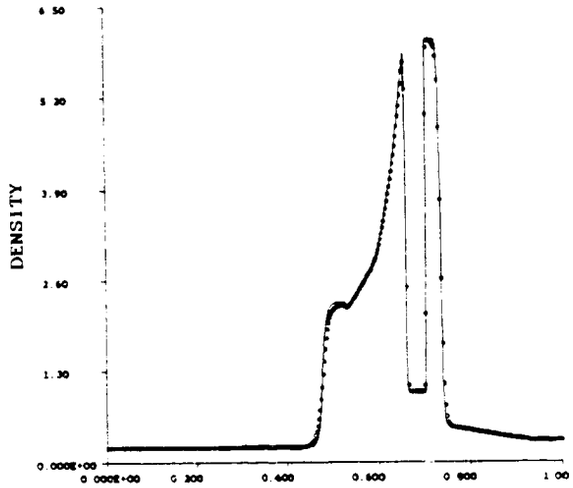

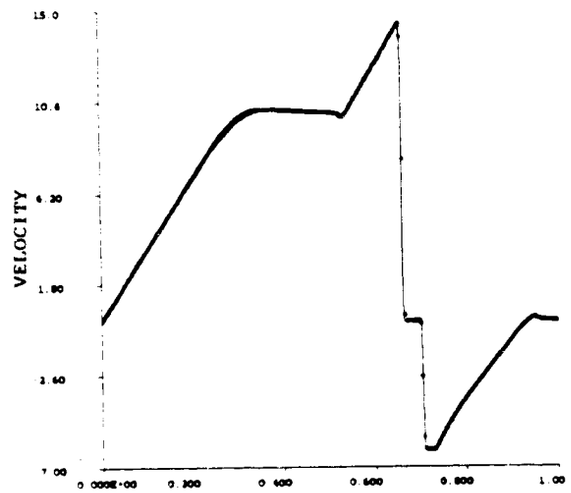

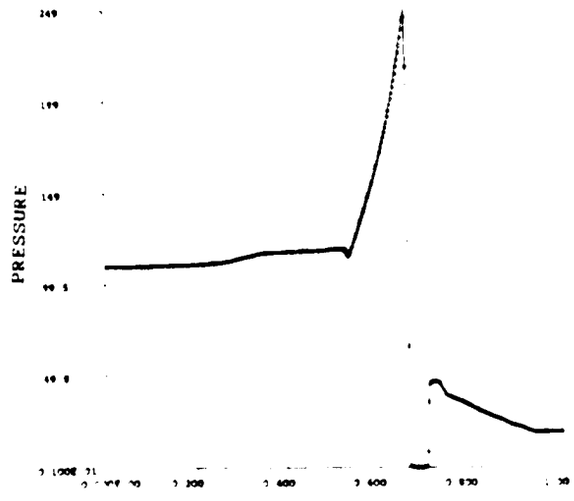

Figure 17d: $t = 0.028$

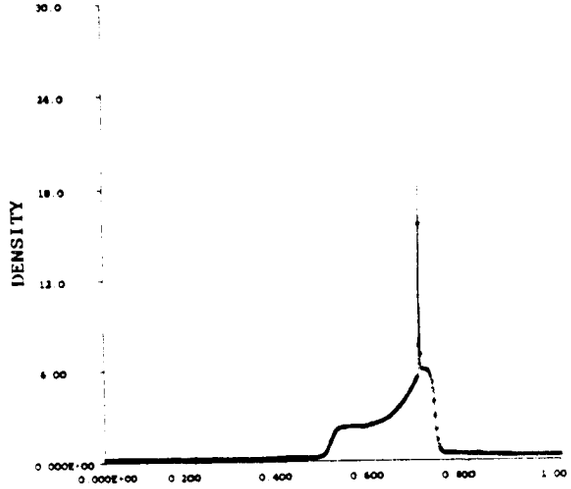

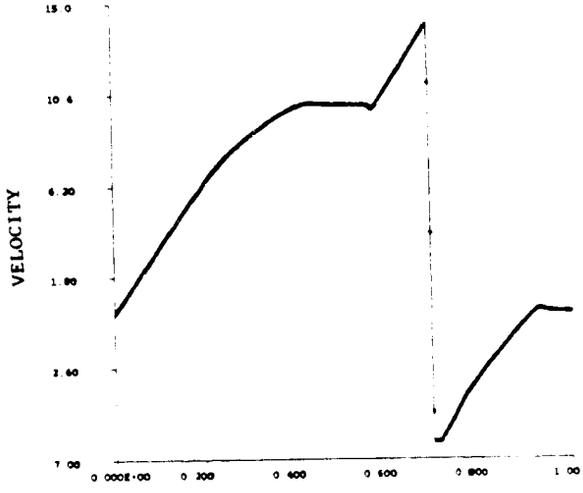

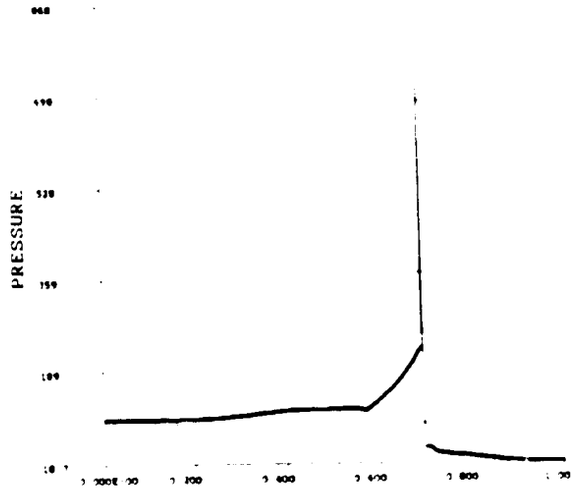

Figure 17e: $t = 0.030$

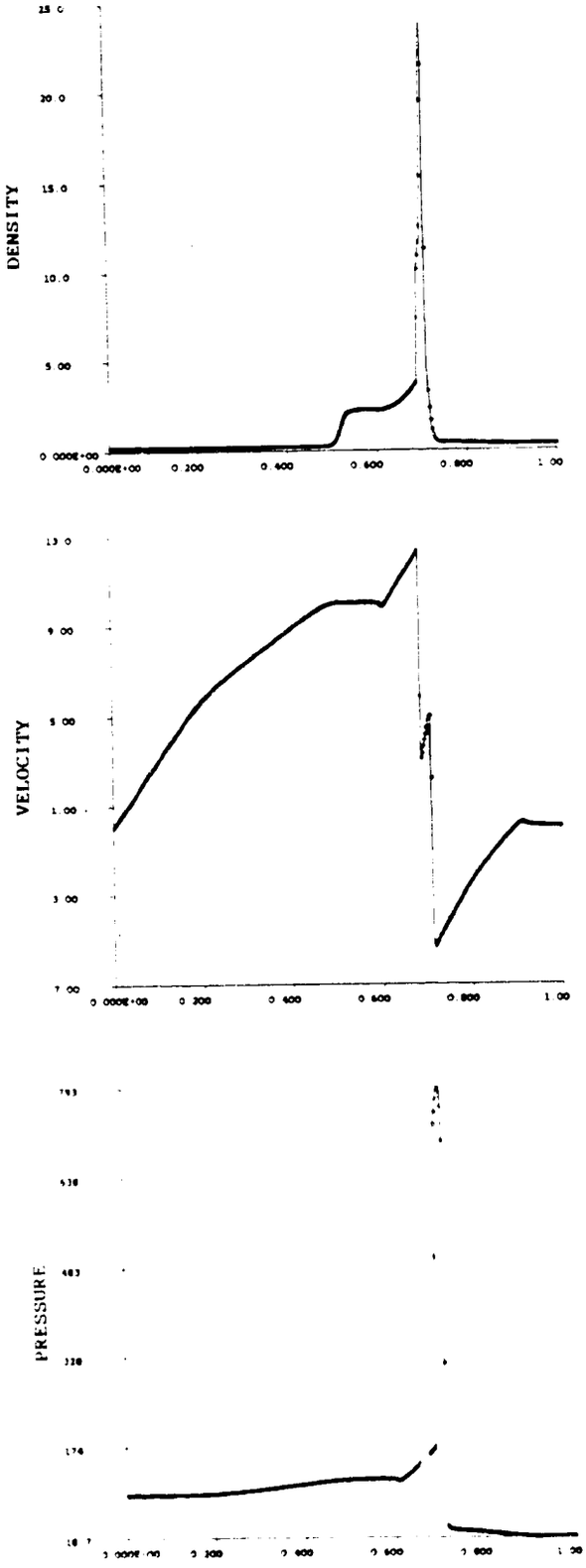

Figure 17f: $t = 0.032$

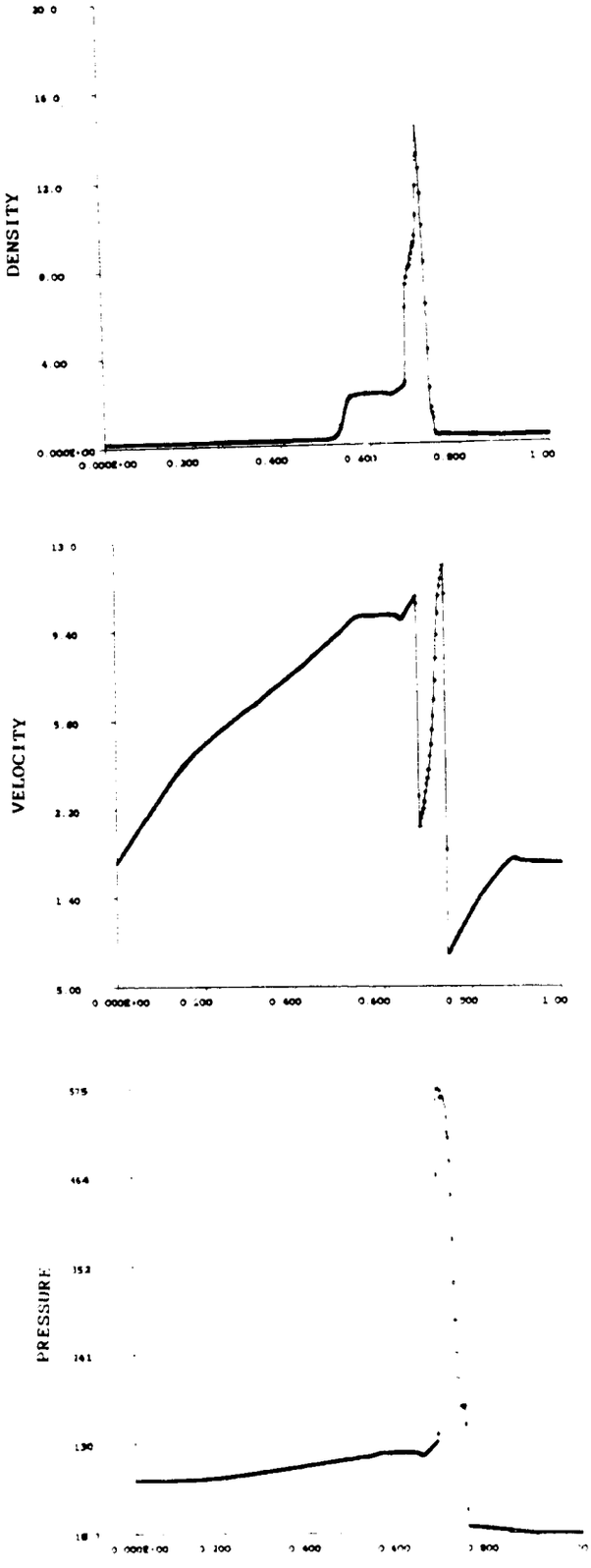

Figure 17g: $t = 0.034$

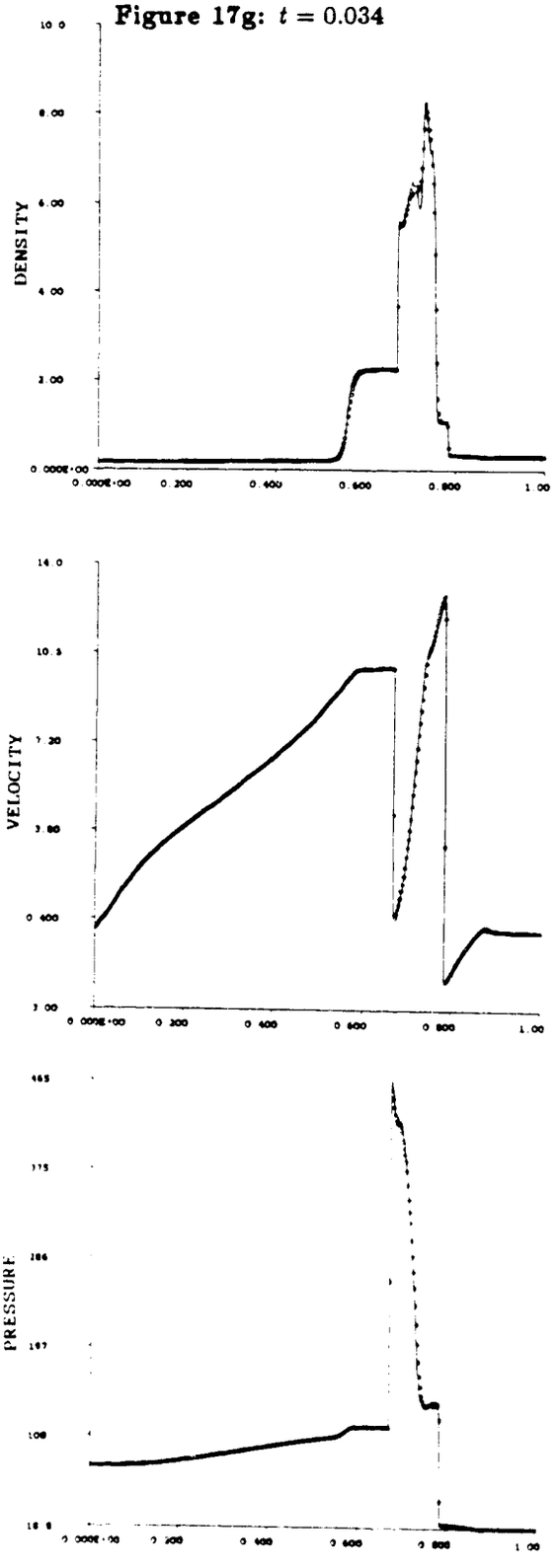

Figure 17h: $t = 0.038$

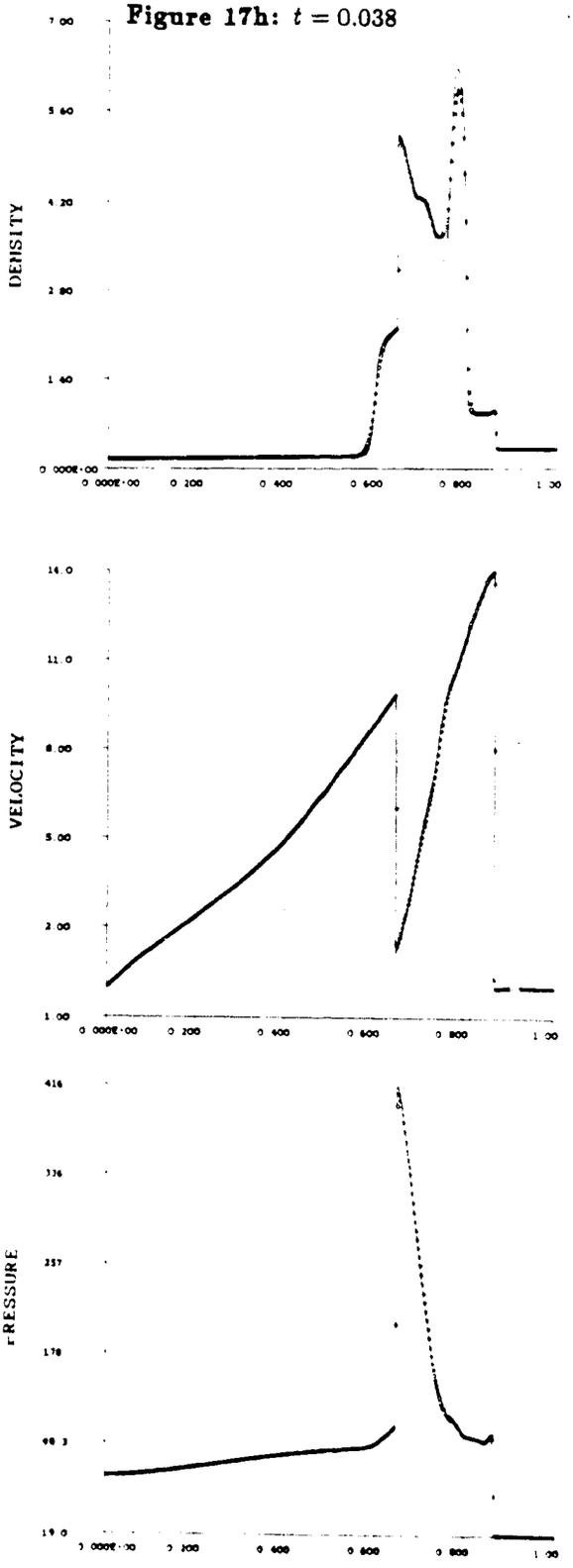

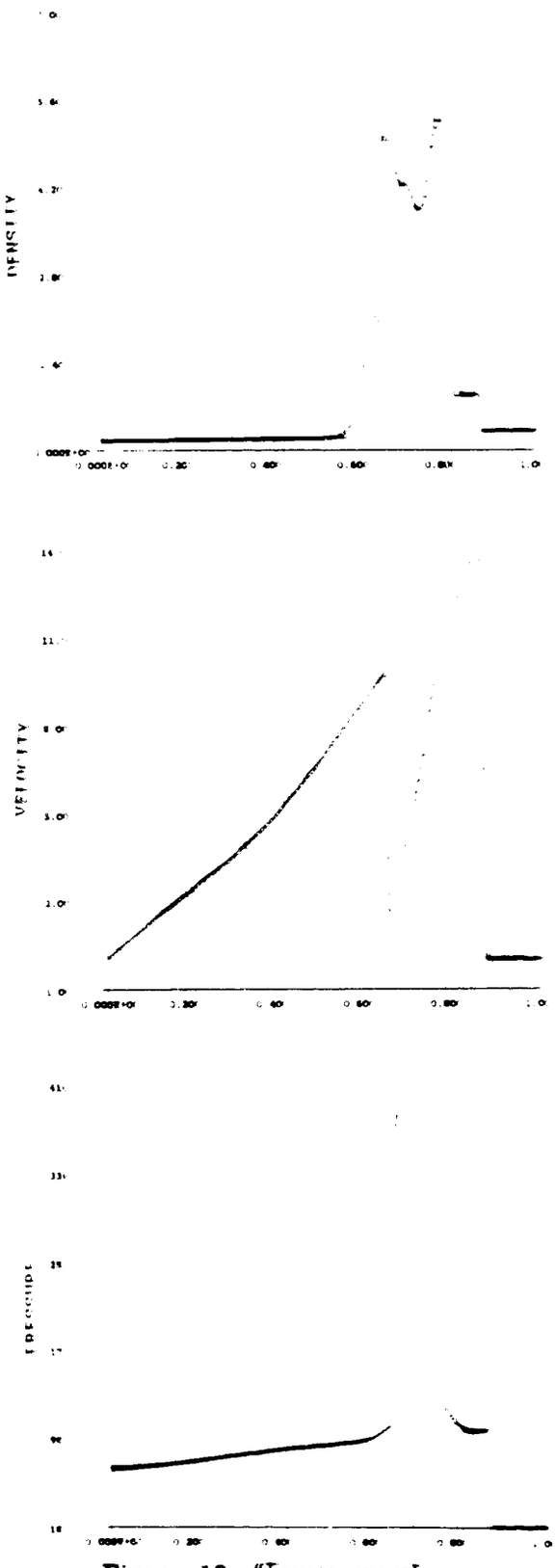

Figure 18: "Fourth-order" solution with $J = 200$ at $t = 0.038$

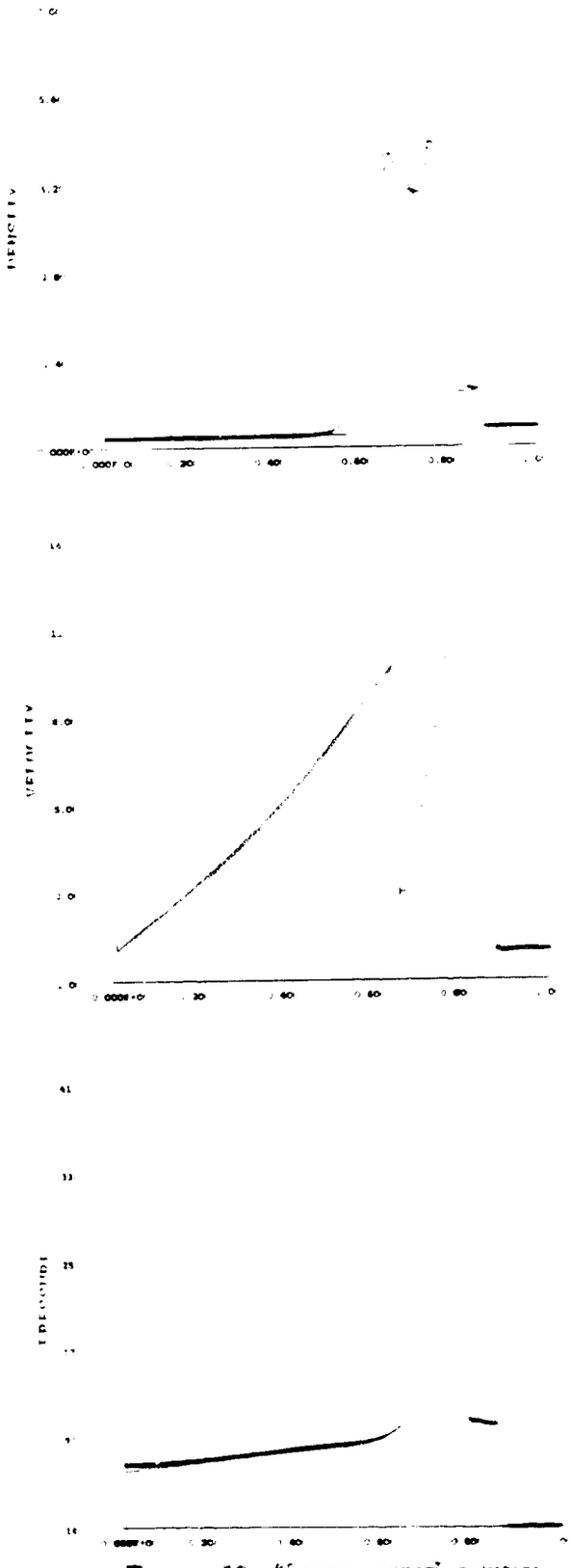

Figure 19: "Second-order" solution with $J = 200$ at $t = 0.038$

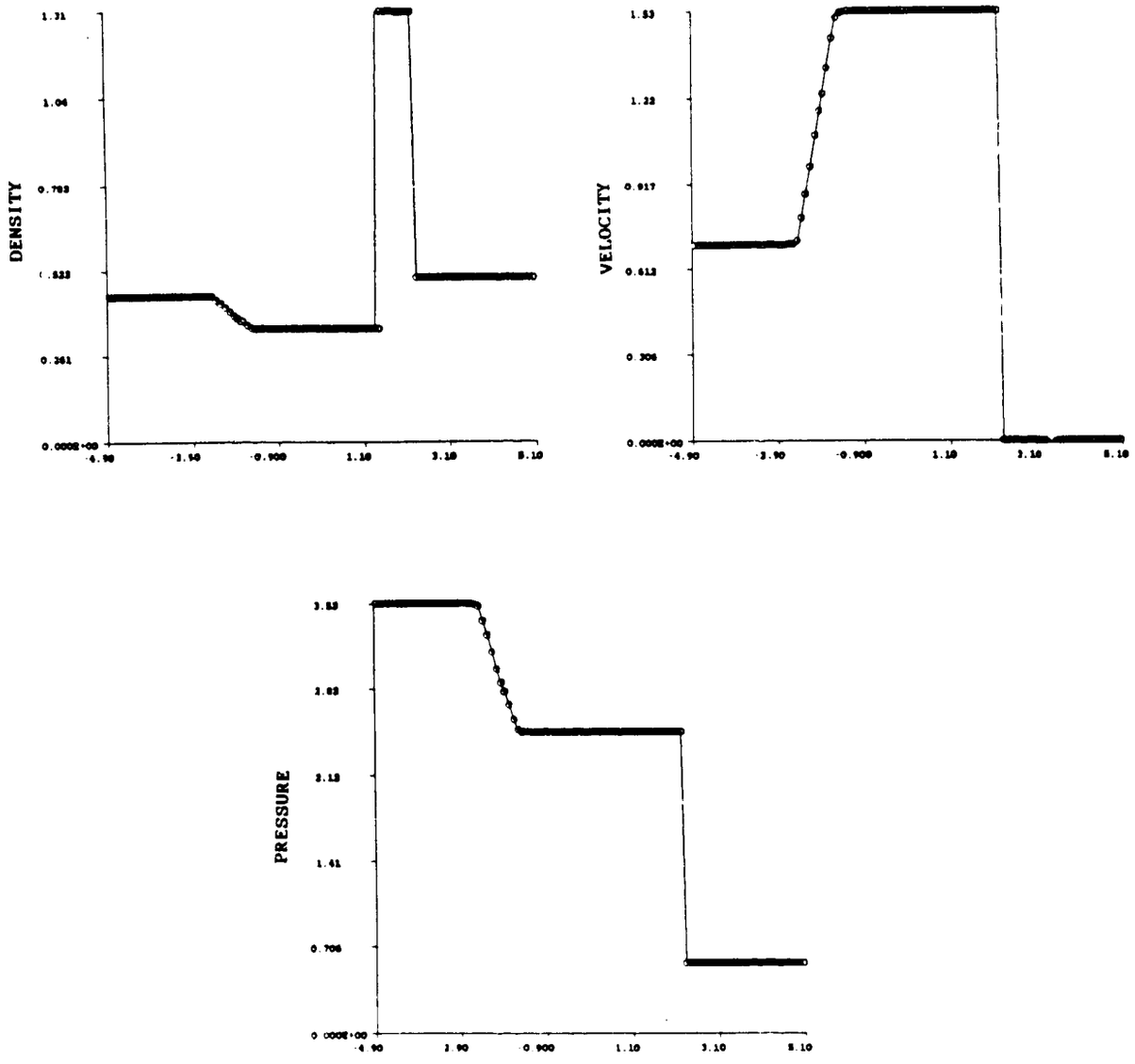

Figure 20: "Fourth-order" solution of Lax's problem with a self-adjusting grid

1. Report No. NASA CR-178101 ICASE Report No. 86-22	2. Government Accession No.	3. Recipient's Catalog No.
4. Title and Subtitle UNIFORMLY HIGH ORDER ACCURATE ESSENTIALLY NON-OSCILLATORY SCHEMES III.		5. Report Date April 1986 6. Performing Organization Code
7. Author(s) Ami Harten, Bjorn Engquist, Stanley Osher, Sukumar R. Chakravarthy		8. Performing Organization Report No. 86-22
9. Performing Organization Name and Address Institute for Computer Applications in Science and Engineering Mail Stop 132C, NASA Langley Research Center Hampton, VA 23665-5225		10. Work Unit No. 11. Contract or Grant No. NAS1-17070, NAS1-18107
12. Sponsoring Agency Name and Address National Aeronautics and Space Administration Washington, D.C. 20546		13. Type of Report and Period Covered Contractor Report 14. Sponsoring Agency Code 505-31-83-01

15. Supplementary Notes

Langley Technical Monitor:
J. C. South

Submitted to J. Comput. Phys.

Final Report

16. Abstract

In this paper, a third in a series we continue the construction and the analysis of essentially non-oscillatory shock capturing methods for the approximation of hyperbolic conservation laws. We present an hierarchy of uniformly high order accurate schemes which generalizes Godunov's scheme and its second order accurate MUSCL extension to arbitrary order of accuracy. The design involves an essentially non-oscillatory piecewise polynomial reconstruction of the solution from its cell averages, time evolution through an approximate solution of the resulting initial value problem, and averaging of this approximate solution over each cell. The reconstruction algorithm is derived from a new interpolation technique that when applied to piecewise smooth data gives high-order accuracy whenever the function is smooth but avoids a Gibbs phenomenon at discontinuities. Unlike standard finite difference methods this procedure uses an adaptive stencil of grid points and consequently the resulting schemes are highly nonlinear.

17. Key Words (Suggested by Authors(s))	18. Distribution Statement		
conservation laws, finite difference scheme, essentially non-oscillatory	02 - Aerodynamics 59 - Mathematical and Computer Sciences Unclassified - unlimited		
19. Security Class of this report) Unclassified	20. Security Classif.(of this page) Unclassified	21. No. of Pages 97	22. Price A05

For sale by the National Technical Information Service, Springfield, Virginia 22161

C-2

NASA-Langley, 1986

END

DATE

FILMED

AUG 12 1986